Study on coupling between MHD oscillation and turbulence in toroidal plasmas using beam emission spectroscopy

ONO MAKOTO

Doctor of Philosophy

Department of Fusion Science
School of Physical Sciences
SOKENDAI (The Graduate University for Advanced Studies)

Doctoral Dissertation

Study on coupling between MHD oscillation and turbulence in toroidal plasmas using beam emission spectroscopy

ビーム放射分光法を用いたトロイダルプラズマにおける MHD 振動と乱流の結合に関する研究

Makoto Ono

School of Physical Sciences,
The Graduate University for Advanced Studies

Supervisor: Professor Katsumi Ida, Mikiro Yoshinuma, Tatsuya Kobayashi

January 2017

Abstract

Non-linear coupling between MHD instability and low-k turbulence in toroidal plasmas is studied using by measuring the density fluctuations using Beam Emission Spectroscopy (BES). This work focuses on the Edge Harmonic Oscillation (EHO), which appears as a coherent mode at the frequency of about 10 kHz accompanied by several harmonics near the separatrix. This dissertation is composed of two parts, one of which includes the development and evaluation of the capability of BES system with specially designed sightlines in the Large Helical Device (LHD) as well as the spatio-temporal structure analysis of EHOs measured with the BES, and the other includes analysis on the non-linear coupling between EHO and turbulence measured in DIII-D tokamak.

A local density fluctuation diagnostic based upon the BES with lattice type optics configuration has been implemented on LHD to investigate the spatiotemporal and spectral characteristics of long wavenumber density fluctuations such as MHD activity. In most conventional BES systems, fiber images have round or rectangular shapes due to the configuration of fiber bundles, leading to the almost same wavenumber resolution in two directions on a focal plane. The unique optical fiber geometry which yields a lattice shaped sampling images in a plasma is applied in this system. The idea of the new lattice type fiber configuration is that utilizing the fiber bundle design that the images of fibers align along radial or polidal direction to achieve both enhancement of photon flux and good wavenumber resolution in a particular direction. With vertically elongated slits, the sensitivity for waves in the radial direction increases, although that for waves in the poloidal direction decreases. In order to complement this reduced poloidal wavenumber resolution, another sets of horizontally elongated slits is deployed, forming lattice structure. As a probe beam, a perpendicularly injected neutral heating beam is used, and its accelerating energy is typically 40 keV. The angle between the sight lines and the beam line is $\sim 120^\circ$ at the edge of the plasma, yielding a Doppler blue shift of ~ 3.0 nm in the H_α beam emission. Each channel consists of 7 (or 8) 400-μm-diam fibers arranged in line along poloidal or radial direction. Each fiber bundle of an array for radial wavenumber measurement images 10×140 mm and has a radial spatial separation of 10 mm. Each fiber bundle of an array for poloidal wavenumber measurement images 70×10 mm and has a poloidal spatial separation of 20 mm. These two arrays are overlaid in a same region to form a lattice configuration and views 70×140 mm in total. The array for radial wavenumber measurement averages the signals for 140 mm in poloidal direction, while that for poloidal wavenumber measurement averages for 70 mm in radial direction. The collected light is transmitted to a spectrometer and is detected simultaneously with the 4×8 pixel avalanche photodiode camera with a sampling frequency of 200 kHz. Correlation analysis was applied to reconstruct the two-dimensional spatiotemporal structure of MHD activities detected in the edge region in high-β discharge. The spatiotemporal structure of the low frequency density fluctuation of EHO was found to propagate in the direction of the electron diamagnetic drift velocity ($\boldsymbol{v}_e^* = -\boldsymbol{B} \times (\nabla \cdot \boldsymbol{P})/(n_e B^2)$) at the phase velocity of 1.2 km/s, and have a finite radial propagation with the phase velocity of 0.4 km/s.

The coupling between the high frequency turbulence and EHO is studied in Quiescent H-mode plasmas, where EHOs exist, in DIII-D tokamak. QH-mode is an ELM-free operation with good energy confinement, constant density, and radiated power, with a pedestal localized electromagnetic mode (EHO) providing continuous particle transport. The nonlinear interaction between harmonics of the EHO and turbulence is important to understanding the mechanisms and dynamics of enhanced particle transport in QH-mode. The fundamental frequency of the EHO was typically 10 kHz with long poloidal wavelength ($k_\theta \sim 0.02\text{cm}^2$) and broadband turbulence in the range of 50-200 kHz with correlation lengths of a few cm. The features and characteristics of QH-mode plasma turbulence in the wavenumber-frequency domain are crucial to understanding the mechanisms and dynamics of the enhanced particle transport. Frequency-wavenumber spectral analysis was applied to localized density fluctuation data measured with BES on DIII-D in the region of $0.8 < \rho < 1.0$. In the analysis, a Maximum Entropy Method is applied in the space domain, instead of a FFT, to estimate a well resolved k-spectrum from truncated data. The broadband turbulence measured at ρ 0.9 was found to have poloidal phase velocity of ~10 km/s, which corresponds to the ExB velocity. Bispectral analysis has been applied to the localized density fluctuation data. The cross-bicoherence among the BES channels showed radially varying magnitude of phase coherence well above the noise floor between the EHO and broadband turbulence in the region of $0.8 < \rho < 1.0$. The envelope analysis is done for the high frequency turbulence by applying Hilbert transform to the density fluctuation data. It was found that the turbulence amplitude was modulated at the frequency of EHO. The phase and amplitude of the turbulence envelope is not constant in time, and different from the displacement of the magnetic flux surface.

Acknowledgments

Special thanks are due to my thesis supervisors: Professor Katsumi Ida, Dr. Mikiro Yoshinuma, Dr. Tatsuya Kobayashi for their invaluable support, guidance and encouragement through my doctral course.

I am grateful to my dissertation committee: Professor Hiroshi Yamada, Dr. Motoshi Goto, Dr. Shinishiro Kado, and Dr. Yusuke Kosuga for their support, valuable feedback, and insightful ideas to this research.

I am deeply grateful to Dr. George R. McKee and Dr. Zheng Yan for their supports and kind helps through the internship work at General Atomics. I am also grateful to Dr. Keith H. Burrell, Dr. Xi Chen, Dr. Kshitish Barada, and Choongki Sung for their supports and many valuable suggestions and comments.

My sincere gratitude to previous and present Director General of National Institute for Fusion Science Prof. Akio Komori and Prof. Yasuhiko Takeiri, respectively. I wish to express my appreciation to all members of the LHD experimental group, NIFS and the Graduate University for Advanced Studies (SOKENDAI) staffs for their supports.

Finally, I am sincerely grateful to my family and friends for their support and understanding.

This work is partly supported by Ministry of Education, Sports, Culture, Science and Technology, MEXT KAKENHI Grant No. 23246164. This work is also partly supported by the National Institute for Fusion Science grant administrative budget NIFS10ULHH021.

Contents

List of Figures

List of Tables

Chapter 1

Introduction

Background and Motivation One of the most important subject among researches on the magnetic fusion plasma is improvement of confinement property and stability of the plasma to realize an economical and safe burning fusion reactor. Much effort has been dvoted to research of micro turbulence and MHD instability, and the understanding on plasma physics has been deepend over the decades. On the other hand, the turbulence appears electrostatic and different frequency or wave number range from MHD instabilities or behavior of magnetic flux surface, then studies on interections of those two phenomena are relatively scare. Recently, the existence of self-regulated oscillations in the radial energy transport into magnetic islands was found in a tokamak plasma [1]. This phenomenon indicates bifurcations in the island structure and transport, in other words the coupling between the transport and magnetic topology. In a helical device, a large-scale temperature fluctuations was discovered [2]. The fluctuation was low frequency of a few kHz, but it was found that the magnetic fluctuation level was too small to produce the observed temperature fluctuation, indicating different from MHD activities such as interchange modes. In this way, discoveries in a boundary region of turbulence and MHD activity is beginning to be accumulated experimentally and theoretically [3]. Callen has discussed magnetic turbulence effects on radial electron heat transport in tokamaks with considering drift-wave-induced magnetic perturbations [4]. This research will focus on the density fluctuation

poroperty caused by MHD and micro turbulence, and coupling of these two phenomena in torus plasmas.

As to the MHD oscillation, Edge Harmonic Oscillation (EHO) is observed in this research. EHO is an edge localized MHD oscillation at a typical fundamental frequency of $\sim$ 10 kHz with several higher harmonic componets, and mostly observed quiescent H-mode (QH) [5, 6] in some tokamak devices. QH-mode exibits stationary operation with an H-mode edge pedestal, good thermal confinement and particle transport for impurity removal [7], but without bursting behavior associated with edge localized mode (ELM). QH-mode was originally discovered on DIII-D [5], and was subsequently achieved on ASDEX-Upgrade [8, 9], JT-60U [10, 11], and Joint European Torus (JET) [9].

The peeling-ballooning mode [12, 13] theory of ELMs has been used as a working hypothesis to organize analysis of QH-mode [14]. In the theory, there are two key factors in the edge stability physics; these are the edge pressure gradient and the edge current density as is shown in Fig. 1.2. Experimental study with plasma current ramp up/down in DIII-D has ascertained that QH-mode opetates near the peeling boundary. As for the balooning boundary, the pedestal pressure is kept just below the boundary with enhanced transport. Measurements of divertor $D\alpha$ signal has shown that the light intensity is enhanced with the amplitude of EHO and is modulated at the frequency of EHO, implying that EHO enhances edge particle transport. However, the edge $D\alpha$ intensity does not just follow the amplitude of EHO, and the edge particle loss mechanism does not show a simple correlation with EHO.

Subject of this thesis is to investigate between MHD instability and turbulence in torus plasmas. This thesis is organized as follows:

In Chapter 2, the experimental setups of the study are explained. In order to conduct observation in torus plasmas with diffrent magnetic configuration, we use two devices, the Large Helical Device (LHD) and the DIII-D. Principles of Beam Emission Spectroscopy (BES) that are used for density fluctuation measurement are explained. Lattice-type optical configuration

is deployed to the BES that is used in this thesis in LHD, and the property of the system such as spatial resolution and wavenumber sensitivity is discussed.

Chapter 3 reviews analysis methods including Fourier transform, Maximum Entropy Method, Hilbert transform and Bispectrum.

In Chapter 4, the experimental results are given. A low frequency electromagnetic mode called Edge Harmonic Oscillation observed in LHD is explained. Then, the spatio-temporal structure of EHO is analyzed. The structures of EHO observed in LHD and DIII-D are discussed. The properties of high frequency turbulence observed in DIII-D in the presence of MHD instability is discussed. Then, the interaction between EHO and turbulence is investigated by using bicoherence analysis and envelope analysis.

Finally, a conclusion of the research is given.

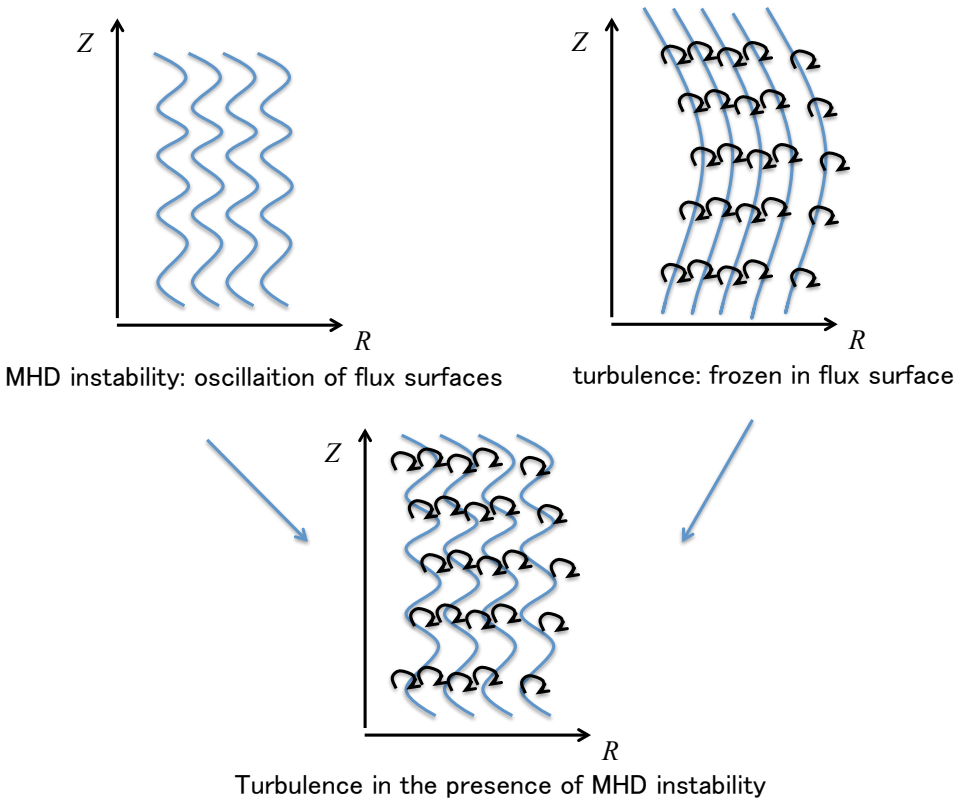

Figure 1.1: Schematic of the turbulence and flux surface.

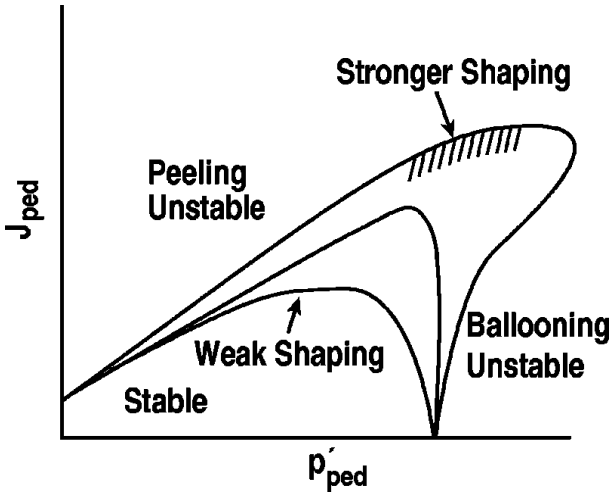

Figure 1.2: Schematic illustration of the peeling-ballooning mode stability boundaries [14]. Weak shaping corresponds to a circular cross section plasma. Stronger shaping is a modest triangularity (0.3), elongated, single null divertor. The stability boundary for a high triangularity double-null divertor would extend further up and to the right; this is not shown. The QH-mode operating region is indicated by the shaded region.

Chapter 2

Experimental Setup

2.1 Large helical Device

Large Helical Device (LHD) [15], which started experimental campaign in 1998, is a heliotron magnetic confinement fusion device. The LHD has a pair of superconducting helical coils with $l/m = 2/10$, together with three pairs of superconducting poloidal coils. The hilical coils generates the rotational transform and magnetic shear. The typical rotational transform has a central value of about 0.35 and an edge value of about 1.4 [16]. The poloidal coils provide a vertical field to control the position of the plasma column, the magnetic axis, the elongation and the leakage of the magnetic field. With those coils, LHD produces currentless plasmas.

Five priority subjects of the LHD are as ollows: (1) to produce plasmas with high temperature, high density, and long energy confinement time and to execute a wide range of studies on transport that can be extrapolated to reactor plasmas; (2) to achieve high-b plasmas with β of more than 5% and to study the related physics; (3) to obtain the basic data required for steady-state operation by long-pulse experiment of net-current- free plasmas with the installation of a divertor; (4) to study the behavior of highly energetic particles in the helical magnetic field and to execute a simulation experiment of a particles in reactor plasmas; and (5) to excute studies complementary to tokamak plasmas to deepen the comprehensive understanding of toroidal

plasmas.

In LHD, which is a heliotron device, the magnetic structure for plasma confinement is formed only by the magnetic coils. Therefore, plasma current is not nessesary to sustain a plasma. This feature provides an advantage for stady-state discharge, and for avoiding disruptions caused by plasma current induced instabilities. Based on the physics data base and operational experience accumulated over a decade, engineering reseaches aming for a heliotron fusion reactor have been conducted [17]. The main parameters of LHD are shown in Tab. 2.1 [16].

The pair of superconducting helical coils of 450 turns has its major and minor radius of 3.9 m and 0.975 m, respectively. The magnetic flux surface shapes almost an alipse on a poloidal cross section, and it rotates five times for one turn in toroidal direction as shown in Fig. 2.1. The helical coils are composed of three layers (HI, HM, HO), enabling to control the plasma minor radius and rotational transform by controling the current ratio among those three layers. LHD has a helical divertor configuration without using magnetic coils to form divertor configuration [18]. For heating a plasma, three methods of electron cyclotron heating (ECH), ion cyclotron heating (ICH) and neutral beam injection (NBI) are used [19, 20].

2.2 DIII-D Tokamak

The DIII-D tokamak was developed from the earlier Doublet III [21] device in1986. A ‘doublet’ is a two lobed toroidally symmetric plasma configuration with a crosssection containing a separatrix in the shape of a figure ‘8’ usually with the lobes shifted radially outwards [22]. Doublet III was considerably larger (BT = 2.6T at R = 1.43 m, a = 0.44 m) and designed with a copper coil configuration specialized for shaping doublet plasmas. The Doublet Ill experiment was more successful when operated with a conventional plasma geometry having an 'expanded boundary' divertor, that is with an internal magnetic separatrix but without a divertor chamber. It was, therefore, decided to rebuild the tokamak within the existing toroidal field coil set so as

to maximize the volume available for this configuration (Fig. 2.2), at the same time increasing the shaping capability. The DIII-D design was driven by the desire to achieve high plasma performance in a modest sized device while maintaining the flexibility in the configuration to allow the device to be modified in response to changing needs in the research programme (Fig.).

The DIII-D device has an aspect ratio similar to that of JET, $R/a = 1.67/0.67$, a maximum toroidal field of 2.2T, and has achieved plasma currents of up to 3 MA [23]. Deutrium neutral beam injection provieds up to 20 MW of heating power with ion energies of 75 keV, with higher power available at ion energies of up to 93 keV. One of the four neutral beam lines has been rotated toroidally to provide 5 MW of power in the opposite direction to the other beams to allow controlled experiments on the influence of plasma rotation on plasma performance. Both the ion cyclotron radiofrequency and the electron cyclotron resonance heating systems have installed source powers of 6 MW. The former is tunable in the range 60 to 120 MHz, while the latter operates at 110 GHz and allows power modulation at frequencies of up to 5 kHz.

2.3 Beam Emission Spectroscopy

Introduction Hydrogen atoms of a neutral beam emit lights as a result of interection with a bulk plasma. These lights emitted from the neutral beam particles are Lyman lines and Balmer lines and called ”beam emission”. Beam emission spectroscopy is a method to measure space and time variation of the beam emission, therefore is utilized for plasma density fluctuation measurement. Bright lines of beam emission are Doppler shifted due to a component of velocity of a neutral beam in a sightline direction. Accordingly, beam emission can be distinguished from the strong background emission at plasma edge by the Doppler shift. However, because velocity of beam particles are independent of ions of a bulk plasma bright lines obtained by BES don’t include information such as ion velocity distribution, which charge exchange recombination spectroscopy can measure.

Conceptual schematic of BES is shown in Fig. 2.4 [24]. As fluctuations arise along magnetic field lines, a sight line should be tangential to a flux surface as much as possible to measure the local fluctuations. In addition, a configuration such that a component of velocity of a neutral beam in a sightline direction is large is favorable to get a large Doppler shift. Among the bright lines of beam emission, Balmer H_α line (656.285 nm) is most intense in brigtness, and is the target line to detect. With imaging optics and an array detectors, imaging measurement of density fluctuations in radial and poloidal directions is available to produce two-dimensional spectrum $S(k, f)$ in wavenumber-frequency space. Measurable wavenumber limit is determined by spatial sampling intervals Δx, and the measurable wavenumber range is given as

$$0 \leq k \leq \frac{2\pi}{2\Delta x}. \tag{2.1}$$

BES can measure fluctuations of long wavelengths up to $k \approx 0$. And one of the features of this method is a local measurement, which measures only lights emitted from the sample volume where a sightline and a probe beam cross. BES has a high ability in determining a location of luminescence. However, when curvature of magnetic fild lines in a sample valume is large the measured value corresponds to density fluctuations ensembled over different flux surfaces.

The principle of BES was first proposed by Fonck, then it was established as a measurement method in experiments on the PBX-M tokamak of Princeton University in 1989 [25]. BES was also applied to TFTR [26] tokamak of Princeton University and Phaedrus-T [27]tokamak of Wisconsin University. With those BES systems, researches on properties of fluctuations of long wavelength such as radial distribution of density fluctuation level, and correlation between confinement time and fluctuation level was done. After that, BES was applied to TEXT-U [28] and DIII-D [29], and measurement results on density fluctuation phenomena during formation of internal transport barriar [30] and L-H transition [31] has been reported, indicating correlation between density fluctuation and confinement performance. Observation of zonal flow by BES

on DIII-D was reported in 2002 [32].

Large tokamaks have an advantage that curvature of field lines in sampling volumes is small, while small devices and Helical devices have difficulties to apply BES beacause of the large curvature of field lines or the toroidal variation of magnetic structure. However, BES was applied to the Compact Helical System by optimizing configurations so that sightlines are as tangential to flux surfaces as possible [33, 34, 35]. Using the BES system in CHS, density fluctuations and density gradient was observed simultaneously [36]. Based on results from CHS, BES has been developped in other Helical devices such as the Large Helical Device [37] and Heliotron J [38].

2.3.1 Principle of BES measurement

Doppler shift

As mentioned above, beam emission is Doppler shifted from back ground lights due to beam particle velocity. Therefore beam emission can be separated from the back ground lights by using spectroscopic method. Doppler shift $\Delta\lambda$ is expressed as

$$\frac{\Delta\lambda}{\lambda_0} = \frac{v\,\cos\theta}{c} \tag{2.2}$$

where v, θ, c and λ_0 are beam particle velocity, the angle formed by a beam and a sightline, the speed of light and a wavelength of beam emission, respectively. Observed wavelength is $\lambda_0 - \Delta\lambda$ when beam particle moves toward an observer, and $\lambda_0 + \Delta\lambda$ when beam particle moves away from an observer. Because separating beam emission from back ground lights will be easier when $\Delta\lambda$ is large, the angle θ formed by a beam and a sightline is desirable to be small.

Relation between density fluctuation level and beam emission intensity fluctuation based on collisional radiative model

Beam particles injected into a hydrogen plasma are excited by several collisional processes as below

- Electron collision excitation:

$$e^- + H^0 \rightleftharpoons e^- + H^{0*}(n) \quad (n \geq 2)$$

$$e^- + H^{0*}(n) \rightleftharpoons e^- + H^{0*}(m) \quad (m > n \geq 2)$$

- Bulk ion collition excitation:

$$H^+ + H^0(n) \rightleftharpoons H^+ + H^{0*}(n) \quad (n \geq 2)$$

$$H^+ + H^{0*}(n) \rightleftharpoons H^+ + H^{0*}(m) \quad (m > n \geq 2)$$

- Electron collision ionization:

$$e^- + H^{0(*)} \rightarrow e^- + H^+ + e^- \quad (n \geq 1)$$

- Bulk ion collision ionization:

$$H^+ + H^{0(*)}(n) \rightarrow H^+ + H^+ + e^- \quad (n \geq 1)$$

- Bulk ion collision charge exchange:

$$H^+ + H^{0(*)}(n) \rightarrow H^{0(*)}(n) + H^+ \quad (n \geq 1)$$

where H^0 and $H^{0*}(n)$ denote a hydrogen beam atom in the ground state and an excited beam atom with the principal quantum number n, respectively. Here, contribution from impurity collition is assumed to be small compared to electron and ion collision.

The spontaneous emission intensity I_{jk} is

$$I_{jk} = A_{jk} N_j h\nu \Delta V \Delta\Omega / 4\pi \tag{2.3}$$

Here, A_{jk} is the rate coefficient of spontaneous emission (Einstein A coefficient) from $n = j$ to $n = k$ state, N_j is the population density of $n = j$ state, h is the Planck constant, ν is the frequency of the emission, ΔV is sample volume in which a probe beam and a sightline across, and $\Delta\Omega$ is solid angle viewing the sample volume from an objective lens. As target bright line is H_α line ($n = 3 \rightarrow 2$) in this research,we will consider the rate equation for the state of $n = 3$.

If a coronal model, where the distribution of $n = j$ state is determined by collisional ecxitation from the ground state and spontaneous emission to lower levels, can be applied, the intensity would then be approximately proportionalto the plasma density. However, except the lowest density plasmas the coronal approximation does not apply. Instead, in addtion to the excitation from the ground state and spontaneous decay as in the coronal model, collisional transitions, both upward and downward, to and from other electron states should be considered for the pupulation of the excited state. Therefore, a full colisional-radiative model of the state populations must be used [39].

The rate equations governing the population N_j of principal quantum number $n = j$ are expressed in matrix form as

$$\frac{\mathrm{d}N_j}{\mathrm{d}t} = \sum_k N_k M_{kj}, \tag{2.4}$$

where M_{kj} is a matrix of rates governing the transitions from levels k to j. The diagonal of M is equal to minus the total rate for transitions out of the level j to all other states, including electron loss from the state j due to ionization and charge exchange. Here, electron and ion collision contributions to the collisional ecxitation (and deextation) rate coefficients will be treated together, and electron density and ion density are treated as equivalent ($n_\mathrm{e} = n_\mathrm{i}$). In the low-energy range (1-30 keV), electron-impact collisions dominate the excitation and ionization rates, and charge exchange dominates electron-loss mechanism. For beam energies above ~ 40 keV, proton-impact collitios become dominant for excitation and ionization, and the proton-impact ionization exceeds the charge-exchange rate [43].

The matrix M_{kj} can be separated for radiative and collisional process as $M_{kj} = n_\mathrm{e} X_{kj} + R_{kj}$, where the off-diagonal terms of R are equivalent to the Einstein coefficients A_{kj}, and minus values of losses from the level j to all other states are summed on the diagonal ($A_j = \sum_k -A_{kj}$),

$$R_{jk} = \begin{pmatrix} 0 & 0 & 0 & \dots & 0 \\ A_{21} & A_2 & 0 & & \vdots \\ A_{31} & A_{32} & A_3 & & \vdots \\ \vdots & \vdots & & \ddots & \vdots \\ A_{k1} & A_{k2} & \dots & A_{k(j-1)} & A_j \end{pmatrix}. \tag{2.5}$$

For the conditions of interest ($E_\mathrm{beam} \geq 40$ keV, $T_\mathrm{e} = T_\mathrm{i} \sim 1$ keV), the tridiagonal coefficients in X are dominant, therefore transitions such that $|j-k| \leq 1$ govern the behaviour. Furthermore, rates for upward transitions ($j \rightarrow j{+}1$) are larger than rates for downward transitions ($j \leftarrow j{+}1$). This situation can be regarded as an upward cascade of electrons one towards higher states. Then, the rate equations can be written in simple lower-triangular form as

$$\frac{\mathrm{d}N_1}{\mathrm{d}t} = -D_1 N_1, \tag{2.6}$$

$$\frac{\mathrm{d}N_2}{\mathrm{d}t} = P_{12} N_1 - D_2 N_2, \tag{2.7}$$

$$\frac{\mathrm{d}N_3}{\mathrm{d}t} = P_{13}N_1 + P_{23}N_2 - D_3N_3, \tag{2.8}$$

where P_{kj} is the rate at which the excited state j is populated from state k with a correction for downward cascade, and D_j is its total depopulation rate. The following expressions indicate the best set of explicit transition effects, which give good agreement with a full-scale calculation using the entire transition matrix M [39].

$$D_3 = (X_{34} + X_{35} + X_{32} + L_3)n_\mathrm{e} + A_3, \tag{2.9}$$

$$D_2 = (X_{23} + X_{24} + X_{21} + L_2)n_\mathrm{e} + A_2, \tag{2.10}$$

$$D_1 = \left(X_{12}\left[1 - \frac{X_{12}n_\mathrm{e} + R_{21}}{D_2}\right] + X_{13} + L_1\right)n_\mathrm{e}, \tag{2.11}$$

$$P_{12} = \left(X_{12} + X_{13}\frac{X_{32}n_\mathrm{e} + R_{32}}{D_3}\right)n_\mathrm{e}, \tag{2.12}$$

$$P_{13} = \left(X_{13} + X_{14}\frac{X_{43}n_\mathrm{e} + R_{32}}{D_4}\right)n_\mathrm{e}, \tag{2.13}$$

$$D_4 = (X_{45} + X_{43})n_\mathrm{e} + A_4, \tag{2.14}$$

$$P_{23} = X_{23}n_\mathrm{e}. \tag{2.15}$$

Here, L_j is the rate for direct electron loss due to ionization and charge exchange from level j, A_j is the total radiative transition rate to all levels below j. Dominant flows in of electrons in the energy level diagram are shown in Fig. 2.5. Figure 2.6 shows the results of calculations for $j = 3$ and $j = 2$ states of hydrogen which gives rise to the H_α and L_α lines [39]. The overall shapes of the curves of the excited-state fractions $f_i = N_j/N_1$ are remarkably similar for all temperatures and energies. This fact results in the logarithmic derivatives of f_j lying almost on a universal curve as shown in the middle panel of Fig. 2.6. The relative amplitude of the intensity fluctuations $\delta I/I$ can be evaluated in terms of the differential cross section for the fractional population of the ecxited state j, $\kappa_j = (n_\mathrm{e}/f_j)(\mathrm{d}f_j/\mathrm{d}n_\mathrm{e})$, thus the logarithmic derivative $\mathrm{d}\ln f_j/\mathrm{d}\ln n_\mathrm{e}$. The difference of beam energies lead to noticeabe shifts in the absolute values

of f_j but changes in d ln f_j/d ln n_e negligible. The temperature variation produces a slight shift in the horizontal direction of the logarithmic derivative curves and the time-constant (τ_2, τ_3) curves as a result of the modest increase of the collisional rate coefficients at lower T_e. By reading values from the plots, we have $\kappa \approx 0.6$ for $j = 3$ at moderate densities of a few $10^{19}\mathrm{m}^{-3}$. In the following sections, we will be discussing property of density fluctuation qualitatively, regarding fluctuations in observed beam emission $\tilde{I}/I$ as density fluctuation $\tilde{n}/n$. In the case that the absolute value of density fluctuation is needed, the constant proportionality C in the relation ($\tilde{n}/n = C\tilde{I}/I$) will be calculated using the plasma parameters for a discharge of interest.

2.3.2 BES System With Lattice-shaped Viewing Geometry

A local density fluctuation diagnostic based upon the BES with radially and poloidally elongated sightlines has been implemented on the LHD to investigate the spatiotemporal and spectral characteristics of long wavenumber density fluctuations) such as magnetohydrodynamics (MHD) instability. The first application of BES to a helical system resulted in the compact helical system (CHS) [34, 35]. In that system, the simultaneous measurement of the density fluctuations and density gradient was accomplished with the optimized sightlines, which are aligned nearly tangent to the magnetic axis.

The ealier application of BES systems in LHD utilized sightlines nearly parallel to the midplane and passing through the plasma in the toroidal direction with tangentially injected neutral beams. In order to cover the large Doppler shift of the $H\alpha$ beam emission because of the high-energy neutral beam atom (beam energy $E \sim 120 - 170$ keV) and the large morional Stark splitting due to the large $v \times \boldsymbol{B}$ (magnetic field B of 3.0 T), a grating spectrometer was chosen for isolation of the beam emission instead of the interference optical filter [40]. When a neutral beam propagates across the magnetic field ($\boldsymbol{V}_{\mathrm{beam}} \nparallel \boldsymbol{B}$) in a plasma, the hydrogen atoms feel the electric field in the atom's rest frame due to the motion across the magnetic field ($\boldsymbol{E}_m = \boldsymbol{V}_{\mathrm{beam}} \times \boldsymbol{B}$). The induced electric field $\boldsymbol{E}_m$ in the hydrogen atoms causes the Stark shift,

$a_{\mathrm{i}} V_{\mathrm{beam}} B \lambda_0^2 \sin\phi$, where i $= 1 - 15$ is the number of Stark split, ai is a coefficient of the wavelength shift for the Stark split, λ_0 is the wavelength of Balmer α line for $E = 0$, and ϕ is the angle between the magnetic field and the neutral beam.When the Balmer α line is observed with an angle β to the neutral beam of a sightline, the Doppler shifted wavelength is $(V_{\mathrm{beam}}/c)\lambda_0 \cos\beta$. Therefore, the observed wavelength of the Balmer α line is given as

$$\lambda_{\mathrm{i}} = \lambda_0 \left(1 + \frac{V_{\mathrm{beam}}}{c} \lambda_0 \cos\beta\right)\left(1 + a_{\mathrm{i}} V_{\mathrm{beam}} B \lambda_0^2 \sin\phi\right).$$

The neutral beam based on the negative ion source with high energy ($\sim 120 - 170$ keV) is injected tangentially to the torus for plasma heating. The beam energy is much higher than the energy of the positive ion source neutral beam used in CHS ($\sim 20 - 30$ keV). The induced electric field is roughly estimated to be 60 kV/cm in LHD for $(B, E_{\mathrm{beam}}, \theta) = (3.0\ \mathrm{T}, 170\ \mathrm{keV}, 20^\circ)$, while 10 kV/cm in CHS for $(B, E_{\mathrm{beam}}, \theta) = (1.0\ \mathrm{T}, 30\ \mathrm{keV}, -26.5^\circ)$, where E_{beam} is the beam energy, θ is the angle between the magnetic field $\boldsymbol{B}$, and the beam velocity $\boldsymbol{v}_{\mathrm{beam}}$. The interference filter used in the CHS BES system has the typical pass-band and the tunable wavelength of 1.0 nm and 0.6 nm, respectively. The interference filter used in CHS BES system covers the Doppler-shifted full energy component of the beam emission and the central wavelength shift corresponding to the probe beam energy range ($\sim 20 - 30$ keV) [35]. For the H_α line from the high-energy beam in LHD, the Doppler shift varies by about 2 nm, depending on the beam energy, and the Stark splitting is as much as 1.5 nm. This requires the capability of isolation with a bandwidth of 1.5 nm or wider along with a variable range of at least several nanometers. However, the capability was not achievable by use of the filter system. Therefore, a grating spectrometer was applied to control the transition wavelength over a wider range.

Another BES system was developped with sightlines viewing the plasma in the poloidal direction [37].

That system has detected edge MHD oscillations and achieved the radial profile of the coherence between the density fluctuation and the magnetic fluctuation. It was found that e-noise

in the root mean square value corresponds to around 5% of the dc value of the signal in the detected fluctuation spectrum, and the signal-to-noise ratio had to be improved to measure turbulences. Because of the larger size of LHD, which has a major radius R_{ax} of 3.5-4.0 m and an averaged minor radius a of 0.6 m, the distance from diagnostic ports to the plasma is larger and the solid angle for collecting beam emissions is smaller. Therefore, it is required to increase the sampling area to achieve sufficient detected photon flux and signal-to-noise ratio for fluctuation spectral analysis.

The BES system presented in this paper observes the density fluctuations on the poloidal cross-section. One of the most characteristic aspects is that the sight lines of this system can be optimized to investigate propagation behaviors for radial and poloidal direction by making slit shaped measurement channels perpendicular to each direction. In most conventional BES systems, a sampling area is round due to the shape of a fiber or rectangular with bundled fiber image [41, 44], leading to almost the same wavenumber sensitivity in two directions on a focal plane. The optical fiber geometry which yields slit-shaped sampling images in the plasma is applied to the BES system in LHD. The idea of the fiber configuration is utilizing the fiber bundle design — the images of fibers elongated along radial or poloidal direction to achieve both enhancement of photon flux and good wavenumber resolution in the directions along the narrow sides of the slits. Poloidally elongated sightlines are aligned in the radial direction to investigate the radial profile and propagation characteristic of density fluctuations, and radially elongated sightlines are aligned in the poloidal direction to investigate the poloidal structure of the fluctuations. These slit-shaped sightlines have the advantage that the wavenumber sensitivity is increased in the direction perpendicular to the slit direction. By combining the two sets of the radially and poloidally elongated sightlines in the same sampling area, both radial and poloidal wavenumber sensitivities are improved compared with the conventional square-shaped sightline. This configuration is expected to enable simultaneous measurement of radial and poloidal characteristics of the density fluctuation. This article presents the sightline design and

the estimated wavenumber sensitivity.

Figure 2.8 shows the top view of LHD drawn with the BES sight lines, the probe beam (NBI No. 5), and the typical magnetic surface on the mid plane [45]. The sight lines pass throughout the plasma in the toroidal direction, aligned for the radial and vertical directions. A neutral hydrogen atomic beam for heating is used as the probe beam, and its accelerating energy is 40 keV. The angles between the sight lines and the beam line range from 113° to 120° on the mid plane, yielding a Doppler blue shift of 2.3~3.0 nm in the H_α beam emission as shown in Fig. 2.10.

Figure 2.9 shows the fiber image configuration on the poloidal cross section. Each fiber has a numerical aperture of 0.25, a core diameter of 400 μm, and a clad diameter of 420 μm. The fiber images are almost focused at the center of the neutral beam and the roughly 25-to-1 magnification results in an observed spot size of about 1 cm in diameter on a poloidal cross section. The spots are located immediately adjacent to each other in each direction, therefore the spacial pitch $\Delta x \sim 1.0$ cm for radial/vertical direction. The arrangement of the fibers connected to the detection system can be selected, and the beam emission is detected with chosen 32 channels simultaneously. Each channel consists of 7 (or 8) fibers arranged in line along the poloidal or radial direction. Each fiber bundle of an array for radial wavenumber measurement images 10×130 mm and has a radial spatial separation of 20 mm. Each fiber bundle of an array for poloidal wavenumber measurement images 80×10 mm and has a poloidal spatial separation of 20 mm. These two types of arrays are overlaid in the same region to form a lattice-shaped viewing geometry and views 160×150 mm in total. The array for radial wavenumber measurement averages the signals for 130 mm in the poloidal direction, while that for poloidal wavenumber measurement averages for 80 mm in the radial direction.

The lights collected from the plasma are transmitted through the fibers to two grating spectrometers (Fig. 2.11 [42]). The spectrometer is composed of two lens sets with the focal distance of 200 mm (F/2.8) and a diffraction grating with the ruling number of 2160/mm.

To observe the center wavelength and luminescent intensity of beam emission, diffracted image is taken by a CCD camera. Spectrum images are usually taken for each shot for 100 frames with the exposure time of 94.2 ms and the sampling frequency of 100 ms. An example of spectrum image is shown Fig. 2.12. The horizontal axis and vertical axis correspond to wavelength and measurement location, respectively (shown in pixel number). Figures 2.12 (a) and (b) are the spectrum images of the emission from a plasma without the probe beam and with the probe beam, respectively. In the both cases, the H_α emission from the edge of the plasma can be seen as the brightest line around 620 [pixel] in the vertical axis. The beam emission is blue shifted as indicated by red arrows in Fig. 2.12 (b).

The beam emission separated from the background emission is detected by using Avalanche Photodiode Detector camera (APDCAM). The APDCAM uses a 4×8 element avalanche photodiode array (Hamamatsu S8550). The APD array is composed of 32 sensors of $1.6 \times 1.6\text{mm}^2$ area at a pitch of 2.3 mm as shown in Fig. 2.13. The typical gain factor is about 50 with 320V reverse voltage and the peak quantum efficiency is about 85% at 650 nm. The sampling frequency was set as 200 kHz for the experiments described later in Sec. 4.1.1.

Evaluation of detected photons Here, we will evaluate the number of insident photos to an APD. Figure 2.15 shows temporal evolution of a detected beam emission. The number of photons per digit will be estimated with an assumption that the amplitude of the signal in the time range when the probe beam is off corresponds to the intrinsic noise level of the detetor. With the estimated value, the number of insident photos to an APD will be calculated for the duration which the probe beam is injected. Subtracting the DC component, the average value of noise level is around 84~ [digit] for $7 < t < 8$s. For its sampling frequency is 200 kHz, the noise amplitude per unit time is $84 \times 2 \times 10^5 \approx 1.6 \times 10^7$ [digit/s]. The noise equivalent photon flux for the detector is 5×10^7[photon/s]. From the above, the number of photons per unit digit can be estimated to be $5 \times 10^7 / 1.6 \times 10^7 \approx 3.1$[photon/digit]. For $4 < t < 5$s, the average of beam emission intensity (subtracted baias level) is 4.2×10^3[digit], or 8.4×10^8[digit/s]. Then, the

number of insident photons of beam emission is estimated to be $8.4 \times 3.1 \approx 2.6 \times 10^9$[photon/s].

Spatial Resolution Determined by Line Integral Effect The images of the light collecting fiber set for viewing perpendicularly injected neutral beam have a spatial width of 1 cm and a spatial pitch of 1 cm on the focal plane. Because of the probe beam width, the sampling volumes of each line of sight pass through several magnetic flux surfaces, and this leads to integration of beam emission across different flux surfaces. Thus, it is essential to estimate this integral effect to evaluate the localization of the measurement.

On the assumption that the beam emission intensity is proportional to the product of the bulk plasma density and neutral beam density, $n_e n_{beam}$, we will evaluate the radial spatial resolution by effective minor radius, r_{eff} weighted by $n_e n_{beam}$. Here, r_{eff} denotes the radius of the equivalent simple torus which encloses the same volume as the flux surface of interest. The evaluation is done with the beam profile data of NBI#4, which is the same type as NBI#5, which is perpendicularly injected on the mid plane with the beam energy of $E \simeq 40$keV. Figures 2.16, 2.17, 2.18 and 2.19 show the profiles on the mid plane of effective minor radius r_{eff}, electron density n_{e}, beam particle density n_{beam} and the multiple of electron density and beam particle density $n_{\mathrm{e}} n_{\mathrm{beam}}$, respectively. For each profiles, the origin of the coordinate axes is the center of torus. Figure 2.20 is a plot of the value of $n_e n_{beam}$ along sightlines on the mid plane with respect to the effective minor radius.

If we define the spatial resolution as the standard deviation in effective minor radius weighted by the multiple value of electron density n_{e} and beam particle density n_{beam} along each sightline, this is expressed as

$$\Delta r_{\mathrm{eff}} = \sqrt{\int w \cdot (r_{\mathrm{eff}} - r_{\mathrm{eff}\ 0})^2 dl}, \tag{2.16}$$

where, w is defined as

$$w = \frac{n_{\mathrm{e}} \cdot n_{\mathrm{beam}}}{\int n_{\mathrm{e}} \cdot n_{\mathrm{beam}} dl}, \tag{2.17}$$

and measurement central position in radial direction $r_{\mathrm{eff}\ 0}$ is defined as

$$r_{\mathrm{eff}\ 0} = \int w \cdot r_{\mathrm{eff}} dl. \tag{2.18}$$

The evaluated location for lines of sight on the mid plane in the range of 4.30 < R < 4.65 m is 0.66 < reff 0 < 0.53 m (Fig. 2.21). The spatial resolution is $2\Delta r_{\mathrm{eff}} \sim 0.01$ m at the edge and this increases up to ∼ 0.10 m. The ratio of the light intensity emitted from the region of $r_{\mathrm{eff}\ 0} \pm \Delta r_{\mathrm{eff}}$ to the total light intensity integrated along a line of sight is expressed as

$$w_0 = \sqrt{\int_{r_{\mathrm{eff}\ 0}-\Delta r_{\mathrm{eff}}}^{r_{\mathrm{eff}\ 0}+\Delta r_{\mathrm{eff}}} w dr_{\mathrm{eff}}}, \tag{2.19}$$

For the region of 4.30 < R < 4.65 m, w_0 was estimated ∼68%. The deviation in r_{eff} of the poloidally elongated slit sightlines in the range of 4.30 < R < 4.65 m is around 0.01 m for the typical discharges in LHD. This deviation is smaller than the line integral effect.

The finite lifetime effect of the excited beam atoms is not taken into account in the calculation because the displacement of the beam particle for the life time is comparable or smaller than the line integral effect. The displacement d due to the life time effect can be calculated as

$$d = v_{\mathrm{beam}}/A_{3\to2} = \sqrt{(2E_{\mathrm{beam}}/m_{\mathrm{H}})}/A_{3\to2}, \tag{2.20}$$

where v_{beam}, $A_{3\to2}$, E_{beam} and m_{H} are beam particle velocity, Einstein coefficient for spontaneous emission of H_α line, beam energy and hydrogen mass, respectively. With the values of $A_{3\to2} = 4.39 \times 10^7$/sec, $m_{\mathrm{H}} = 1.67 \times 10^{-27}$ kg and beam energy $E_{\mathrm{beam}}$of 40 keV in the radial direction, the displacement d of the beam particle during the life time is ˜ 6.3 cm. This displacement corresponds to Δr_{eff} ˜ 0.02 m at R = 4.6 m and Δr_{eff} ˜ 0.03 m at R = 4.3 m.

The beam attenuation effect, that is the beam density, depends on the mode strength and structure of density fluctuation. When the beam attenuation effect is strong, the evolution of

the beam density is needed to be calculated step-by-step with the change in the spatial structure of the density. However, the beam attenuation effect is relatively small and can be neglected in LHD plasma. At $R = 4.6\,\mathrm{m}$, where the wavenumber sensitivity was the calculated, the attenuation of the neutral beam used was only 10% of the initial beam density, because the electron density in LHD is relatively low of $1 \times 10^{-19}\,\mathrm{m}^{-3}$ near the plasma edge. Therefore the intensity modulation at $R = 4.6\,\mathrm{m}$ due to the change in beam attenuation is reduced to 1/10 of the density fluctuation amplitude at $R > 4.6\,\mathrm{m}$.

Wavenumber Sensitivity Figure 2.23 (a) shows the shapes of the fiber bundles of square (A), radially elongated slit (B), and poloidally elongated slit (C) [46]. The radial location for each bundle was taken at $R = 4.60\,\mathrm{m}$ ($r_{\mathrm{eff}} \sim 0.65$ m at the intersection of the line of sight and the probe beam center on the mid-plane). For comparisons of wave number sensitivity among the different types of bundle designs, intensity of collected light by using each bundle design was calculated. In the calculation, test data which has white spectrum in poloidal or radial wavenumber is sampled at points in the Δr_{eff} and multiplied with light intensity ($n_{\mathrm{e}} n_{\mathrm{beam}}$), and sampled signal ensembled over a fiber bulndel is normalized with a signal sampled at an ideal imaging point in (r_{eff}, z) space (the idal point doesnt have width in the 2D space). The sensitivity is taken as a root mean square value of collected wave intensity at each fiber image of the bundle design and normalized with the wave intensity collected with a dot shaped sampling image at the center of the bundle. This calculation is done with consideration of the line integral effect in the radial direction (Δr_{eff}), and wave amplitude is weighted with the multiple values of ne and nbeam. The test wave data is a 20 kHz plane wave in (r_{eff}, Z) plane with white spectrum of kz (or $k_{r\mathrm{eff}}$) and $k_{r\mathrm{eff}} = 0$ (or $k_Z = 0$). Figure2.23 (b) shows the poloidal wave number sensitivity for each bundle design. While the poloidal wave number sensitivity of square and poloidally elongated slit drop sharply, the radially elongated slit keeps sensitivity up to $k_Z/2\pi = 50\,\mathrm{m}^{-1}$, which corresponds to the inverse of the double value of the fiber image diameter. For the wavelengths of which the integer multiple correspond to the length in the poloidal direction of

the sampling areas, the collected signals are averaged to be zero, and this can be the sensitivity drop. Figure 2.23 (c) shows the radial wave number sensitivity for each bundle design. Although the sensitivities are almost comparable between the radially elongated sightline and the square shaped sightline because the widths of the sampling areas in the radial direction are almost similar ($\Delta r_{\rm eff}$ is 1.9 and 2.7, respectively), the poloidally elongated slit has better sensitivity in the range of $0 < k_{r\rm eff}/2\pi < 60$.

Spatiotemporal structure of fluctuations is determined by a two-point two-time correlation function at a different position. Two-point two-time correlation function can be given by

$$R(x,\tau) = \frac{\langle I(x,t) I_{\rm ref}(t+\tau)\rangle}{\sqrt{\langle I^2(x,t)\rangle}\sqrt{\left\langle I^2_{\rm ref}(t)\right\rangle}}, \tag{2.21}$$

where τ is the time lag, $I(x,t)$ is the time series of the channel located at x, $I_{\rm ref}(t)$ is the time series of the reference channel, and $\langle\,\rangle$ stands for temporal average. Figures 2.24(a) and 2.24(c) show a contour plot of correlation functions of the test wave data ($f = 20\,\mathrm{kHz}$, $k_{r\rm eff}/2\pi = 20.0\mathrm{m}^{-1}$, $k_Z/2\pi = 18.2\mathrm{m}^{-1}$) detected with slit-shaped sightlines (group I and II in Fig. 2.9) for the poloidal direction and radial direction, respectively. From the slope of the peak in those contour plots, radial and poloidal phase velocities can be estimated $(v_r, v_\theta) \sim (1.0, 1.1)$ [km/s], corresponding to the value calculated with wavelength and frequency. Figures 2.24(b) and 2.24(d) show the contour plots of cross correlation of the wave sampled with square shaped sightlines. With the reduced number of channels of the square type array compared to the array of radially elongated sightlines and the spatial pitch comparable to the half of the wavelength in this case, the contour of correlation function cannot reconstruct the propagation direction (Fig. 2.24(b)).

2.3.3 BES System With High Spatial Resolution

For the current BES system in DIII-D, 64 channels are deployed in a 8 (radial) × 8 (poloidal) 2D grid, plus two common-mode rejection channels [49]. Each channnel images an approximately 0.9 cm (radial) × 1.2 cm (poloidal) region with channels located immediately adjecent to each other in each direction, for a total sampling area of approximately 7 × 12 cm. The array is placed on a motorized mount and can be remotely scanned radially to observe different spatial regions of the plasma on a shot-to-shot basis.

The system observes the emission resulted from an injected deuterium neutral beam with an energy of 70-80 keV ($v_{\text{beam}} = 2.6\times10^6$ m/s), and $P_{\text{NBI}} \approx 2.5$ MW. The beam atoms excited dut to collisions with electrons and ions emits D_α line from the three beam-energy components. Emission is Dopplershifted over approximately $\lambda \approx 652 - 655$ nm. Flctuations in the light emission intensity are proportional to the local density fluctuations, $\tilde{n}/n = C(\tilde{I}/I)$, with a proportinality factor, C of 2-3 for typical DIII-D plasma parameters [50, 51] The factor C depends on local plasma density, temperature, beam energy and Z_{eff}. Among these, The important parameter is density and the others have a fairly weak dependence.

The neutral beam viewing optical system consists of: a highthrouput $f/2$, $f = 40$ cm, objective lens, 25 cm vacuum window, in-vessel shutter, optical axis-folding mirrors (to avoid a toroidal field coil) and scannable 2D motorized fiber-mounting array, as shown in Fig. 2.27 [52]. The fibermounting array places the fiber faces at the curved focal plane of the objective lens. The objective lens images light from the beam onto a set of fiber optic bundles with a magnification M of 2.9-3.4, depending on the radial location of the image in the plasma. The sightline is deployed so that the sampling volume, which has a half-width of over 20 cm in the toroidal direction, is nearly tangent to a magnetic flux surface. The sightlines are also angled at approximately 5° in a vertical plane relative to the equatorial (horizontal) plane of the tokamak to more closely align the observation volume with the magnetic field pitch angle. The typical magnetic field pitch angles on DIII-D are in the range of $5° - 10°$ for plasma current opposite to

toroidal field direction. The individual fiber bundles for each spatial channel can be deployed arbitrarily in the focal plane. The 2D grid can be radially scanned on a shot-to-shot basis across the outboard midplane of the plasma (near Z = 0) to provide measurements over the radial range $0.2 < r/a < 1$ (plasma minor radius, a), as well as into the scrape-off-layer region. Each detection channel consists of 11 1-mm plasticclad- silica fibers, 40m in length, arranged in a 4:3:4 configuration (Fig. 2.28), that convey the light to a remotely located spectroscopy lab.

The high throuput spectrometers consists of a 50-mm-diam, $f/1.5$ collimating lens, 5-cm-diam interference filter, high-speed $f/0.58$ focusing lens and PIN photodiode to isolate the local beam fluorescence from the collected light signal. The interference filter is a high transmission filter that transmits light in the spectral range $\lambda = 652 - 655.5$ nm, cutting off near $D_{\alpha,o}$. The collimated beam is normally incident on the intereference filters, which are designed to also transmit a fraction of the thermal deutrium charge exhange lines on the blue side of edgh D_α emission [44] (as shown in Fig. 2.29). The filters are designed to be used at near normal incidence to reduce the spectral blurring that results from angle tuning. Specialized ultra low noise cryogenically-cooled transimpedance preamplifiers [53] convert the photodiode current to a voltage signal.Signal conditioning electronics then frequency filter and further amplify the signal. The signal is digitized using multichannel simultaneous digitizers (D-tAcq Solution Inc.) Fourteen-bit, 16-channel digitizer boards (ACQ16PCI) utilize synchronized external clocks and triggers to insure that all channels are sampled at 1 MHz on a common time-base, crucial for cross correlation and cross phase measurements.

Two common-mode rejection channels have been deployed with the recently expanded system. The common-mode channels are located approximately five and 10 cm inboard of the main channel grid, respectively. These channels are used for measurement and isolation of any fluctuation components on the neutral beam itself that do not represent local plasma fluctuations and thus should be subtracted from the measured signals [49]. Such common-mode fluctuations arise mainly from fluctuations in the neutral beam source [54], and also large-amplitude edge

fluctuations that imposed on the beam due to fluctuating beam attenuation. Such fluctuations can complicate analysis and interpretation of the measured local fluctuations. The common-mode channels allow for the identification of spectral signals that are common to all channels. The distance between two channels is larger than the radial correlation length of turbulenct eddies. Therefore, any signal common between these channels and the array can be rejected as common-mode signal.

An control system has been implemented to control timing, detector temperature control and AC power to various system components, and provide for safety of the equipment. This system consists of several National Instruments compact Field Point (cFP) components (relay, thermocouple, analog input modules) and a timing board, that have been integrated with the LabView virtual instrument software package for interface and control running on a host PC. The control system allows for fully remote operation of the BES system, system protection, and recording of diagnostic system parameters. The system controls LN2 flow to the detectors and preamplifiers to maintain a temperature near 140 K to minimize e-noise and photodiode dark current (all cooled components are located in a vacuum box to prevent condensation). Power is cycled to cryogenic solenoid valves in response to real-time temperature measurements. The timing system allows for data acquisition to commence at any point during the plasma discharge with a precision of 1 microsec. A block diagram of the detection and control system is shown in Fig. 2.26 [48].

The spatial transfer function is the measure of is the measure of how the location and relative intensity of light collected from the sample volume are collected, i.e., the measured spot size, which ultimately sets the spatial resolution of the system [55]. Therefore, proper interpretation of data requires for evaluation of the spatial transfer function . Quantification of th spatial transfer function was done [56] using the beam/optical sight line geometry, flux surface geomatry, local magnetic field pitch angle, local plasma density, local beam density profile, and atomic transition rates. The measured intensity distribution $M(\boldsymbol{x})$ of a system is determined

by the convolution of the true intensity distribution $S(\boldsymbol{x})$ with the point spread function (PSF), $P(\boldsymbol{x})$, i.e., $M(\boldsymbol{x}) = S(\boldsymbol{x}) \times P(\boldsymbol{x})$. The Fourier spatial transform of the PSF is the spatial transfer function (STF), $\tilde{T}(\boldsymbol{k}) = F\{P(\boldsymbol{x})\}$. Thus in wave-number space, the true intensity distribution can be obtained with the spatial transfer function via $\tilde{S}(\boldsymbol{k}) = \tilde{M}(\boldsymbol{k})/\tilde{T}(\boldsymbol{k})$. Here, $\tilde{S}(\boldsymbol{k})$ and $\tilde{M}(\boldsymbol{k})$ are the Fourier transforms of $S(\boldsymbol{x})$ and $M(\boldsymbol{x})$, respectively. It is more straightforward to calculate the spatial effects in the PSF in real space and transform the result to obtain the spatial transfer function in wave-number space.

Figure 2.30 (a) shows the calculated point spread function for the optical sight line which is nearly tangent to the flux surface at the left beam source at $R = 220$ cm. Here, An effective state lifetime τ of 2.5 ns was assumed, while the poloidal field pitch angle was assumed to be 5° relative to the equatrial plane (0° relative to the BES sight line). The FWHM of the radial projection is 1.15 cm compared to the ideal imaged fiber width of 0.86 cm. The FWHM of the poloidal projection is 1.3 cm compared to the fiber image of 1.25 cm. The ratio of the integrated intensity within the radial FWHM to the total intensity is 75%, while the ratio for poloidal direction is 95%. Fourier transforming the point spread function yields the spatial transfer function. The extent of the spatial transform in wave-number space is a measure of the sensitivity of the system. Shown in Fig. 2.30 (b) is the spatial transfer function obtained by Fourier transforming the point spread function shown in Fig. 2.30 (a). The e-folding distances for the radially projected spatial transfer function are 2.5 cm^{-1} and 3.3 cm^{-1} for the poloidal profection.

The dependence of the spatial transfer function on several key parameters is shown in Fig. 2.31 for a typical upper-single-null, L-mode discharge on DIII-D (#119525). As is shown in Fig. 2.31(a), reduction in effective lifetimes due to increased collisionality leads to reduction in radial FWHM of point spread function and is highly beneficial for achieving good spatial resolution. Fig. 2.31(b) shows that optimal radial resolution is achieved in the outboad region where the optical sight line is nearly tangent to the magnetic flux surface at the beamline intersection.

The dependence of the spatial transfer function on the poloidal pitch angle is illustrated in Fig. 2.31(c), showing that change in sensitivity is small within the typical pitch angle variation of $+/-5^{\circ}$ from the 5° BES sight line angle.

Parameters	Targeted value	Achieved value
Major radius	3.9 m	
Minor radius of helical coil	0.975 m	
Minor radius of plasma	0.5 - 0.65 m	
Magnetic field	3T (R=3.9 m)	2.96T (R=3.6 m)
Magnetic energy	0.90 GJ	0.77 GJ
Coil temperature	4.4 K	3.5 K
Heating power		
ECRH	10 MW	2.5 MW
ICRH	3 MW	3.0 MW
NBI	15 MW	23 MW
Steady state (ECRH+ICRH)	3 MW	1.7 MW

Table 2.1: Parameters of Large Helical Device [16].

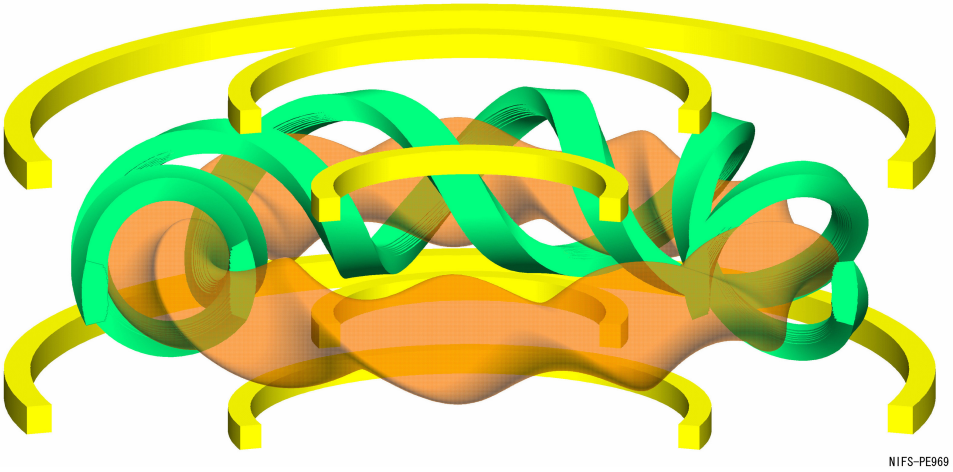

Figure 2.1: Schematic of a configuration of magnetic coils in LHD.

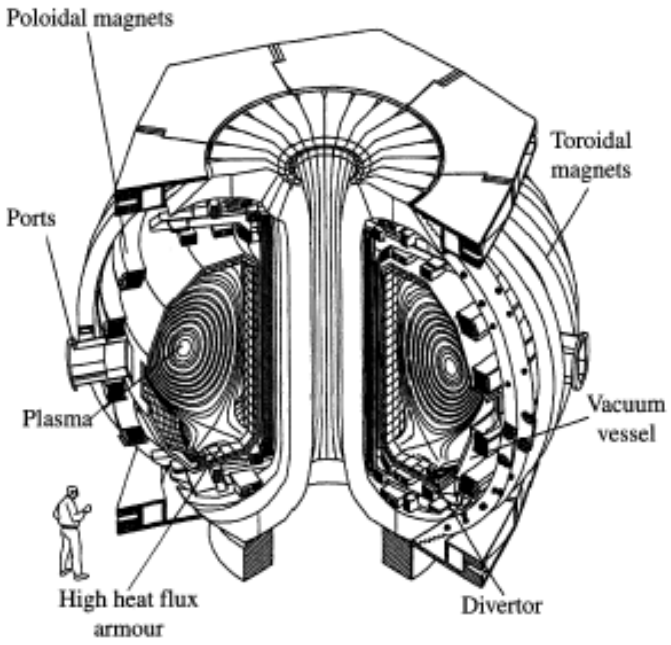

Figure 2.2: Layout of the DIII-D experiment with an inset illustration the geometry [23].

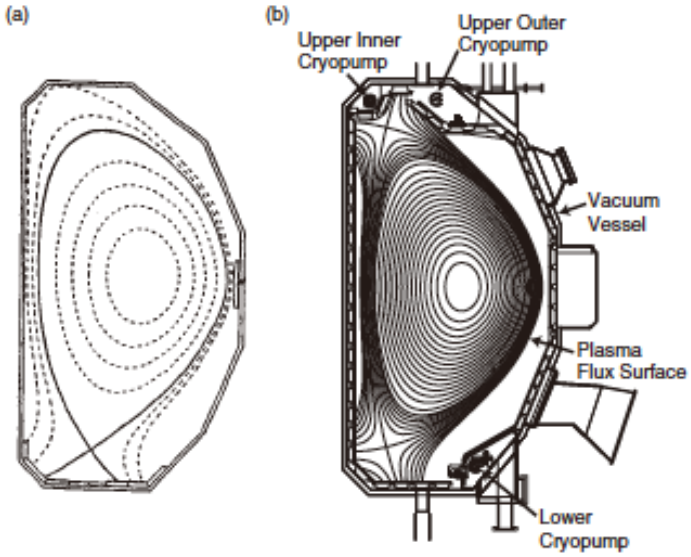

Figure 2.3: (a) A cross-section of the DIII-D vacuum vessel in 1986 with an MHD equilibrium superposed: a location between the ports is chosen. (b) Cross-section of the DIII-D vacuum vessel and typical ports in 2000 with MHD equilibrium superposed [22].

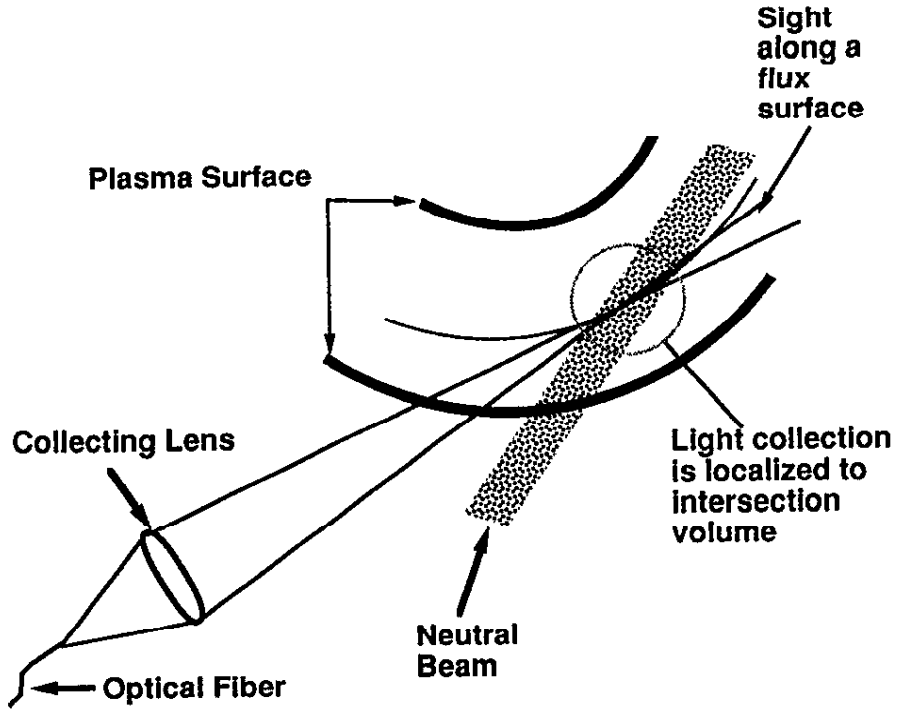

Figure 2.4: Schematic of a BES installation in TFTR [24].

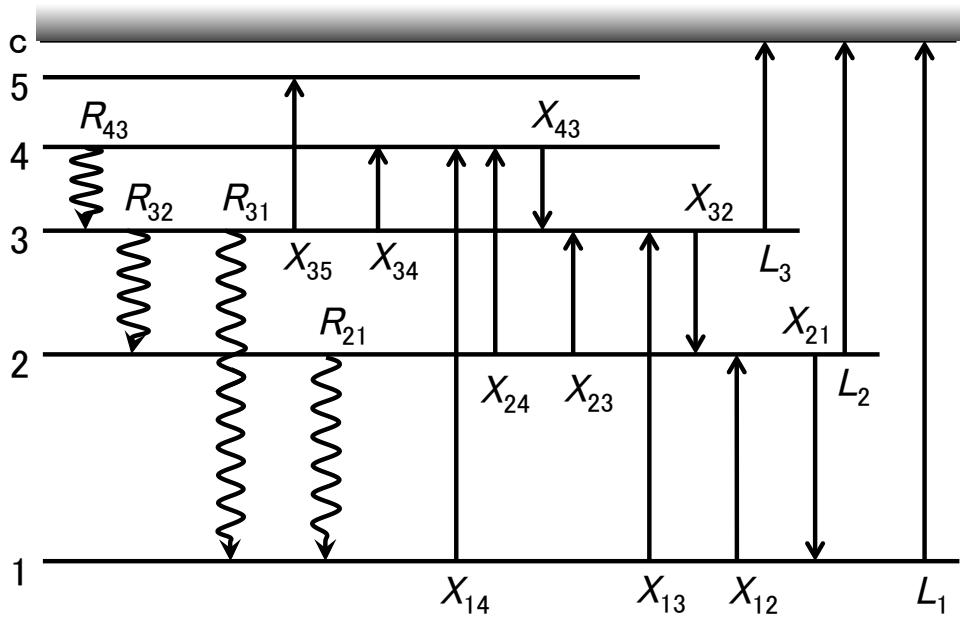

Figure 2.5: Dominant flows of electrons in the energy level diagram. ”c” denotes the continuum state.

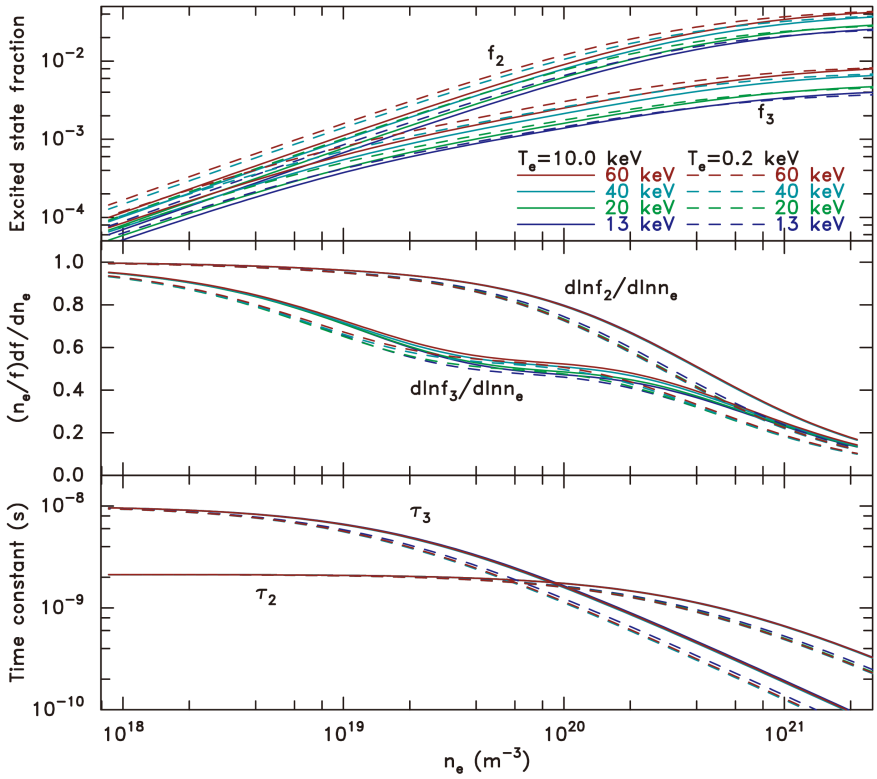

Figure 2.6: Solutions of the excited-state quantities for several beam and plasma parameters [39].

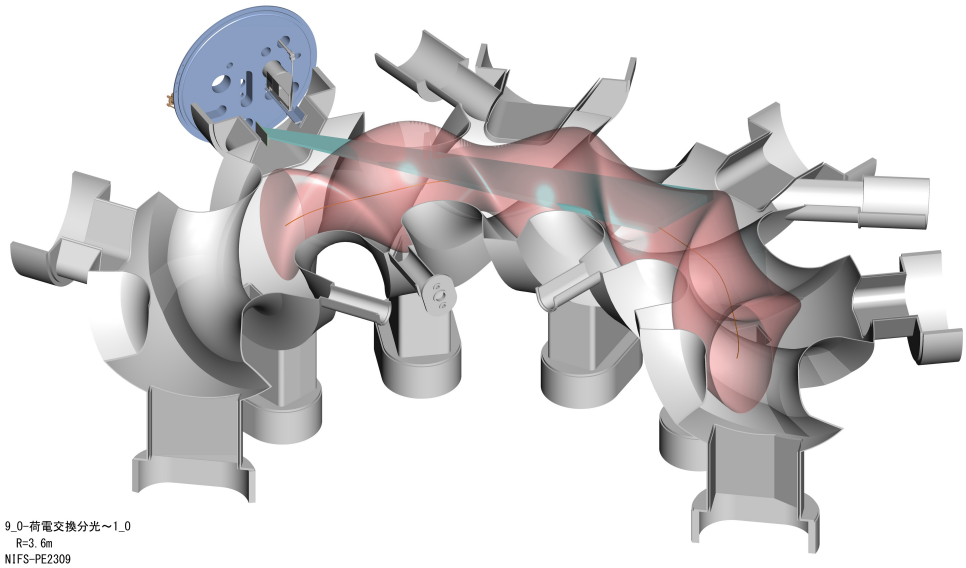

Figure 2.7: Configuration of viewing area of BES system.

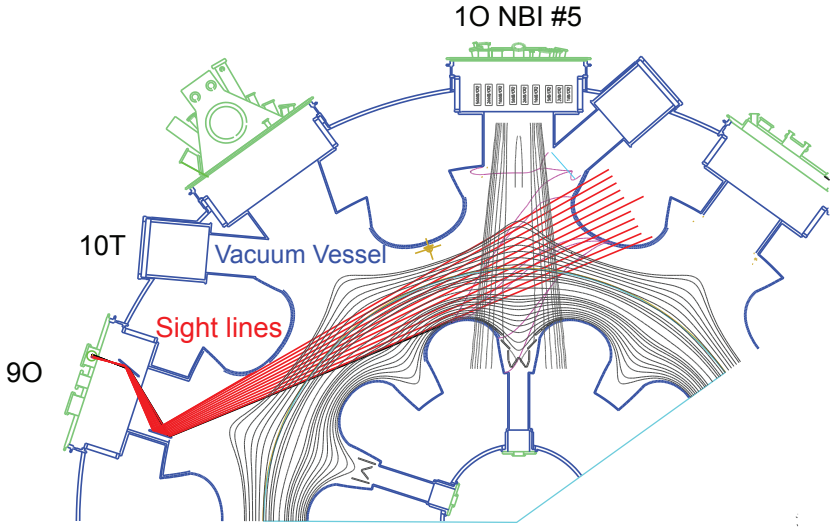

Figure 2.8: Top view of the sight lines of the BES system in LHD [45]. Red lines are some of the sight lines on the mid plane.

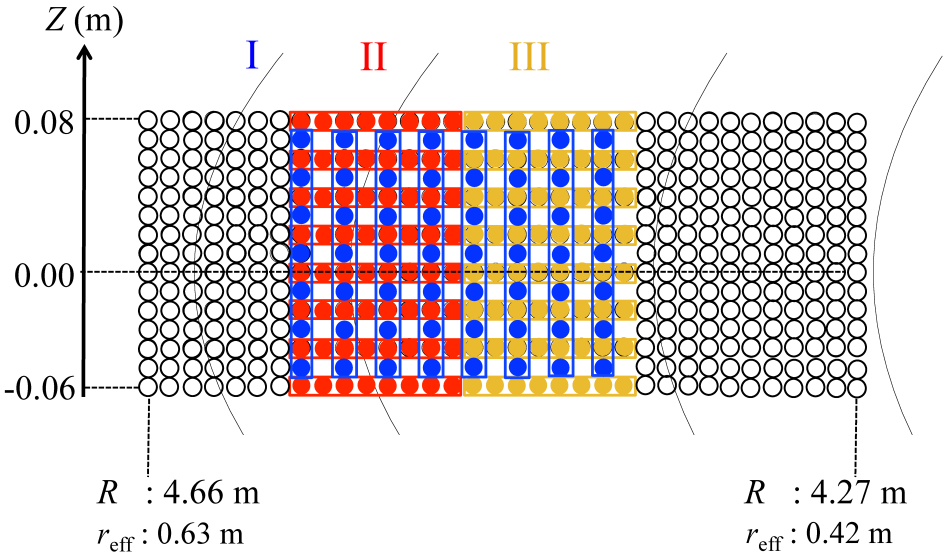

Figure 2.9: Fiber image configuration on the poloidal cross section [46]. Each channel of group I (blue circle) consists of 7 fibers making poloidally elongated slit shaped sampling area, while group II and III yield radially elongated sampling area with 8 fibers in each channel. Two types of slits are overlaid in the same area.

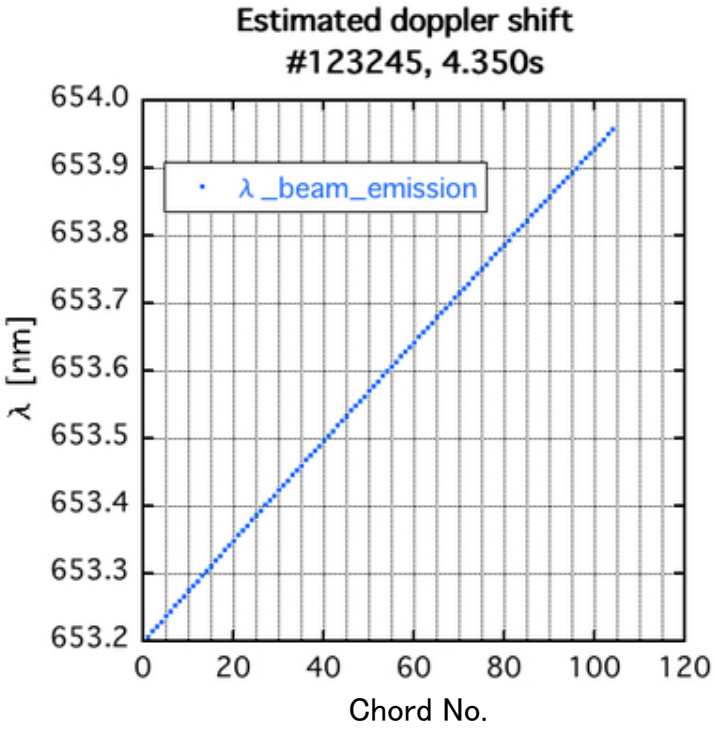

Figure 2.10: Estimation of wavelength of the Dopper shifted H_α line for each sightline cord on the mid plane. The probe beam energy is 40 keV.

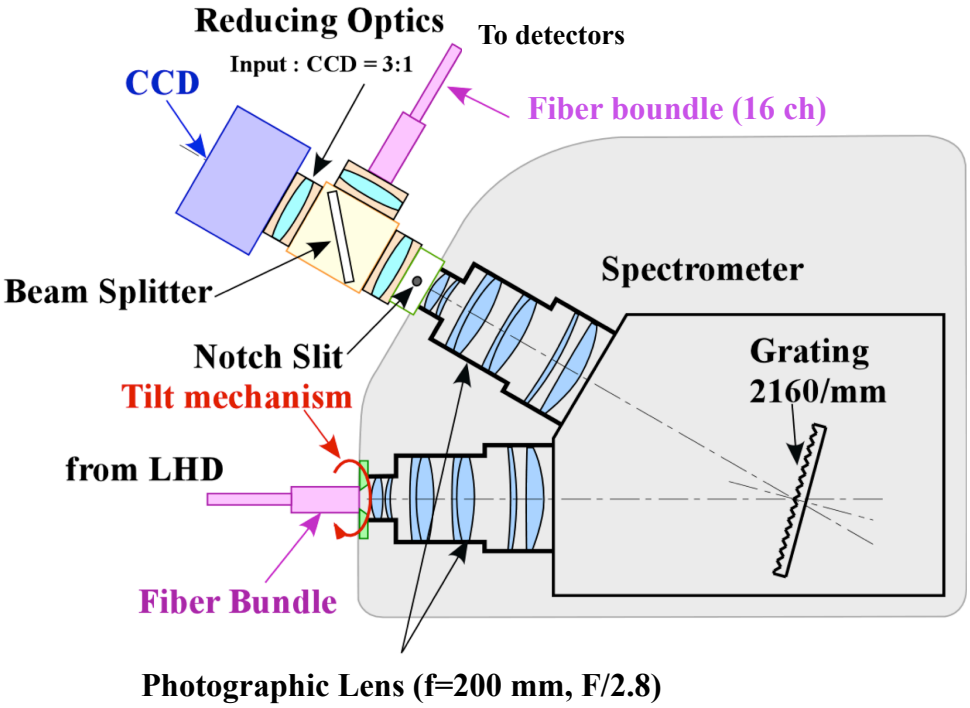

Figure 2.11: Spectrometer [42]

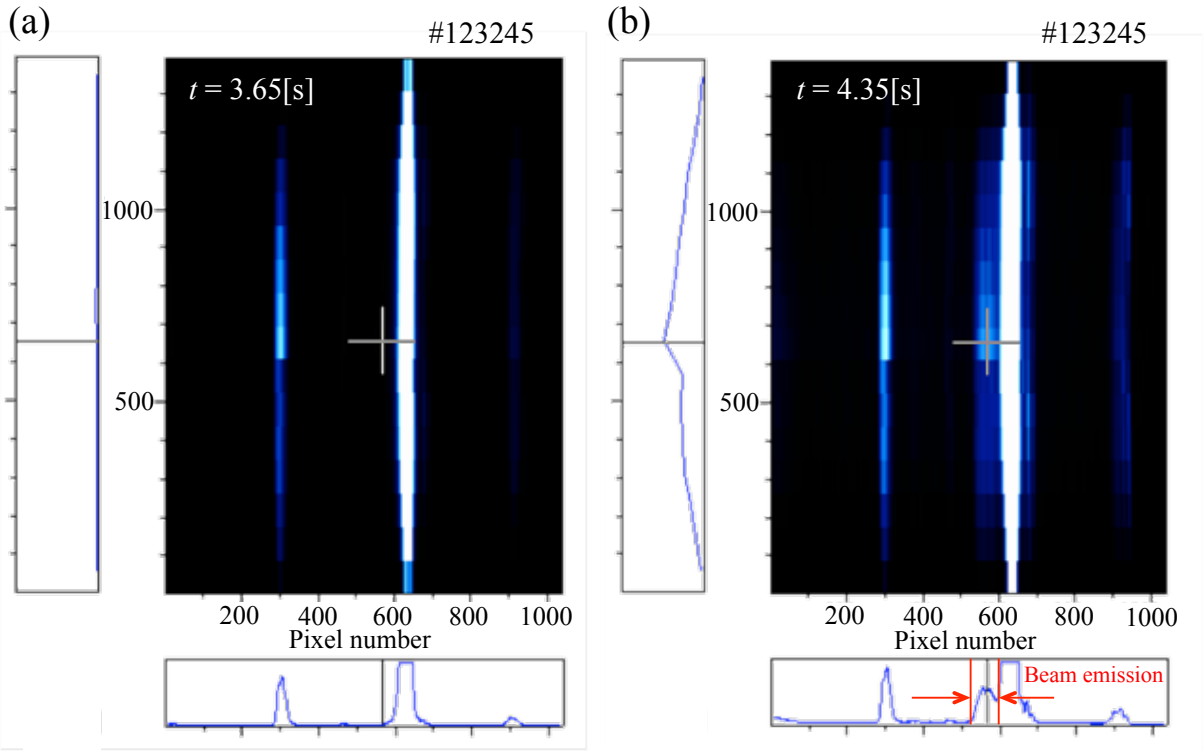

Figure 2.12: CCD image taken at the output side of the spectrometer in the case of (a) without probe beam and (b) with probe beam. Horisontal axis and vertical axis corresponds to wavelength and space, respectively. Doppler shifted beam emission is indicated with red arrows.

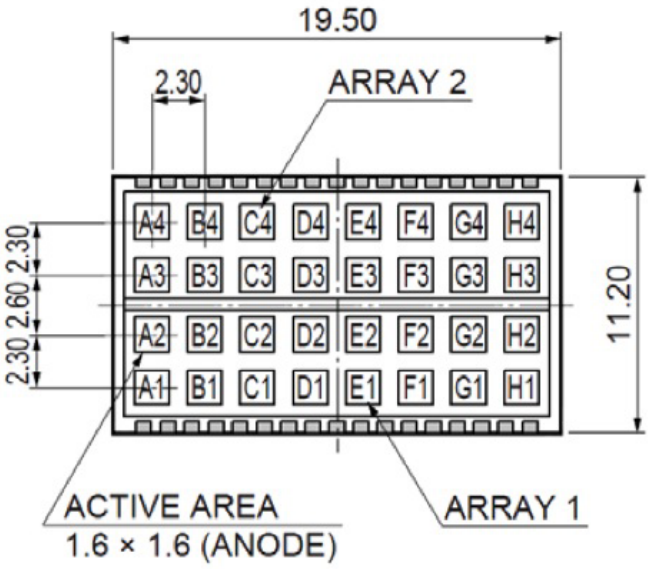

Figure 2.13: Hamamatsu S8550 APD censor array.

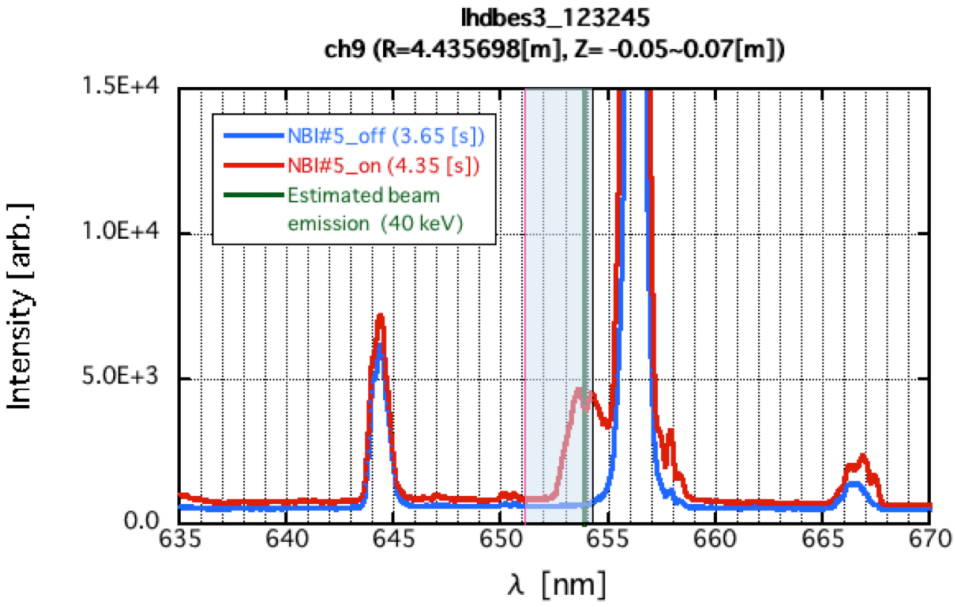

Figure 2.14: An example of spectrum of visible light from a plasma.

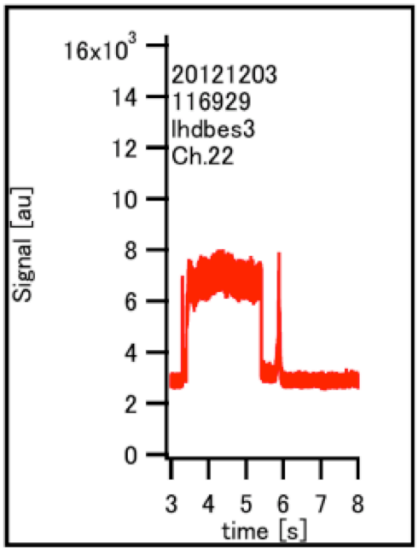

Figure 2.15: Temporal evolution of beam emission (#116929).

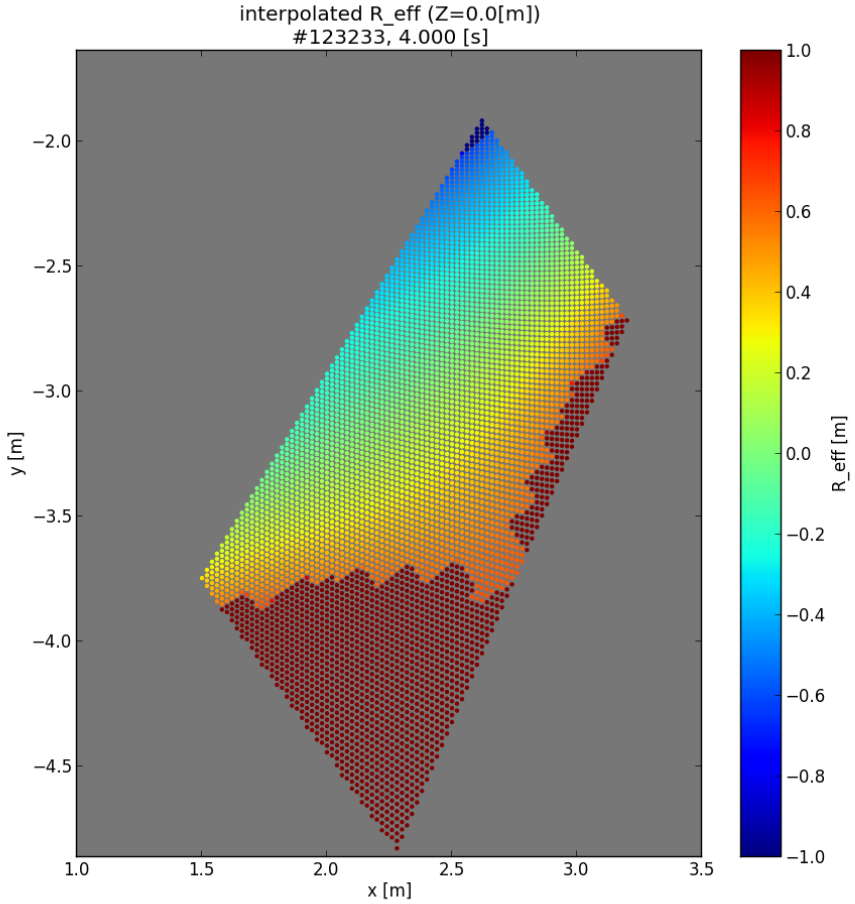

Figure 2.16: r_{eff} profile.

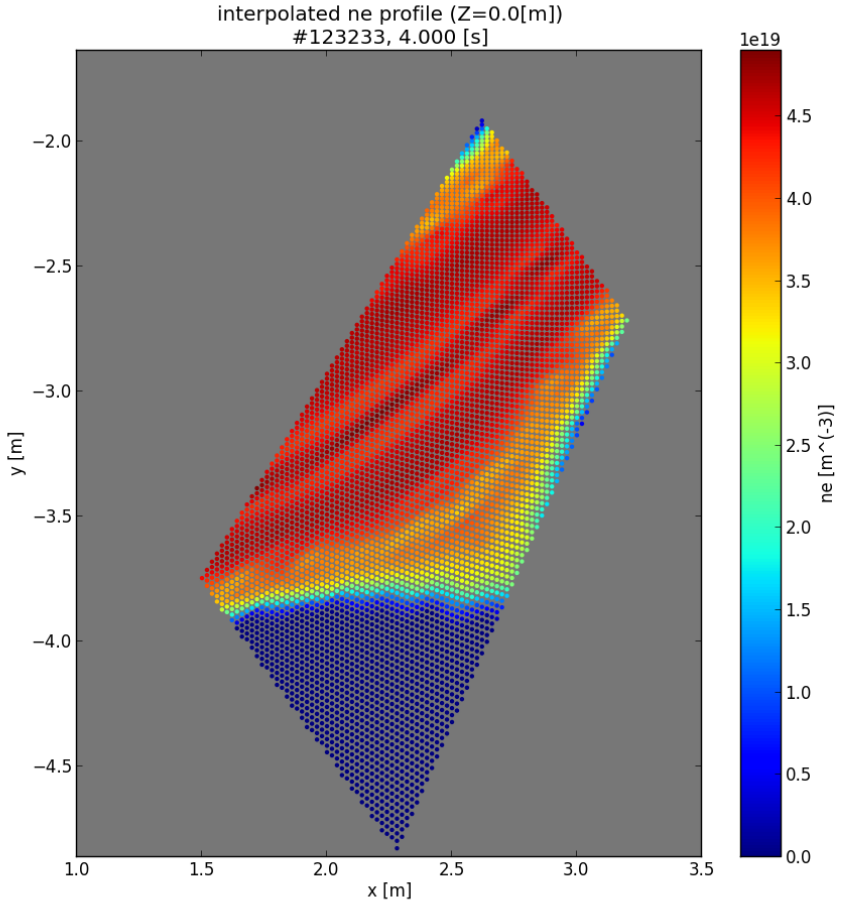

Figure 2.17: Electron density n_e profile.

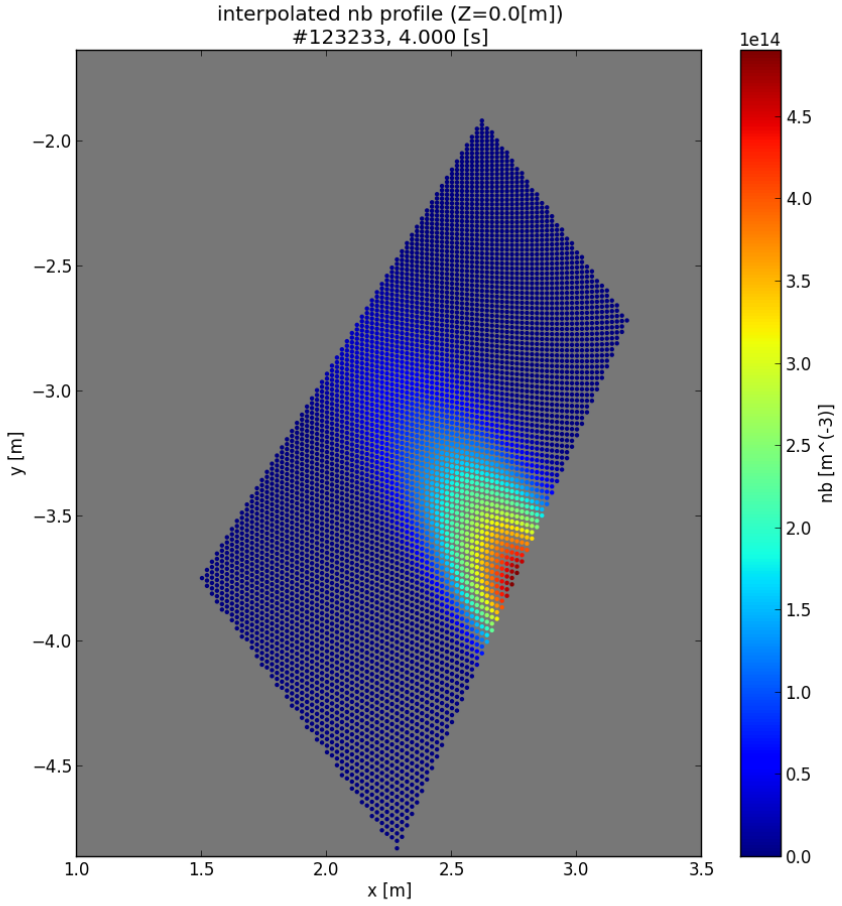

Figure 2.18: Neutral beam particle density n_{beam} profile.

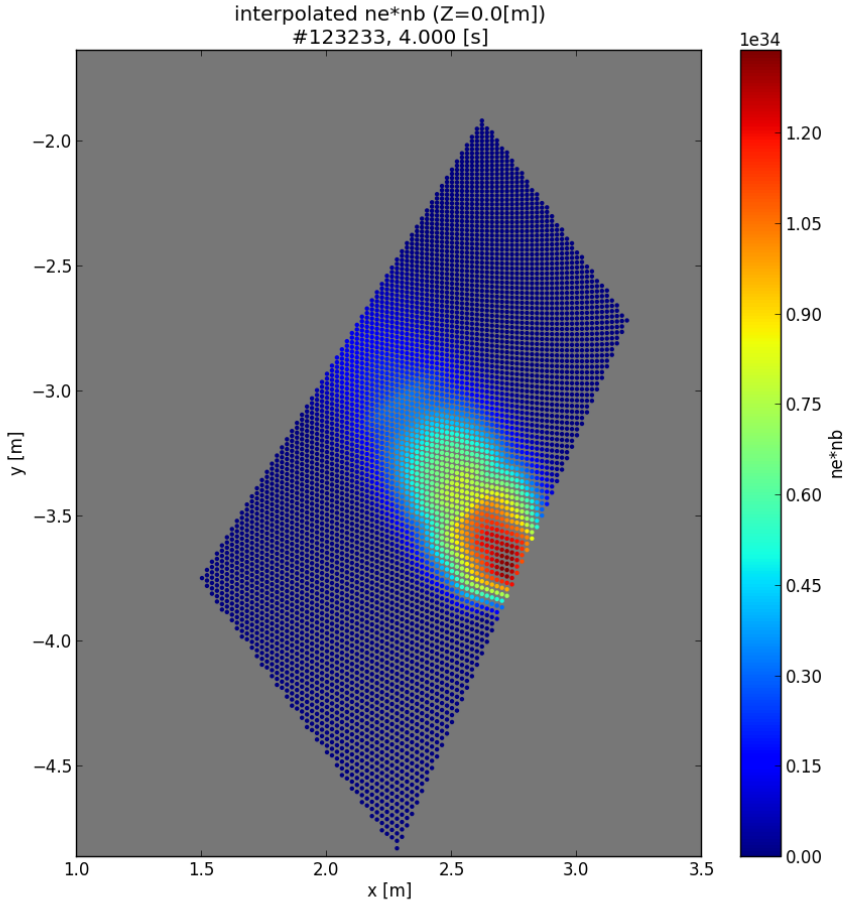

Figure 2.19: Profile of the multiple of electron and beam particle density$n_{\mathrm{e}}n_{\mathrm{beam}}$.

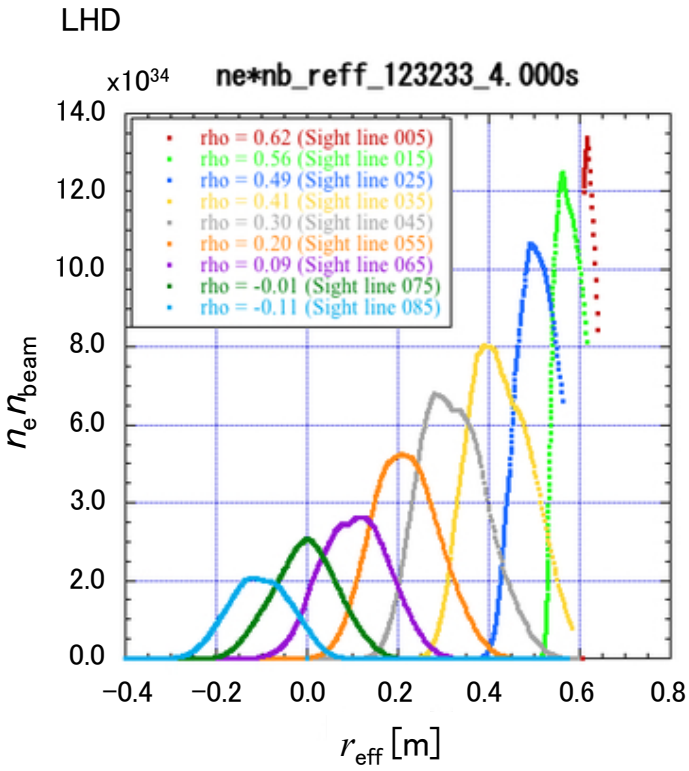

Figure 2.20: Radial profile of $n_e n_{beam}$ along sightlines on the mid plane.

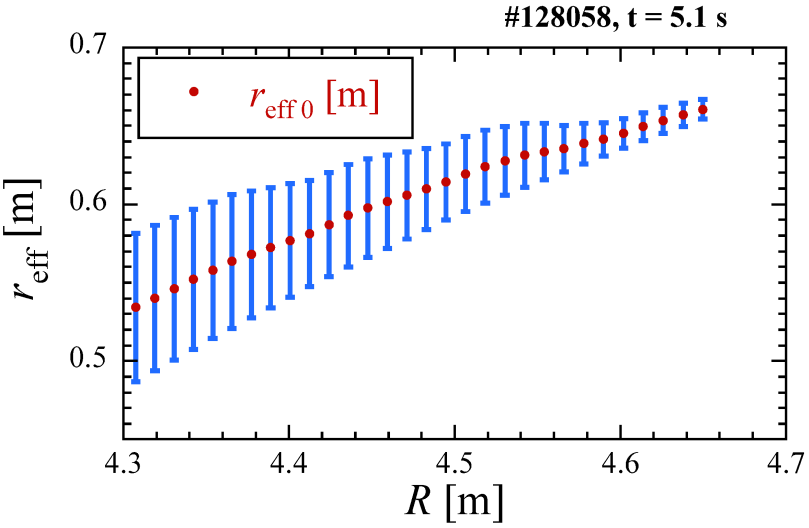

Figure 2.21: Effective minor radius, r_{eff}, at the major radius, R, where the line of sight crosses the probe beam on the mid-plane [46]. The spatial resolutions determined by the integration effect due to the finite beam width are indicated with bars.

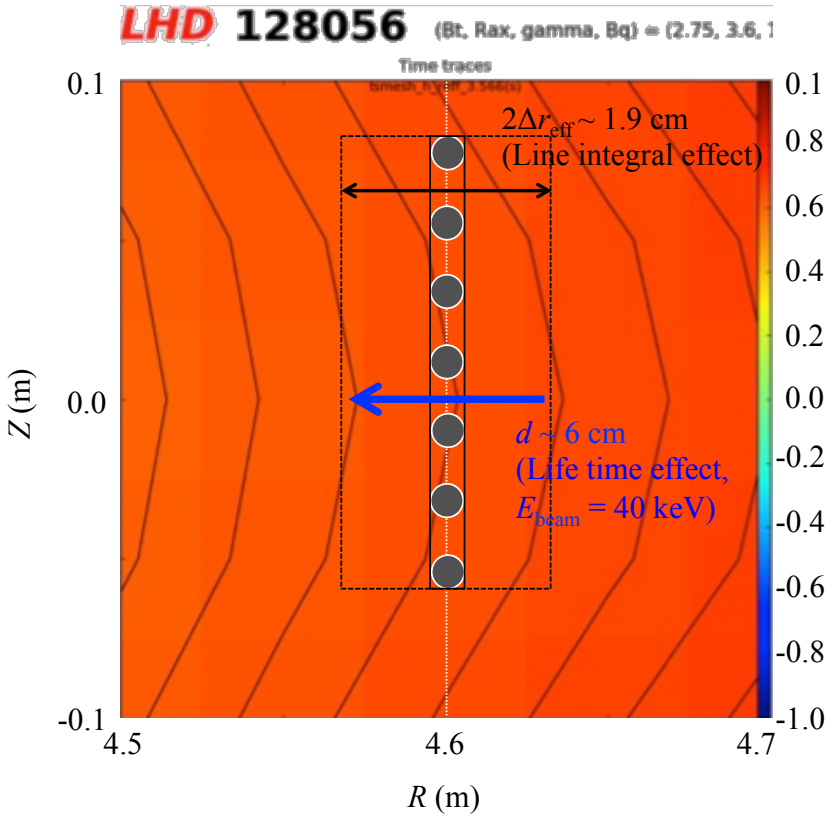

Figure 2.22: Comparison between the finite life time effect and the line integral effec [46]. The size of the displacment due to life time effect ($d \sim 6.0$cm) is shown by the blue arrow, overlaid on the contour of $r_{\rm eff}$ on the holizontally elongated poloidal cross-section. The black circles are a set of fiber images on the center of the beam. The area sorrounded by dashed lines shows the line integral effect ($\Delta r_{\rm eff} \sim 1.9$ cm).

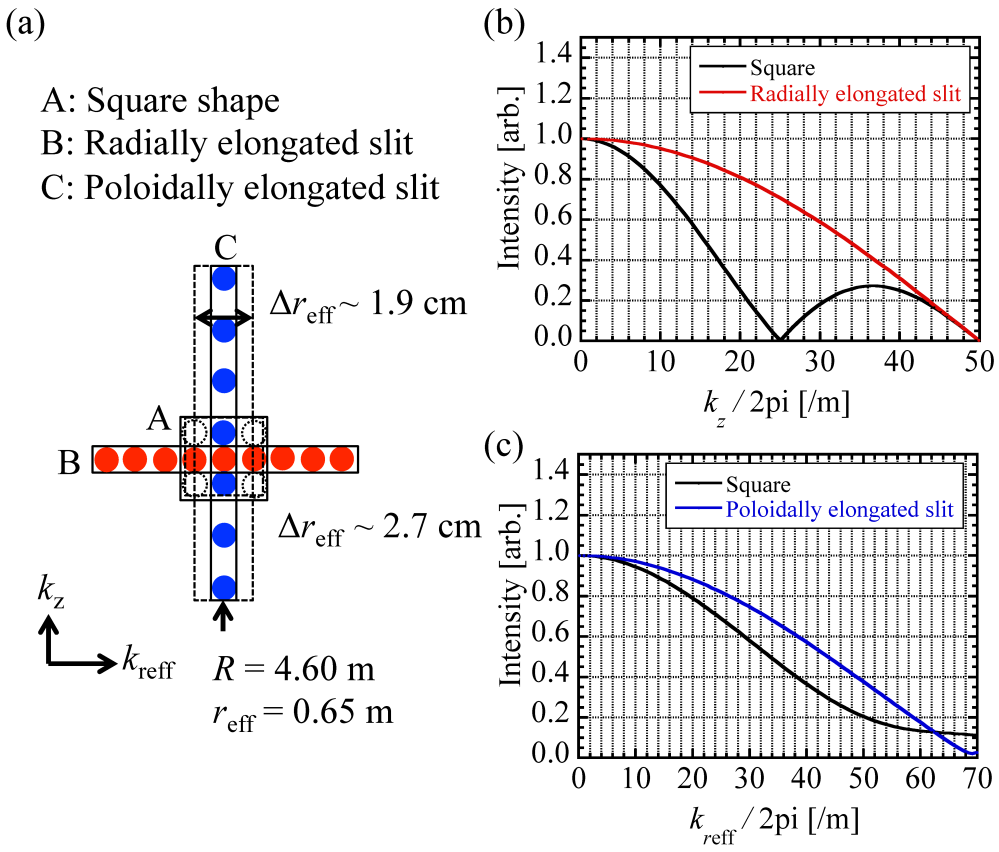

Figure 2.23: (a) Three types of fiber bundle designs. Comparisons of wavenumber sensitivity for a wave propagating in (b) poloidal direction and (c) radial direction [46].

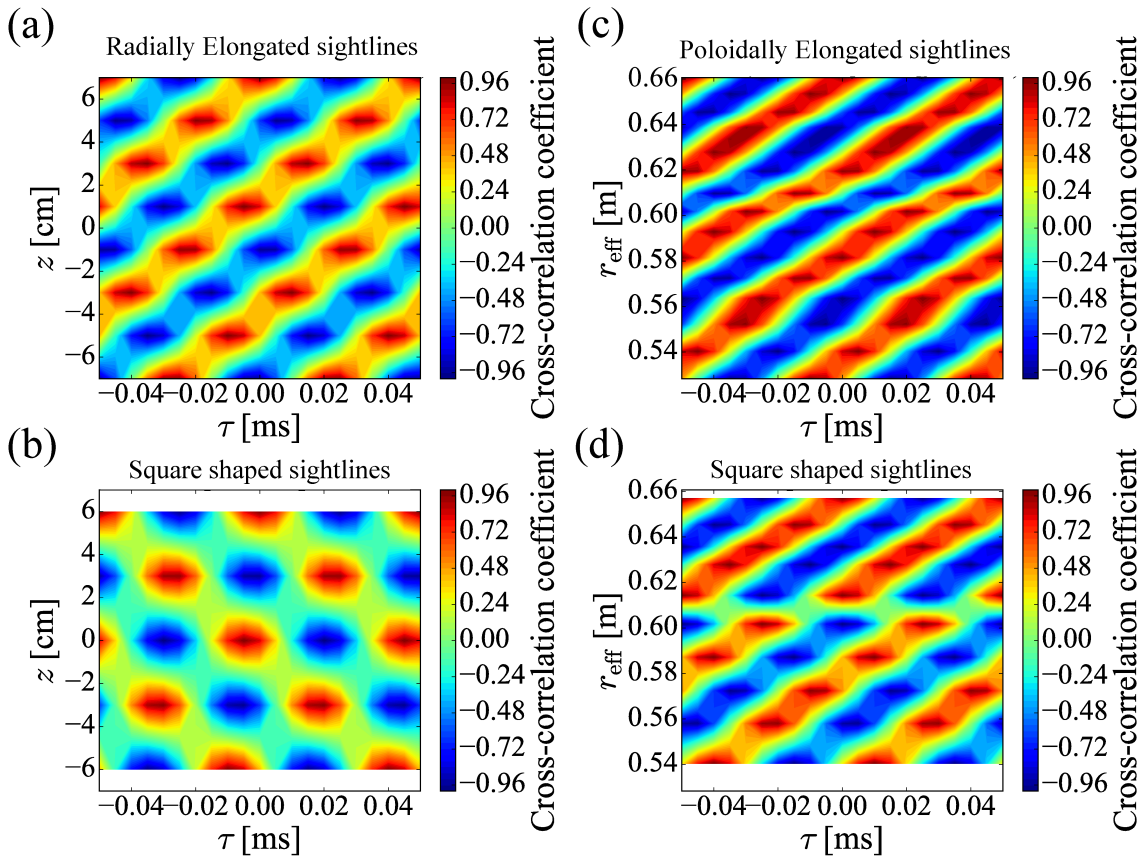

Figure 2.24: Contour plots of cross correlation function of the test wave data (f = 20 kHz, $k_{\mathrm{reff}}/2\pi$ = 20.0 m^{-1}, $k_Z/2\pi$ = 18.2 m^{-1}) in poloidal direction detected with (a) radially elongated sightlines (group II in Fig. 2.9) and (b) square shaped sightlines, and in radial direction detected with (c) poloidally elongated sightlines (group I) and (d) square shaped sightlines [46].

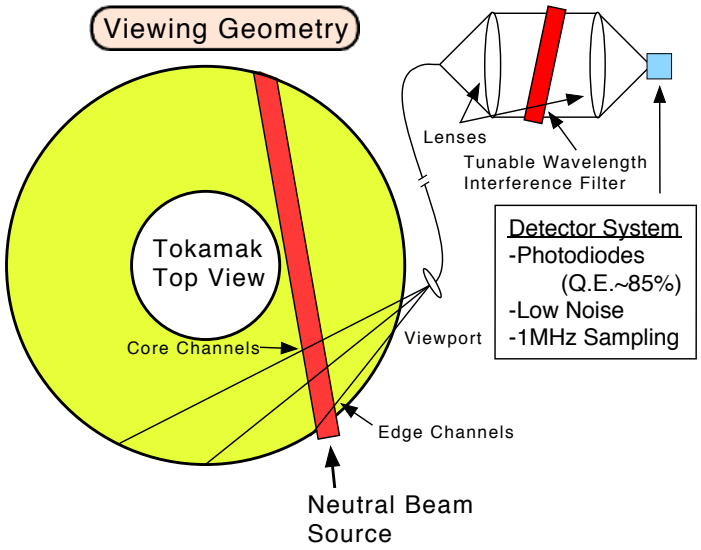

Figure 2.25: Viewing geometry and optical coupling of BES system in DIII-D.

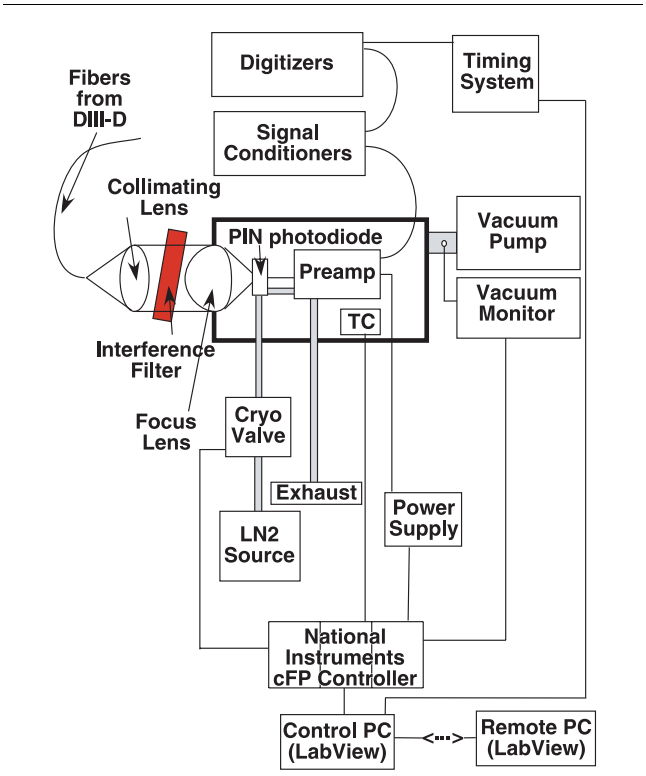

Figure 2.26: Block diagram of the main components of the Beam Emission Spectroscopy detection and control system [48].

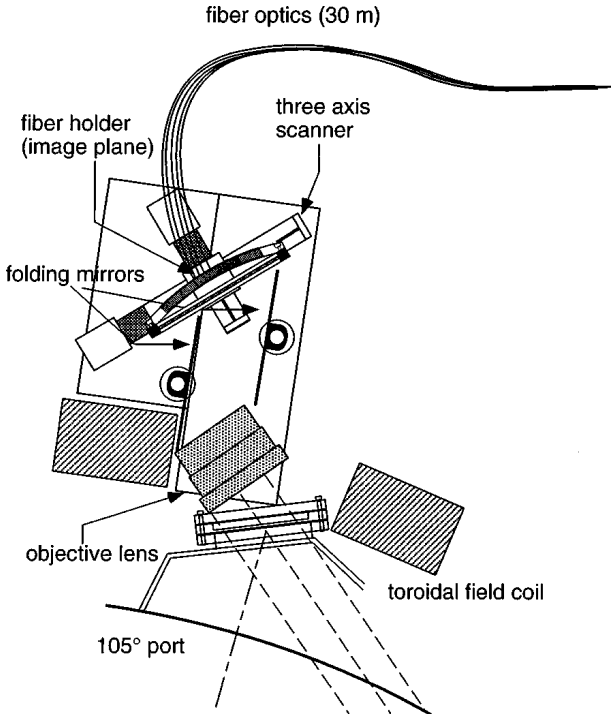

Figure 2.27: Schematic of port optics showing objective lens, folding mirrors, remotely scannable fiber mounting array, and fiber optics to remotely located spectroscopy lab [52].

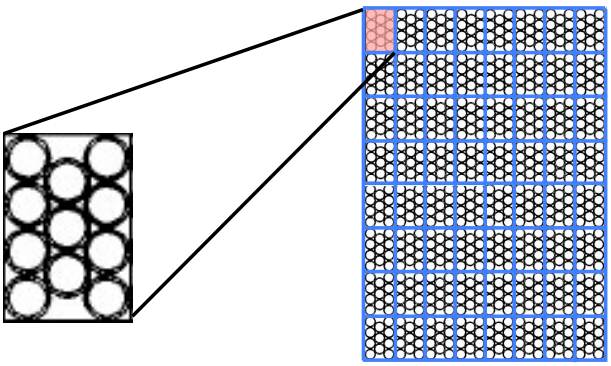

Figure 2.28: Schematic of fiber bundle configuration. 11 1-mm-diam fibers are arranged in a 4:3:4 pattern.

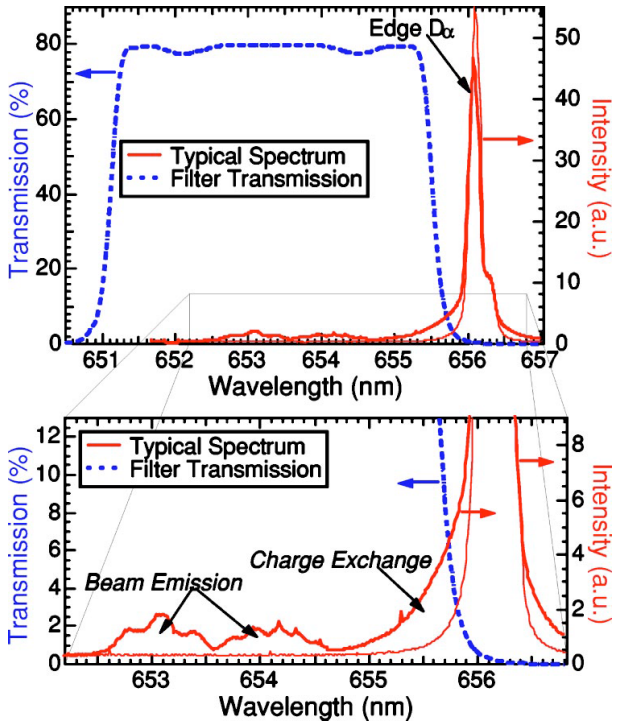

Figure 2.29: A new interference filter transmission spectrum includes Doppler-shifted beam emission as well as a significant fraction of deuterium thermal charge exchange. The filter eliminates much of the edge recycling D_α emission [44].

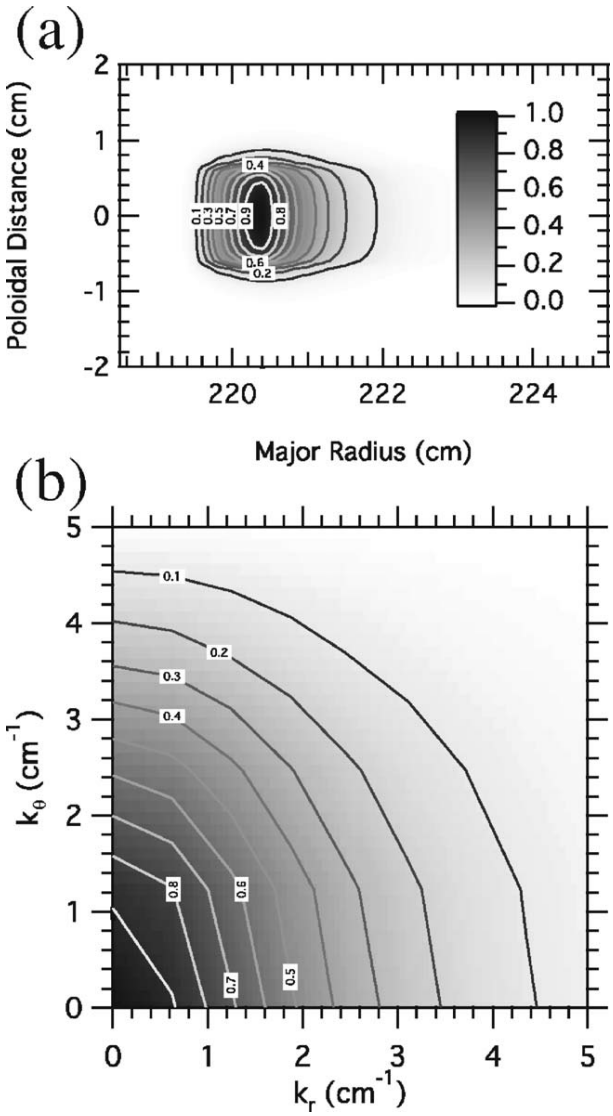

Figure 2.30: Spatial transfer function for optimal conditions. R = 220 cm, left source, $\Delta\theta = 0°$, and τ_3 = 2.5 ns. (a) 2D point spread function. (b) 2D spatial transfer function [56].

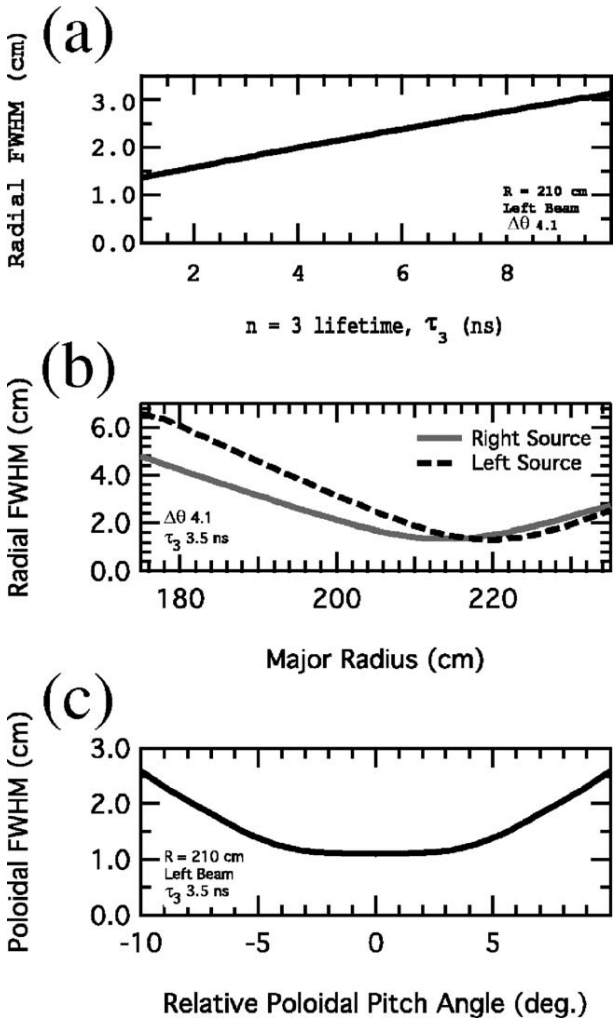

Figure 2.31: Quantification of radial and poloidal FWHMs for parameter scan. (a) Dependence of radial FWHM on the density-dependent atomic excited state lifetimes. (b) Radial FWHM vs major radius for “right” and “left” neutral beam sources viewed by BES. (c) Poloidal FWHM vs relative sight line-field line pitch angle [56].

Chapter 3

Data Analysis

Spectral analysis is a basic tool of statistical processing for analyzing spatially or temporally variable data [57]. Spectrum is essential to clarify the properties of variable data. In order to investigate properties of stationary random variable or existence of sertain periodic motions, analyses based on Fourier series (transform) are used. Spectrum is defined as magnitudes of each coefficient of expanded Fourier series from signals recorded as a time series, and the magnitudes correspond to the waves' energies of each frequencies. Correlation function is an index to quantificate a similality of certain two signals. Correlation function is defined in a real time cordinate, and its Fourier transform is equivalent to spectrum.

3.1 Fourier Transform

Frequency power spectral analysis using one-dimensional Fast Fourier Transform

Spectrum A variable $x(t)$ is If we define $X(f)$ as a Fourier transform of a variable $x(t)$,

$$X(f) = \int_0^\infty x(t)e^{-i2\pi ft}dt. \tag{3.1}$$

Then power spectrum density function $P(f)$ can be written as

$$P(f) = \lim_{T\to\infty}\left[\frac{1}{T}|X(f)|^2\right] = \lim_{T\to\infty}\left[\frac{1}{T}X(f)X^*(f)\right] \tag{3.2}$$

Considering random variable denoted by $x(t)$, the energy per unit time (mean power) of the variable $\bar{x^2}$ is written as

$$\bar{x^2} = \lim_{T\to\infty}\int_{-T/2}^{T/2} x^2(t)dt. \tag{3.3}$$

Spectrum $P(f)df$ means a contribution rate of a wave component in the frequency range from f to $f + df$ to the energy of variation $\bar{x^2}$, and this notion can be written as

$$\bar{x^2} = \int_{-\infty}^{\infty} P(f)df. \tag{3.4}$$

$P(f)$ called two-sided spectrum is a spectrum which is defined in the frequency range of $(-\infty, \infty)$. Howevere, it is convenient to define the frequency range as $(0, \infty)$ for experimental or analytical usage. In this case, one-sided spectrum $E(f) = 2P(f)$ is defined.

Let $X(k)$ be a finite discrete Fourier transform of $x(j)(j = 0, 1, 2, ..., N-1)$

$$X(k) = \sum_{j=0}^{N-1} x(j)\exp\left[-i2\pi\cdot\frac{k}{T}\cdot\frac{jT}{N}\right]\cdot\frac{T}{N} = \sum_{j=0}^{N-1} x(j)\exp\left[-i2\pi\cdot\frac{jk}{N}\right]\cdot\frac{T}{N}\ (k = 0, 1, 2, ..., N/2) \tag{3.5}$$

where,

- $\Delta t = T/N$,
- $\Delta f = 1/T$,
- $t = j\Delta t = j(T/N)$,
- $f = k\Delta f = k/T = k(N\Delta t)$,
- $f_N = N/(2T) = 1/(2\Delta t)$.

Here, from a condition that the frequency range is smaller than the Nyquist frequency ($f < f_{\mathrm{N}}$) the range for k is determined as

$$|k| \leq \frac{N}{2} \tag{3.6}$$

That is the number of Fourier components is half of the number of data. In FFT programs, a calculation omitting $\Delta t (= T/N)$ is usually done as

$$A_k + iB_k = \sum_{j=0}^{N-1} x(j) \left[\cos\left(2\pi j \frac{k}{N}\right) + i \sin\left(2\pi j \frac{k}{N}\right) \right]. \tag{3.7}$$

Therefore, the real and imaginary part of $X(k) = X_r(k) + iX_i(k)$ are the multiple of A_k and T/N (or $-(T/N)$), and the multiple of B_k and T/N (or $-(T/N)$), respectively.

$$\begin{aligned} X_r(k) &= \tfrac{T}{N} A_k \\ X_i(k) &= -\tfrac{T}{N} B_k \end{aligned} \tag{3.8}$$

From Eq. 3.2 spectrum is given by Fourier transform of $x(t)$ as

$$\tilde{P}\left(\frac{k}{T}\right) = \frac{1}{T} E\left[X(k)X^*(k)\right] = \frac{1}{T} E\left[|X(k)|^2\right] \tag{3.9}$$

or

$$\tilde{P}\left(\frac{k}{T}\right) = \frac{T}{N^2} E\left[A_k^2 + B_k^2\right] = \frac{\Delta t}{N} E\left[A_k^2 + B_k^2\right] \tag{3.10}$$

where $E[\,]$ denotes the ensemble average.

Smoothing by using window functions The method using FFT assumes that signals bounded by the period of time Δt is repeated periodically out of the period of time. When the difference between the start point and the end point of the quarried data, discontinuous points occurs in the repeated data series, producing errors in a spectrum if FFT is applied(Gibbs phenomenon).

To avoid the effect of the discontinuous points, it is needed to reduce the difference between the start point and the end point. For this purpose, a window function is applied to data set, and there are several type of window functions (Fig. 3.1). Window functions WF_n for data with the number of N are defined as:

- Hanning window:

$$WF_n = 0.5 - 0.5\cos\left(\frac{2\pi n}{N-1}\right) \; 0 \le n \le N-1 \tag{3.11}$$

- Hamming:

$$WF_n = 0.54 - 0.46\cos\left(\frac{2\pi n}{N-1}\right) \; 0 \le n \le N-1 \tag{3.12}$$

- Blackman window:

$$WF_n = 0.42 - 0.5\cos\left(\frac{2\pi n}{N-1}\right) + 0.08\cos\left(\frac{4\pi n}{N-1}\right) \; 0 \le n \le N-1 \tag{3.13}$$

Taking multiple of a quarried data and a window function, the difference between both ends of the data can be minimized. In this research, the humming window is used for its better frequency resolution.

Smoothing of raw spectra (ensemble averaging) To calculate coherence function, to be mentioned later, it is required to averaging spectra in time domain. For this time averaging, the process below is done to the data produced by FFT. After all the time series are devided into l, FFT is appled to each section to get spectra, then all the spectra are averaged

$$\tilde{P}\left(\frac{k}{T}\right) = \frac{1}{l}\left[\tilde{P}_1\left(\frac{k}{T}\right) + \tilde{P}_2\left(\frac{k}{T}\right) + \cdots + \tilde{P}_l\left(\frac{k}{T}\right)\right]. \tag{3.14}$$

Calculation algorithm In this research, frequency power spectral analysis has been done through the procedure below on time series data of digitized beam emission intensity by APD-CAM.

1. Determine the time width T for spectral analysis from accuired data. On the determination of the time width, it is considered that the statistical property does not change in T and that frequency resolution is determined as $\Delta f_{res} = 1/T$.

2. Apply a window function to the data. Multiple the window function (Eq. 3.12) with $N = T/f_s$ to the quarried data with the time width of T. Here, f_s is the sampling frequency.

3. Apply FFT to the data.

4. Repeat the above procedure over the time range in which statistical property dose not change, then take an ensemble average.

For example, used values for analysis in Sec. 4.1.1 are: $\Delta t = 5\ \mu$s, $T = 10$ ms. For this case, Nyquist frequency and frequency resolution are $f_{\mathrm{N}} = 1/(2\Delta t) = 100$ kHz and $\Delta f_{\mathrm{res}} = 1/T = 100$ Hz, respectively.

Cross correlation function

Cross correlation function characterizes the correlation between two variables of $x(t)$ and $y(t)$ quantitatively. Cross correlation function $C_{xy}(\tau)$ and cross correlation coefficient $R_{xy}(\tau)$ are defined as [57]

$$C_{xy}(\tau) = \overline{x(t)y(t+\tau)} = \lim_{T\to\infty} \int_{-T/2}^{T/2} x(t)y(t+\tau)dt \tag{3.15}$$

and

$$R_{xy}(\tau) = \frac{C_{xy}(\tau)}{C_x(0)C_y(0)} = \frac{\overline{x(t)y(t+\tau)}}{\sqrt{\bar{x^2}}\sqrt{\bar{y^2}}} \tag{3.16}$$

, where $C_x(\tau)$ and $C_y(\tau)$ are auto correlation functions of $x(t)$ and $y(t)$. From Eq. 3.15, cross correlation function satisfies $C_{xy}(\tau) = C_{yx}(-\tau)$, then coross correlation coefficient stays in the range of $-1 \leq R_{xy}(\tau) \leq 1$. Cross correlation coefficient is a quantified index of relevance between two signals when the signals have time delay of τ.

Coherence analysis by using FFT

Cross spectrum Let $X(f)$ and $Y(f)$ be Fourier components of $x(t)$ and $y(t)$, then cross spectrum is given as

$$\hat{P}_{XY}(f) = \frac{1}{T} E\left[X^*(k)Y(k)\right] = \frac{T}{N^2} E\left[(A_X(k) + iB_X(k))(A_Y(k) - iB_Y(k))\right], \tag{3.17}$$

where

- $A_X(k)$, $B_X(k)$: Ensemble averaged real part and imaginary part of Fourier component of $x(t)$
- $A_Y(k)$, $B_Y(k)$: Ensemble averaged real part and imaginary part of Fourier component of $y(t)$.

Procedure for calculating the cross spectrum is the same as the auto spectrum.

Cross coherence Cross coherence is used to indicate the relative intensity of correlation between two signals x,y. This quantity is defined as

$$\mathrm{Coh}_{XY}(f) = \frac{\left|\hat{P}_{XY}(f)\right|}{\sqrt{\hat{P}_X(f)\hat{P}_Y(f)}}, \tag{3.18}$$

where P_X and P_Y are auto power spectrum of x and y, respectively. For the calculation, the power spectrum $\hat{P}_X(f)$, $\hat{P}_Y(f)$ and $\hat{P}_{XY}(f)$ are needed to be ensemble averaged over several windows. The cross coherence takes the value from zero to unity since the absolute value of cross spectrum is normalized by the maximum value of it.

Spatiotemporal correlation function

Spatiotemporal correlation function is used to indicate the correlation between two variables at different time and location. For two variables of $\zeta(x, t)$ at point x and time t and $\zeta(x + r, t + \tau)$ at

point $(x + r)$ and time $(t + \tau)$, the function is defined as

$$\boldsymbol{H(x, r; t, \tau) = \overline{\zeta(x, t)\zeta(x + r, t + \tau)}.} \tag{3.19}$$

3.2 Maximum Entropy Method

MEM is a method to determine a spectrum which maximizes information entropy on auto corelation function [47]. Here, the information entropy is a degree of disorder the information. The entropy is proportional to the integral of the logarithm of the spectrum,

$$H \propto \int_{-k_N}^{k_N} \log P(k) dk. \tag{3.20}$$

The entropy is maximized when the random variable x obeys the Gaussian distribution.

The spectrum by MEM is expressed as

$$P(k) = \frac{P_M \Delta x}{\left|1 + \sum_{m=1}^{M} a_M e^{-i2\pi k m \Delta x}\right|^2}, \tag{3.21}$$

where $M, k, and \Delta x$ are the maximum value of the lag in the auto correlation function C_M, the wavenumber and the sampling interval, respectivly.The parameters a_M are the Lagrange multipliers which are the solution of the Yule-Waker equation

$$\begin{pmatrix} C_0 & C_1 & \dots & C_M \\ C_1 & C_0 & \dots & C_{M-1} \\ \vdots & \vdots & \ddots & \vdots \\ C_M & C_{M-1} & \dots & C_0 \end{pmatrix} \begin{pmatrix} 1 \\ a_1 \\ \vdots \\ a_M \end{pmatrix} = \begin{pmatrix} P_M \\ 0 \\ \vdots \\ 0 \end{pmatrix}. \tag{3.22}$$

The autocorrealtion C_m at the lag M is

$$C_m = \frac{1}{N} \sum_{n=1}^{N-m} x(n) x(n + m). \tag{3.23}$$

3.3 Hilbert Transform

Hilbert transform provides sinusoidal component of a signal that is assumed to be cosinusoidal component [59]. This is realized with Fourier decomposition and inverse Fourier decomposition. First, the target signal is processed by Fourier decomposition, and Fourier components as a function of frequency are given. Then, the calculated phase of each elementary wave component at each frequency is delayed for $\pi/2$, and then inverse Fourier decomposition returns Fourier components to time series. Using Hilbert transform, instant value of complex wave component can be calculated as,

$$y(t) = \sqrt{x^2(t) + h[x(t)]^2} \exp\left[i \tan^{-1}\left(\frac{h[x(t)]}{x(t)} \right) \right] \tag{3.24}$$

where $h[*]$ shows Hilbert transform. Real part of y (t) is equivalent to the original time series $x(t)$. This complex wave component can be treated equally with Fourier or wavelet component.

3.4 Bicoherence and Biphase

Auto bicoherence,

$$\hat{b}_{XXX}(f_1, f_2) = \frac{\left| \hat{B}_{XXX}(f_1, f_2) \right|}{\sqrt{\left\langle |X(f_1)X(f_2)|^2 \right\rangle \left\langle |X(f_3)|^2 \right\rangle}}, \tag{3.25}$$

indicates the relative strength of nonlinear coupling among three waves that satisfy the matching condition [59]. Squared auto bicoherence is defined as,

$$\hat{b}^2_{XXX}(f_1, f_2) = \frac{\left| \hat{B}_{XXX}(f_1, f_2) \right|^2}{\left\langle |X(f_1)X(f_2)|^2 \right\rangle \left\langle |X(f_3)|^2 \right\rangle}. \tag{3.26}$$

The squared auto bicoherence has a value between zero and unity since it is defined as a normalized absolute bispectrum. If there is a strong three-wave coupling, the phase relation among three waves is almost conserved and the squared bicoherence approaches to unity. In contrast,

if there is no three-wave coupling, the absolute value of bispectrum at numerator becomes zero and squared auto bicoherence becomes zero. The squared cross bicoherence for $X(f)$ and $Y(f)$

$$\hat{b}^2_{XXY}(f_1, f_2) = \frac{\left|\hat{B}_{XXY}(f_1, f_2)\right|^2}{\left\langle |X(f_1)X(f_2)|^2 \right\rangle \left\langle |Y(f_3)|^2 \right\rangle}, \tag{3.27}$$

can also be defined. There are four types of auto and cross bicoherence, namely, $\hat{b}^2_{XXX}(f_1, f_2)$, $\hat{b}^2_{YYY}(f_1, f_2)$, $\hat{b}^2_{XXY}(f_1, f_2)$, $\hat{b}^2_{YYX}(f_1, f_2)$.

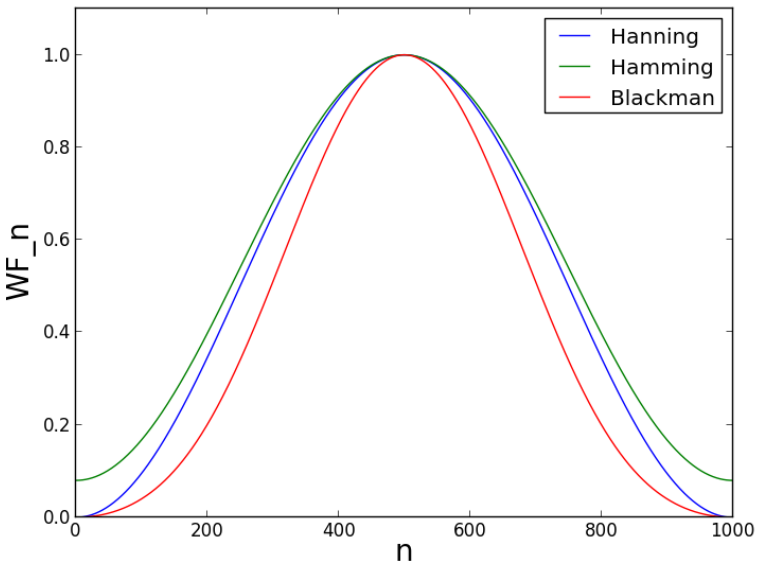

Figure 3.1: Comparison of window functions (N=1000).

Chapter 4

Coupling Between Edge Harmonic Oscillation (EHO) and Turbulence

4.1 Low Frequency Density Fluctuation Driven by MHD instability

4.1.1 EHO of density fluctuations

Figure 4.1 shows the typical experimental conditions and temporal evolution of plasma parameters for a discharge in which the low-frequency fluctuation appears. Additional gas was puffed to increase density. The target high β plasma which is produced with two NBIs of a total power of 10 MW in the most of time. Correlation analysis is applied during the quiet period in $3.9 < t < 4.8$ s, which is shown by the yellow shade in Fig. . The density fluctuations are observed with the BES. Figure 4.2 (a) and (b) show the temporal evolution of auto-power spectrum of the beam emission and that of neutral beam power. Figure 4.3 demonstrates the mean frequency auto power spectrum of beam emission. The frequency peak of the beam emission was observed at 1.4 kHz with a smaller peak at 2.8 kHz, and similar peaks are found in the

magnetic fluctuation $\tilde{B}$ as shown Fig. 4.4.

The level of density fluctuations was quite weak. However, the BES signals have unambiguous cross-correlation with magnetic probe signals. In Fig. 4.5, the squared cross-coherence shows peaks at $f \sim 1.4$ kHz and $f \sim 2.8$ kHz. High cross-correlation between the density and magnetic fluctuations shown here indicates that the oscillation may be MHD modes. The radial profile of the coherence for the low frequency modes (1.4 kHz and 2.8 kHz) is shown in Figure 4.6. Significant coherence values are observed at $r_{\mathrm{eff}} \sim 0.56$ m.

4.1.2 Spatiotemporal Structure of EHO

Spetio-temporal structure of the fluctuation has been used to investigate the propagation behavior of the mode. In this analysis, the magnetic signal is used as a reference, and this leads to more distinct results due to its high intensity. Spatiotemporal structure of density fluctuations is determined by a two-point two-time correlation function at a different position. Two-point two-time correlation function between BES signals and the magnetic signals can be given as Eq. 3.19. Figures 4.7 (a) and (b) show a contour plot of correlation functions of the density fluctuation of the fundamental frequency component $f = 1.4$kHz with the magnetic fluctuation as a reference signal in the poloidal and the radial direction, respectively. The correlation functions are calculated with a time window of 3.0 ms and are ensemble-averaged for 299 samples during the quiet period in $3.9 < t < 4.8$ s. For the fluctuation component at $f \sim 1.4$ kHz, the fluctuation structure is found to propagate in the electron diamagnetic drift direction which corresponds to the $E \times B$ flow measured with the charge exchange spectroscopy. In the radial direction, the cross-correlation function in Fig. 4.7 (b) shows that the fluctuation flow the outside to the inside. The poloidal propagation velocity v_θ is ~ 1.2 km/s with the poloidal mode number m ~ 4. And the radial propagation velocity and wave number are estimated as $v_{\mathrm{r}} \sim 0.4$ km/s. The ratio of the radial and poloidal velocity is $v_{\mathrm{r}}/v_\theta \sim 1/3$. The finite radial phase delay is also found in EHO observed in a Quiescent H-mode plasma in DIII-D, of which turbulence

property is described in the next section (Fig. 4.8).

4.2 High Frequency Turbulence in the presence of MHD instability

4.2.1 Enhancement of Turbulence by EHO

The MEM method is demonstrated by application to spatiotemporal electron density perturbation in a QH-mode plasma in the DIII-D tokamak measured with BES. Measurements of the electron density perturbation are obtained simultaneously at several radii and poloidal locations with a multipoint BES system [60]. BES measures the Doppler shifted D_α fluorescence of the heating neutral beam to investigate localized density fluctuations. The D_α light emission is correlated with the density fluctuation amplitude through atomic physics of the beam excitation process. A 8×8 2D array of high sensitivity BES channels is deployed across the pedestal region from r/a 0.79 to r/a 1.0 as shown in Fig. 4.9 to provide long wavelength density fluctuation measurements. Each channel images an approximately 0.8 cm (radially) by 1.2 cm (poloidally) region near the outboard midplane, and the channel-to-channel separation is 1.0 cm (radially) and 2.7 cm (poloidally). BES provides density fluctuation measurements with a Nyquist frequency of 500 kHz for wavenumbers $k_\perp < 3$ cm^{-1}.

The Fourier cross spectrum between two poloidally separated BES channels ($\Delta Z = 2.7$ cm) are calculated in the QH-mode phase at $\rho \sim 0.91$, where ρ is a normalized minor radius variable, with ρ^2 proportional to the toroidal magnetic flux contained within a flux surface. A time window $\Delta T = 100$ ms is used for the FFT and is averaged over 300 windows with shift steps of $\Delta t = 100$ ms. The resulting spectrum is shown in Fig.4.11 (a). Broadband turbulence was observed in the frequency range up to $\sim$ 150kHz. Coherent peaks in low frequency range in the spectrum are Edge Harmonic Oscillations (EHO), which are observed in QH-mode plas-

mas. Frequency of the fundamental component of the EHO is 6.7 kHz and even-harmonics are dominant in this shot. Figure 4.11 (b) shows poloidal cross phase. A lower frequency band at 5 kHz -50 kHz and a higher frequency band at 50 kHz-150 kHz are found to propagate in opposite poloidal directions (indicated by the opposite sign of the cross phase angle) in the lab frame. The phase of the lower frequency component ($f = 5 - 50$kHz) shows the propagation in the ion diamagnetic drift direction (negative value in the figure), while the broadband higher frequency component in the electron diamagnetic drift direction. As for the EHO frequency components, they seemingly propagate in the electron diamagnetic direction probably, but their poloidal cross phase is nearly zero because the propagation of EHOs are dragged by the oppositly directed large amplitude lower frequency component. The radial profile of the cross spectra between two poloidally separated BES channels for eight different radii are shown in Fig.4.12. The high frequency mode is localized near top of pedestal ($\rho \sim 0.91$), where the amplitude of the EHO peaks. On the other hand, the low frequency mode is overlap the location the high frequency mode exists and increase near the separatrix. In the present paper dispersion relation of the bi-modal turbulence will be examined.

The contour plots of 2D requency-wavenumber spectra obtained by 2D-FFT and MEM in QH-mode are shown in Fig. 4.13 (a) and (b), respectively. The black curves indicate the peak of each contour. 2D-FFT is to decompose the fluctuations into a number of fluctuation modes (poloidal spatial distance x to poloidal wavenumber m and time t to frequency f) [61].

$$Z_{mk} = \frac{1}{MN} \sum_{i=0}^{M-1} \sum_{j=0}^{N-1} z_{ij} \exp\left[2\pi \mathrm{I}\left(\frac{im}{M} - \frac{jk}{N}\right)\right]. \tag{4.1}$$

Figures 4.14 (a) and (b) are comparisons of wavenumber spectra obtained by FFT and MEM for the low frequency mode ($f = 23.4$kHz) and the high frequency mode ($f = 70.3$kHz), respectively. Spectra are normalized with each peak value. As is shown in Fig. 4.14 (a), peak of spectra obtained by MEM shifted to positive wavenumber region (ion diamagnetic direction), which is consistent with the result of cross phase from two poloidally separated channels. For

both frequencies, width of the spectrum with MEM method is narrower than FFT.

In Fig. 4.15, the turbulence velocity for the low frequency mode is shown by black dots, and the turbulence velocity of the high frequency mode is shown by red dots. The turbulence velocity was calculated with the peak valued at $f = 23.4$kHz for the low frequency mode and the $f = 70.3$kHz for the high frequency mode. The radial electric field is obtained from the radial force balance equation for the measured carbon impurity density and temperature with the Charge Exchange Spectroscopy (CXS) [62]. $E \times B$ velocity is shown by squares in Fig. 4.15. Positive value in the velocity indicates that fluctuations are propagating in the electron diamagnetic direction in the lab frame and a negative value represents propagation in the ion diamagnetic direction. It is found that velocity of the high frequency band well matches with the $E \times B$ velocity just inside the well-like structure while the low frequency band is propagating in the ion diamagnetic direction in the plasma frame.

Figure 4.16 shows the radial profile of the turbulence amplitude, comparing for 4 time slices which is shown in the spectrogram in Fig. 4.10. For entire mesuring region, the turbulence amplitude in the frequency range of 60-150 kHz tends to be higher in the time of occurence of EHO. The radial profiles of electron density and electron temperature are shown in Fig. 4.17. Density at the top of the pedestal decreseas when EHO appears, while density gradient at the edge keeps constant. The change in electron temperature profile is similar to the density profile, with small reduction at the pedestal top, but within error bars. In the frequency range of 60-150 kHz, which is used as frequency filterling range to obtain amplitude profile shown in Fig. 4.16, two different turbulence components coexist. Low frequency band turbulence propagetes ion diamagnetic direction in Lab frame as mentioned above, and localized the edge region as is shown in Fig. 4.12. In the edge region, the low frequency band turbulence account for the most of the portion of fluctuation amplitude in the frequency range of $f = 60 - 150$. Near the top of the pedestal ($\rho = 0.91$), the high frequency band turbulence is most dominat in the fluctuation amplitude in the frequency range of $f = 60 - 150$ kHz because the low frequency band is

below the frequency range (4.13 (b)) and is filtered out. From the plasma edge to the top of the pedestal, the density gradient is fairly the same between the duration with EHO and ELMy phase. To investigate cause of the turbulence amplitude change, nonlinear coupling among different frequency component will be examined in next section.

4.2.2 Coupling Between EHO and Turbulence

The squred bicoherence was calculated to investigate nonlinear coupling in a plasma with EHO. The results for three locations $\rho = 0.88, \rho = 0.91, \rho = 0.94$ are shown in Fig. 4.18. The time window of 1024 μs was ensemble averaged over 300 windows in 4020 – 4327.2ms. Assuming that turbulence property is the same along field lines, cross bicoherence of two poloidally adjacent channels at each radial location are taken for noise reduction. Clear bicoherence values are found at where the sum of the frequencies f_1 and f_2 matches any of the EHO frequencies. In addition, at near the pedestal top ($\rho = 0.91$) small but finite bicoherence values are also found along $f_1 = 13.2$ kHz (the second harmonic frequency) in the frequency range of turbulence component ($f_2 = 60 - 150$ kHz), indicating the amplitude of the turbulence component fluctuation is modulated at the frequency of EHO second harmonics.

There are two probable reason for the turbulence amplitude modulation in the density fluctuation signal of BES. First possible cause is the flux surface displacement. In the plasma now focuced on, the turbulence amplitude has the gradient in the radial direction from the inside to the edge as shown in Fig. 4.16. Assuming that the turbulence amplitude is a function of the flux surface, BES will detect higer amplitude of the turbulence when the flux surface shifts towered the inside from the initial location as BES measuring position is fixed in a physical space. On the contrary, BES will detect lower amplitude of the turbulence when the flux surface shifts toward the outside from the initial location. Oscillating flux surface at a certain frequency would result in a turbulence amplitude modulation at the frequency in the BES signal as is shown in Fig. 4.19. Second probable cause is nonlinear interaction between the turbulence and the EHO.

To investigate the cause of the finite bicoherence value between turublence and EHO, we will study the behaviour of the turbulence amplitude by using the envelope analysis. The wave form of turbulence envelope and flux surface oscillation will be compared. Turbulence envelope is taken by using hilbelt transform of the BES signal filtered for the frequency range of the turbulence (Fig. 4.20). Electron temperature fluctuation is taken as the wave form of the flux surface oscillation. The phase and amplitude of ecectron temperature fluctuation detected by electron cyclotron emission (ECE) radiometer can be regarded as the phase and amplitude of flux surface oscillation, because of the high conductivity of electron along field lines. Figure 4.22 shows spectra of the turbulence envelope and the electron temperature fluctuation. The both spectra shows coherent peak at the frequency of EHO. Figure 4.23 is the comparison of the wave form of the both the turbulence envelope and the electron temperature fluctuation, which is filterd for the EHO frequency range (indicated dashed lines in Fig. 4.22). The results showed the wave form of turbulence envelope was not exactly same phase as the flux surface of the EHO frequency component.

The flux surface displacement can be estimated with the change in electron temperature and the temperature gradient. The ECE diagnostic on DIII-D is a multichannel heterodyne radiometer that provides Te(r,t) from measurements of optically thick, second harmonic extraordinary mode (X-mode) electron cyclotron emission [64]. The ECE system has 40 channels, viewing the DIII-D plasma along a horizontal chord at the tokamak midplane at a toroidal angle of 81 degrees. The ECE data is sampled with both slow (1-2 kHz) and fast (100-500 kHz) digitizers. In the QH-mode discharge (#163467), the plasma is optically thick at $\rho \sim 0.88$, with optical thickness $\tau \sim 14.3$ (see appendix). At $\rho = 0.88$ the tempareture gradient is $\nabla T_e = -1.94$ keV/m (radial profile of ∇T_e is shown in Fig. 4.24. The amplitude of ECE signal at the frequency of EHO ($f \sim 13$ kHz) is 8.03 keV. From these values, the flux surface displacement is estimated as $d \approx 0.42$ cm. With the magnitude of the flux surface displacement, the ratio of turbulence envelope amplitude to the mean value is estimated as 0.3%. However, in the measured BES

signal the ratio is around 14%. The change in turbulence amplitude is much larger that the expected amplitude change associated with flux surface displacement. This is an evidence that the turbulence amplitude modulation effect is not fully caused by the flux surface oscillation, and that other effect or nonlinear effect involvs. Figure 4.21 shows the temporal evolution of turublence envelope in ELMy H-mode phase. The averaged level of envelope is 0.0405, while the level in QH-mode phase (Fig. 4.20) is 0.0481, indicating mean time turbulence increase in the presence of EHO.

For the low frequency band component which propagates in the ion diamignetic direction, amplitude modulation effect by EHO is not significant. Figure 4.26 shows auto power spectrum of the envelope of beam emission in the frequency of 30-38 kHz (low frequency band turublence propagation in the ion diamagnetic direction). The spectrum of low frequency band envelope shows no significant coherent peak. The amplitude of low frequency band peaks near the separatrix while the high frequency band turbulence and EHO peaks near the pedestal top. Turublence amplitude modulation effect by EHO is strong on the high frequency band presumably due to overlapped localization of the two modes.

The difference between the waveforms of turbulence envelope and flux surface oscillation is clear when EHO amplitude is large and QH-mode phase is sustained for long duration (Fig. 4.27). In this shot, BES measured density fluctuation from pedestal top to a few centimeters outside the separatrix (Fig. 4.28. In the frequecy range of 150-200 kHz, bicoherence value was found be finite with EHO fundamental frequency in beam emission measured at near the pedestal top. The ECE signal shows un unbiguous peak at the EHO fundamental frequency in the spectrum (Fig. 4.30), indicating that the flux surface displacement is large in the radial direction. The waveform of the ECE signal at the frequency of EHO fundamental, showing gradually increasing amplitude and constant phase in time as shown in Fig. 4.31.

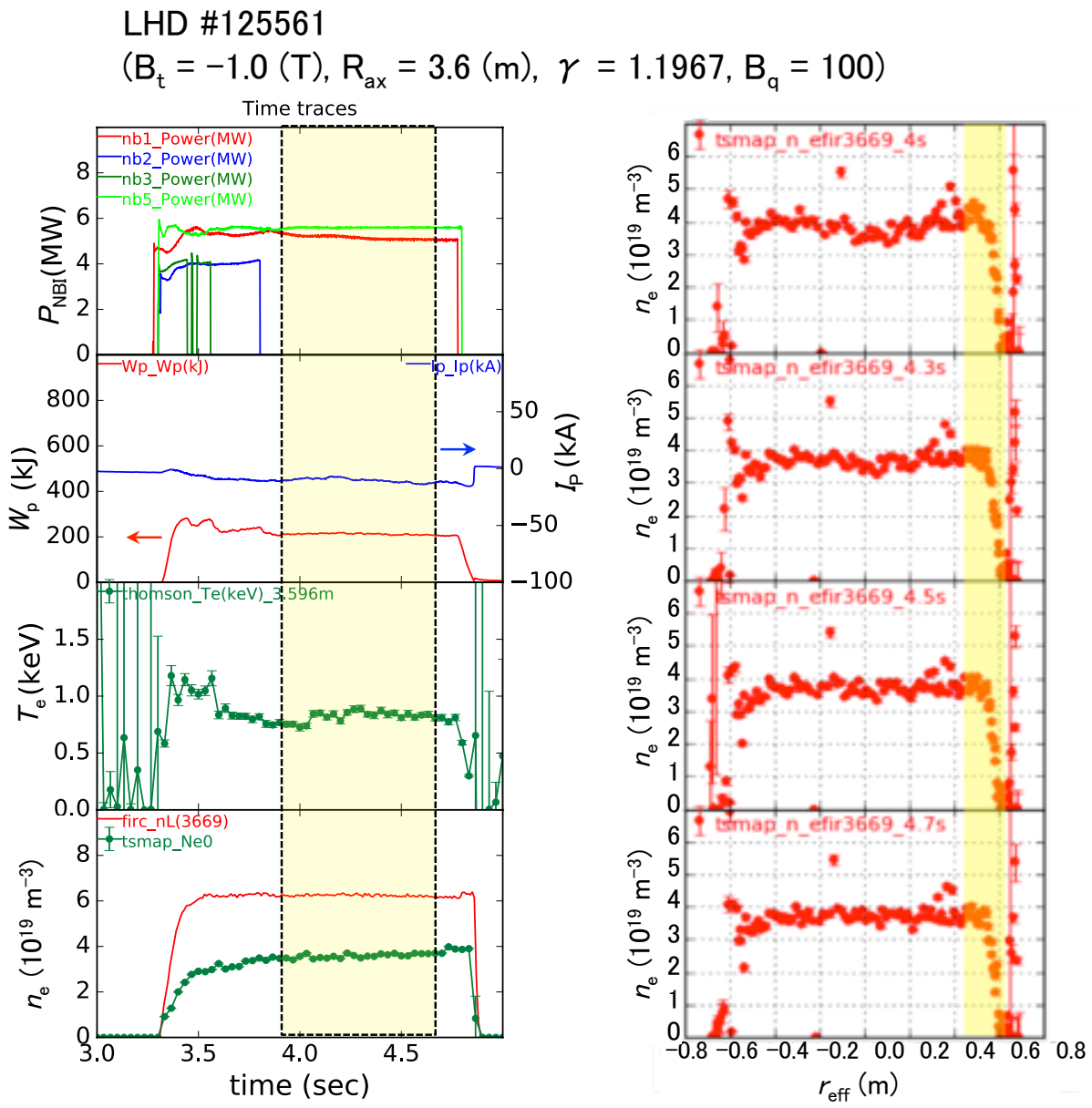

Figure 4.1: A typical temporal evolution of plasma parameters for a discharge in which low-frequency fluctuations appear (#125561):

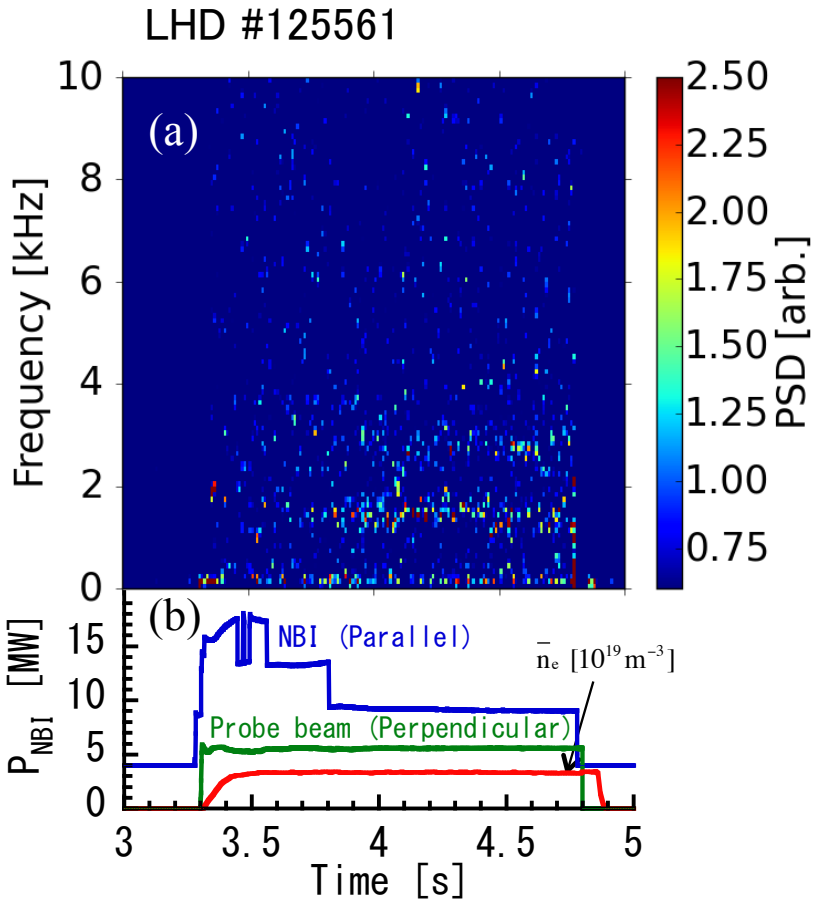

Figure 4.2: Temporal evolution of (a) auto power spectrum and (b) power of neutral heating beams.

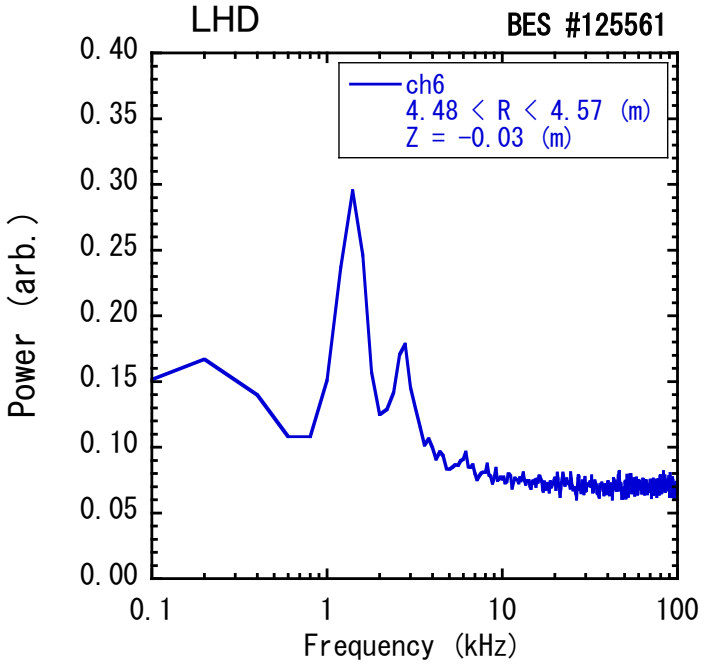

Figure 4.3: The mean frequency spectrum of the density fluctuation for $3.9s < t < 4.8s$.

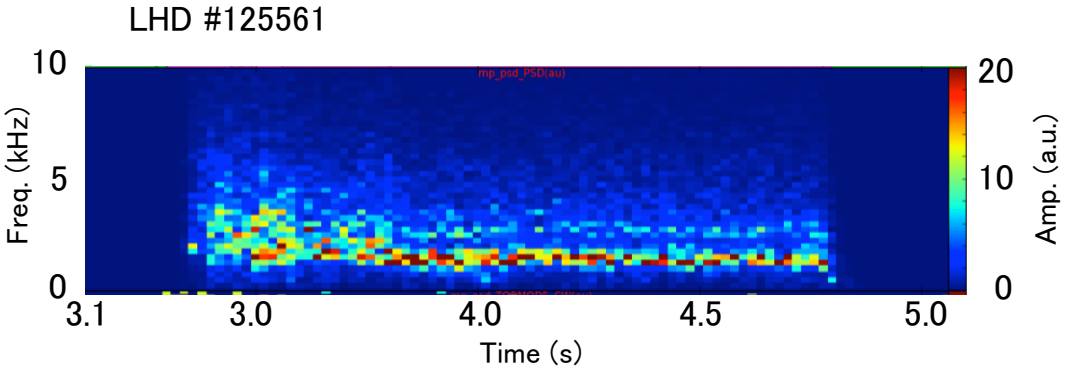

Figure 4.4: Temporal evolution of the magnetic fluctuation.

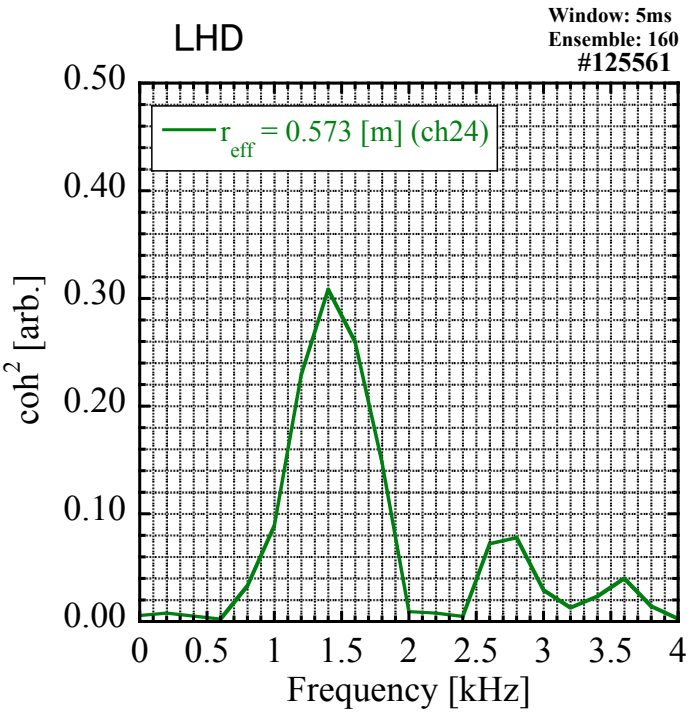

Figure 4.5: Squared coherence between the density and magnetic fluctuations in $3.909s < t < 4.709s$ at $r_{\mathrm{eff}} = 0.573$m.

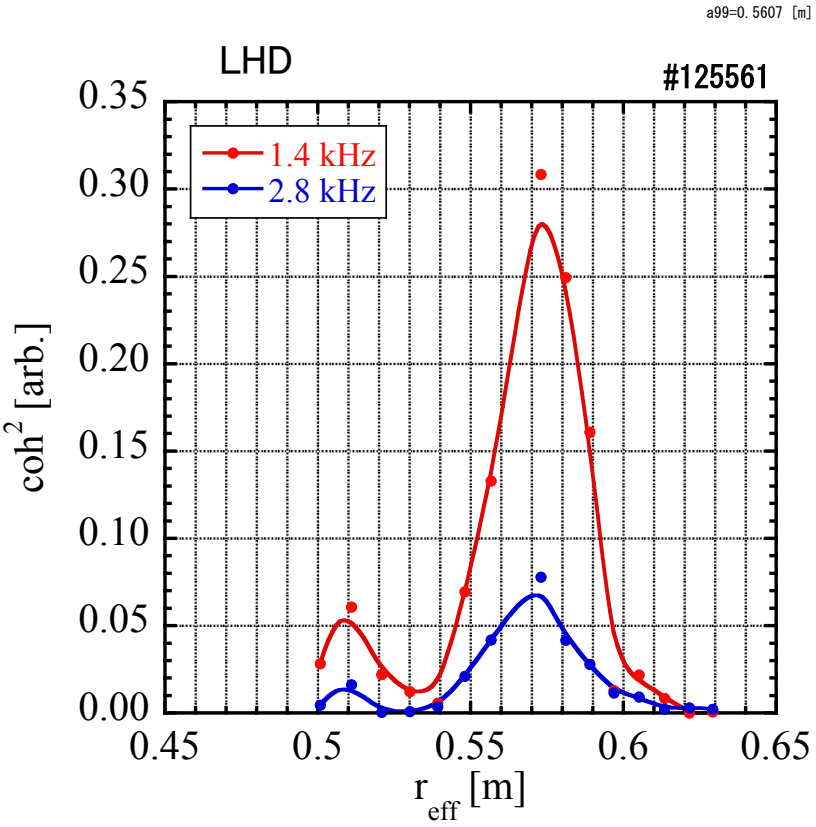

Figure 4.6: The radial profiles of the squared coherence between the density fluctuation and the magnetic fluctuation of 1.4 kHz (red) and 2.8 kHz (blue). The value of coherence peaks at near $r_{\mathrm{eff}} = a_{99} = 0.561$, where a_{99} means the effective minor radius inside which 99% of the electron kinetic energy exists.

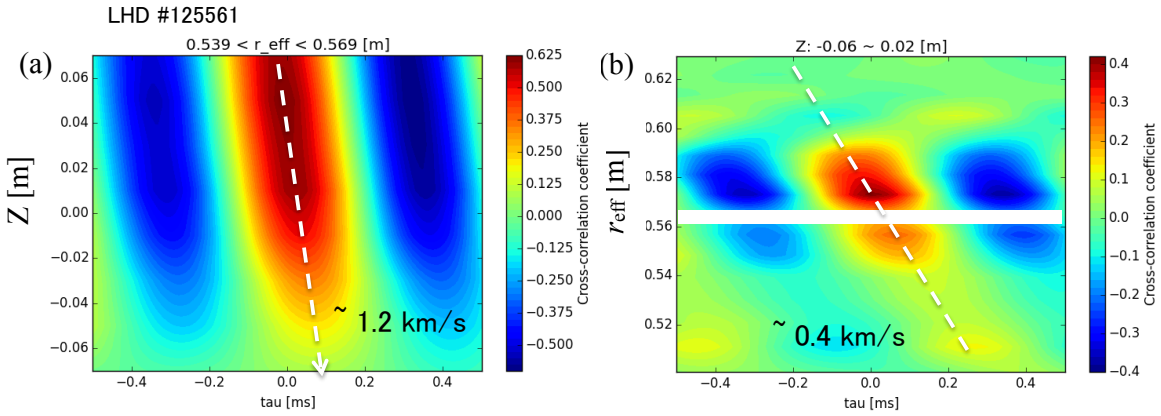

Figure 4.7: Contour plot of the cross-correlation function of the fundamental frequency component ($1.1 < f < 1.8$kHz) of the density fluctuation in (a) poloidal direction and (b) radial direction.

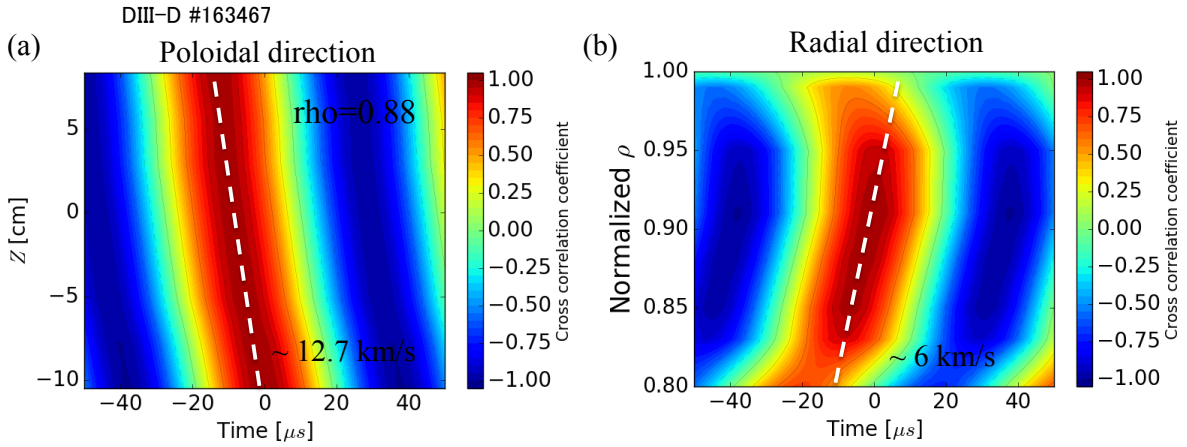

Figure 4.8: Contour plot of cross correlation function of EHO observed in a QH-mode plasma for (a) poloidal direction and (b) radial direction.

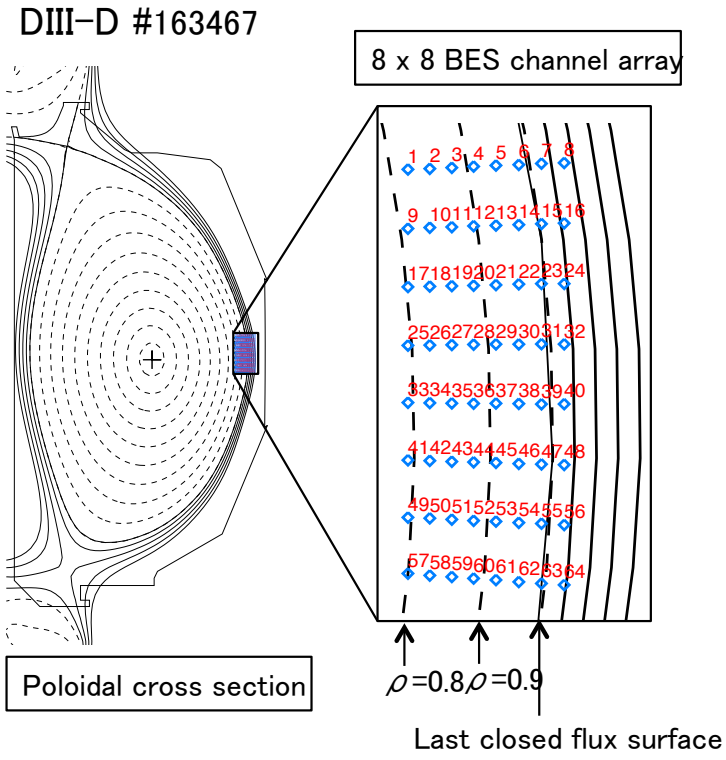

Figure 4.9: BES measuring locations overlaid on the flux surface.

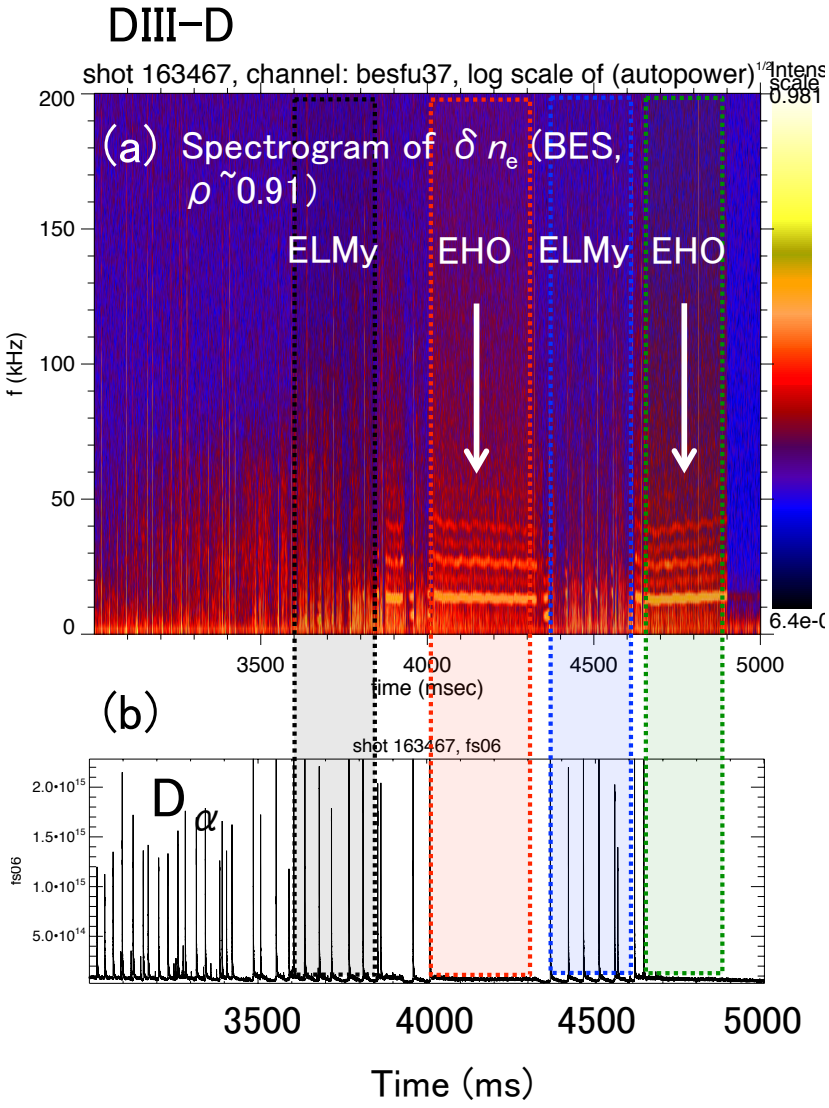

Figure 4.10: Temporal evolution of (a) auto power spectrum of density fluctuation and (b) D_α signal.

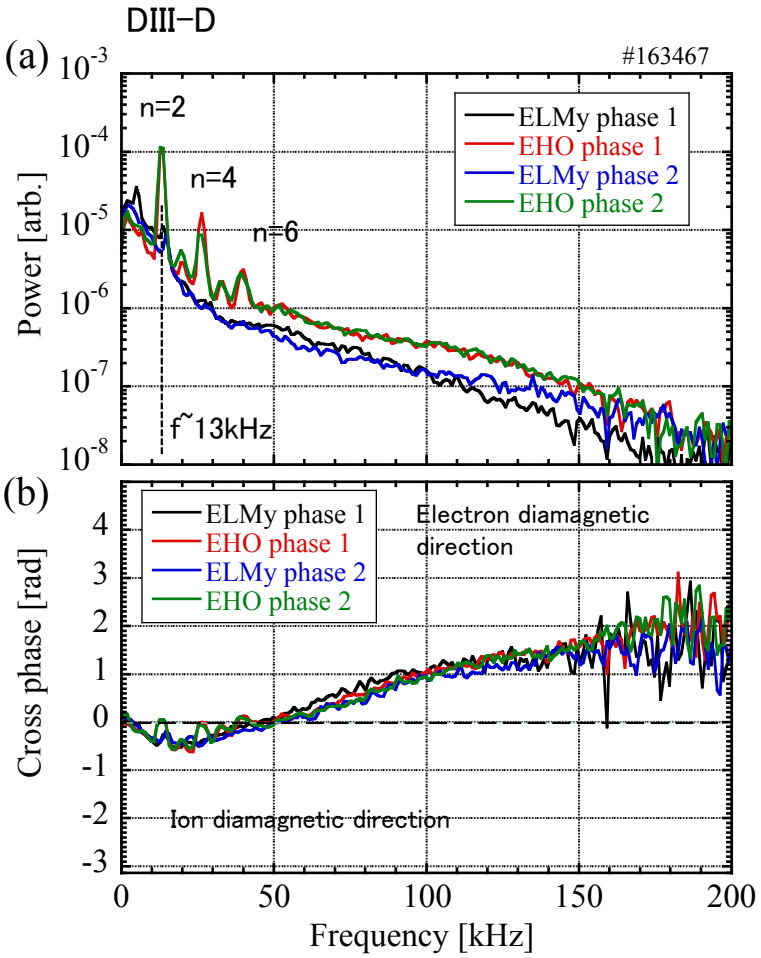

Figure 4.11: Poloidal cross spectrum (upper panel) and cross phase (ΔZ = 2.7 cm) (lower panel) of density fluctuations from BES measurements for ρ ~0.91. The positive cross phase indicates turbulence propagating in the ion diamagnetic direction in the lab frame and the negative cross phase indicates turbulence propagating in the electron diamagnetic direction.

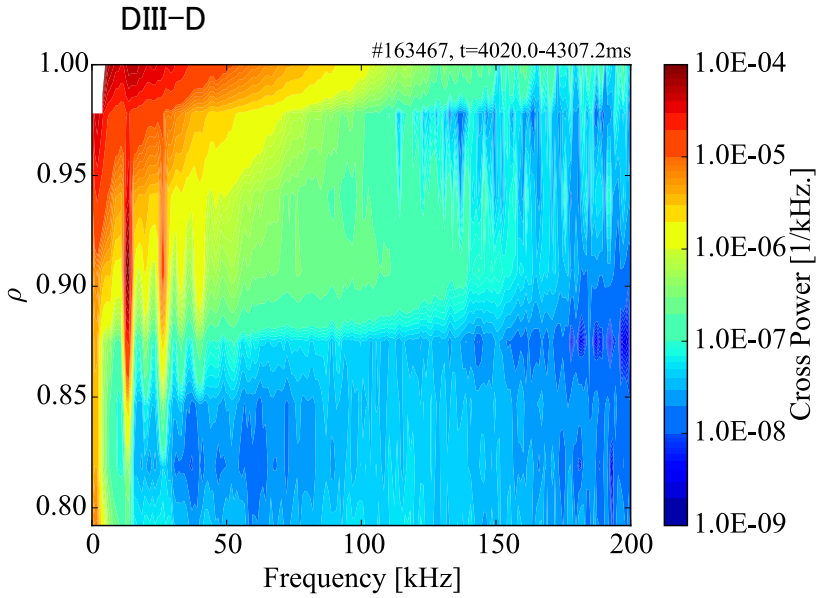

Figure 4.12: The radial profile of the mean frequency cross power spectrum.

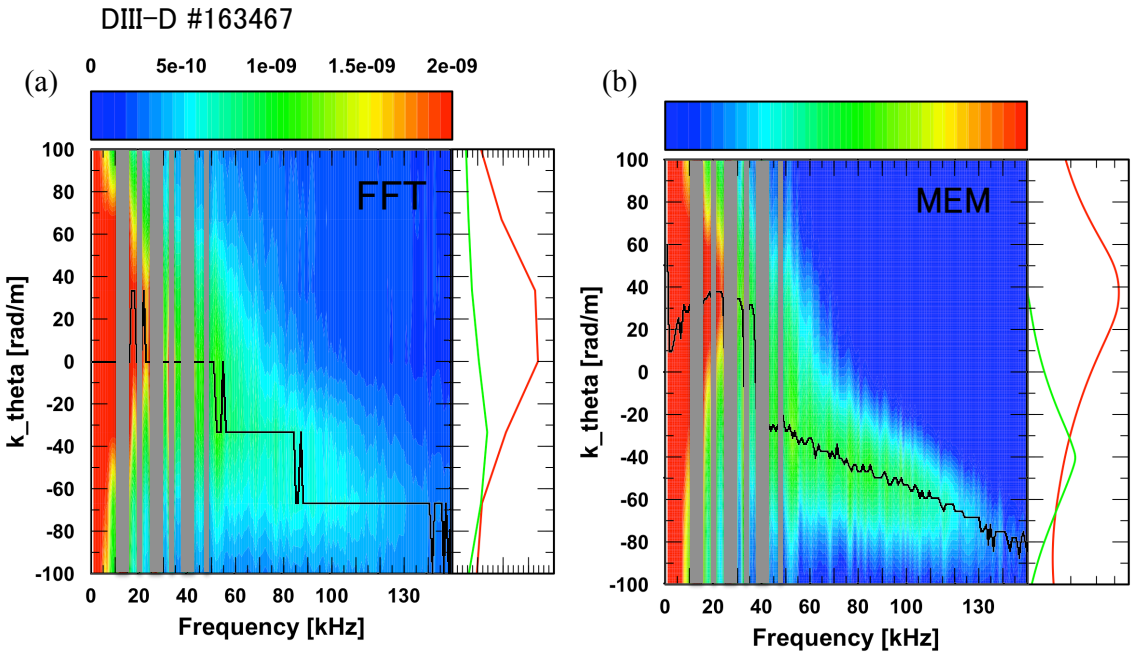

Figure 4.13: Dispersion relation of density fluctuation calculated by applying (a) 2-D FFT and (b) MEM to time series data of 8 poloidal BES channels (ΔZ = 2.7cm). The solid line indicates the peak of the contour.

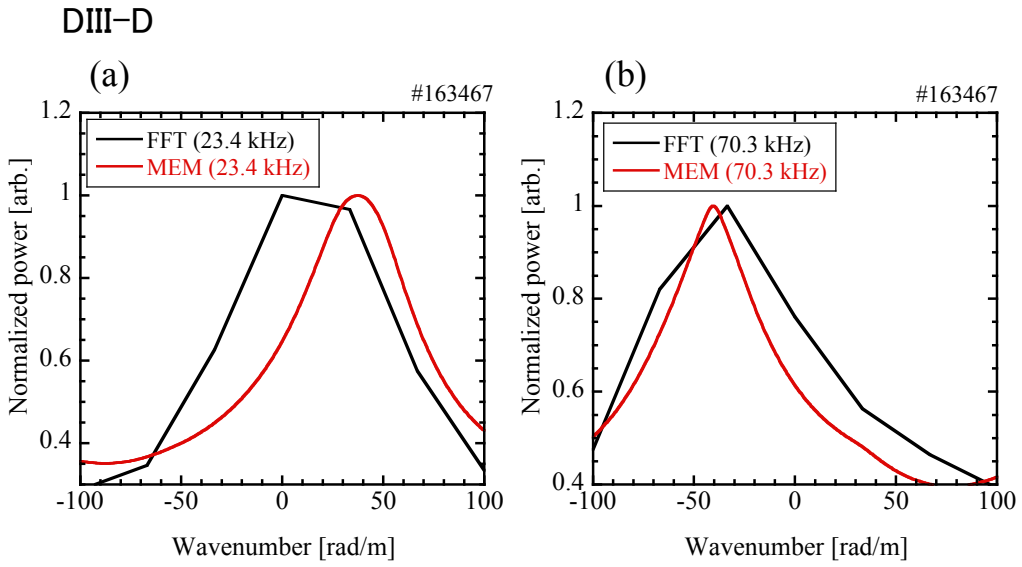

Figure 4.14: Comparison of wavenumber spectra obtained by FFT (black) and MEM (red). Spectra are scaled at the at the strength of each peak.

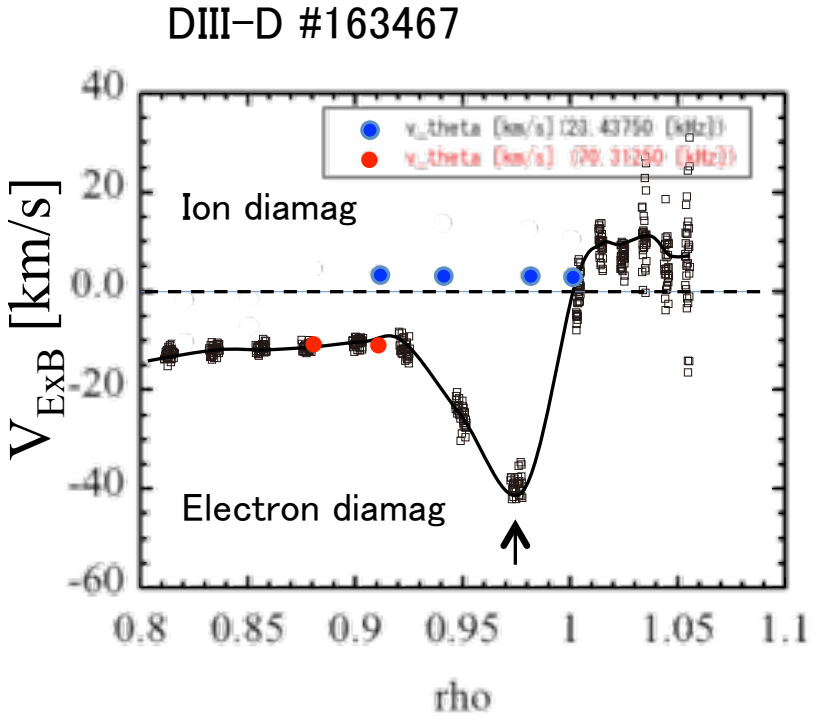

Figure 4.15: Turbulent group velocity from BES measurements for lower frequency at 23.4 kHz (blue), higher frequency at 70.3 kHz (red), and $E \times B$ velocity (square) from (Charge Exchange Spectroscopy) CXS measurements. Solid curve line is an eyeguide for CXS data.

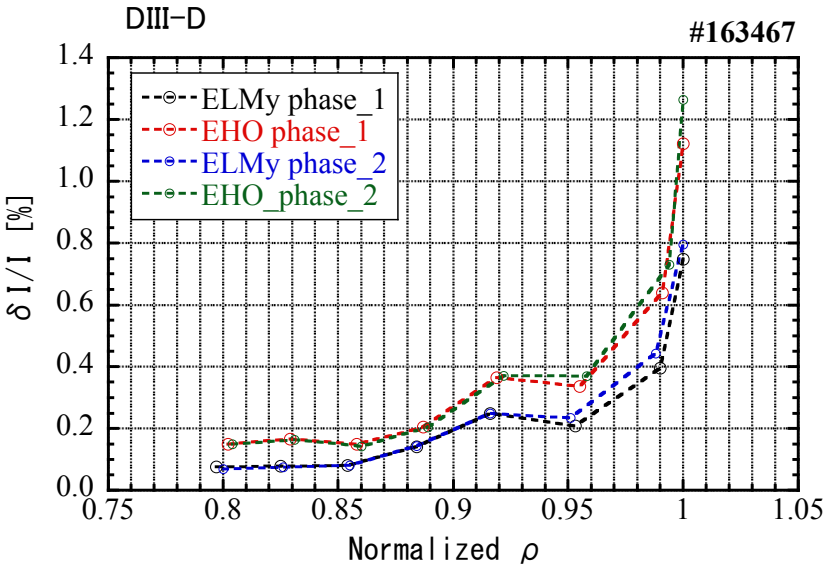

Figure 4.16: Turbulence amplitude profile.

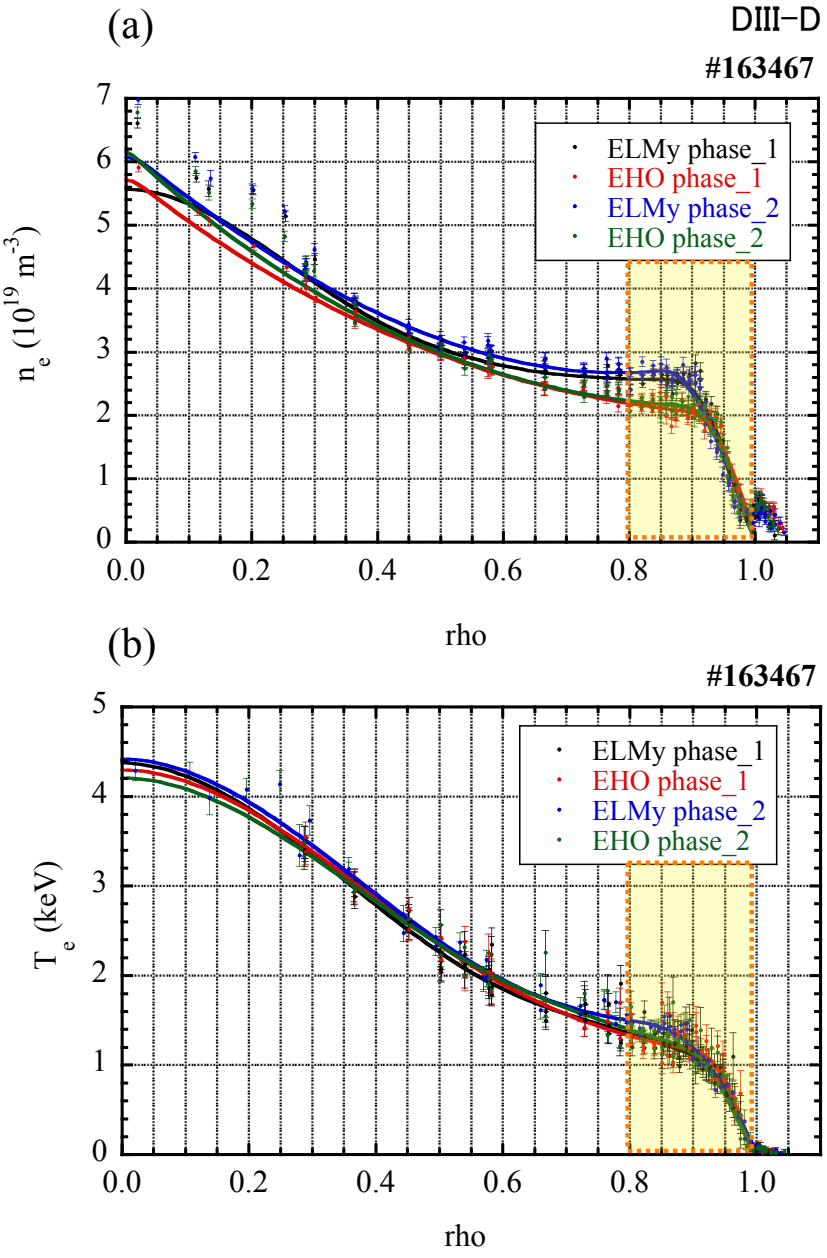

Figure 4.17: Radial profile of (a) electron density and (b) electron temperature for four time slices indicated in Fig. 4.10. The BES measurement region is indicated with yellow shade.

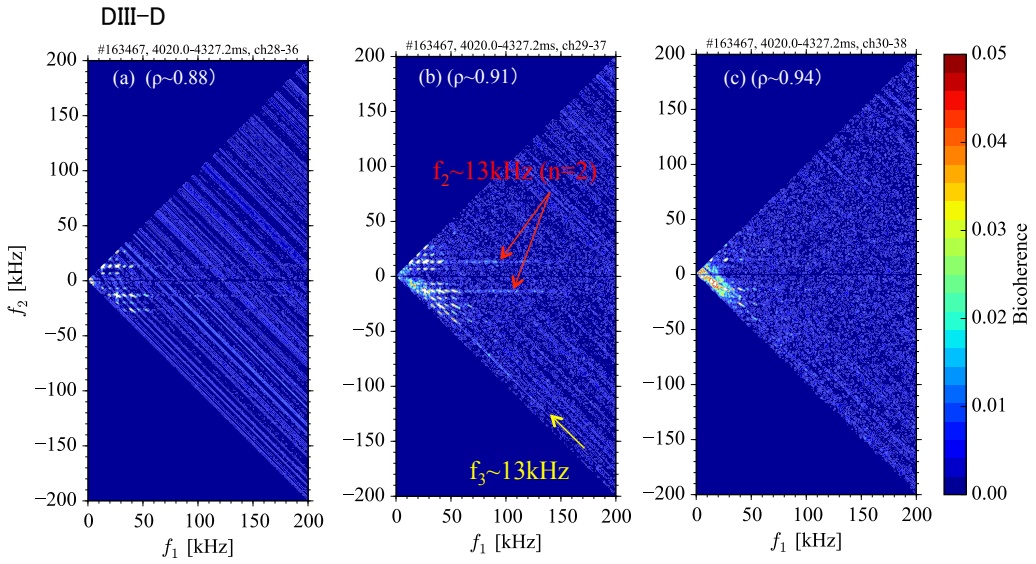

Figure 4.18: Time averaged squared cross bicoherence in beam emission signal when EHO exists. (a) $\rho = 0.88$, (b) $\rho = 0.91$, (c) $\rho = 0.94$.

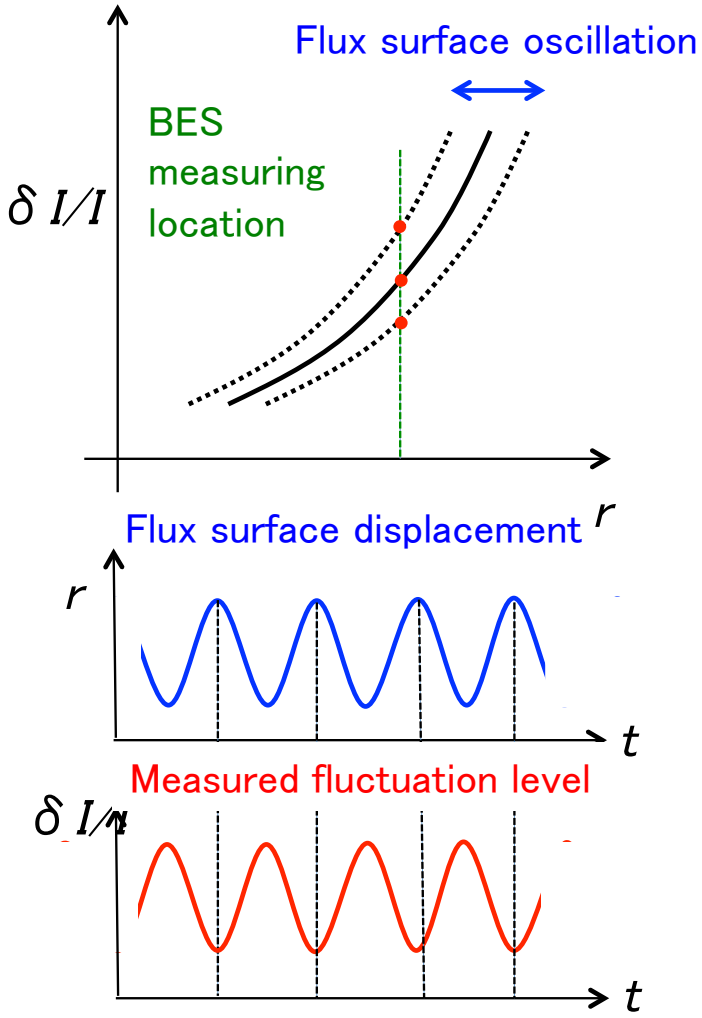

Figure 4.19: A schetch illustrating the detected fluctuation level change in the case that fluctuation is a function of flux surface. The amplitude profile is oscilating in the radial direction. Because BES measuring position is fixed in phyisical space, the fluctuation level is change in time at the frequency of flux surface oscillation. When the fluctuation level has a outword gradient, the flux surface oscillation and measured fluctuation level are out of phase.

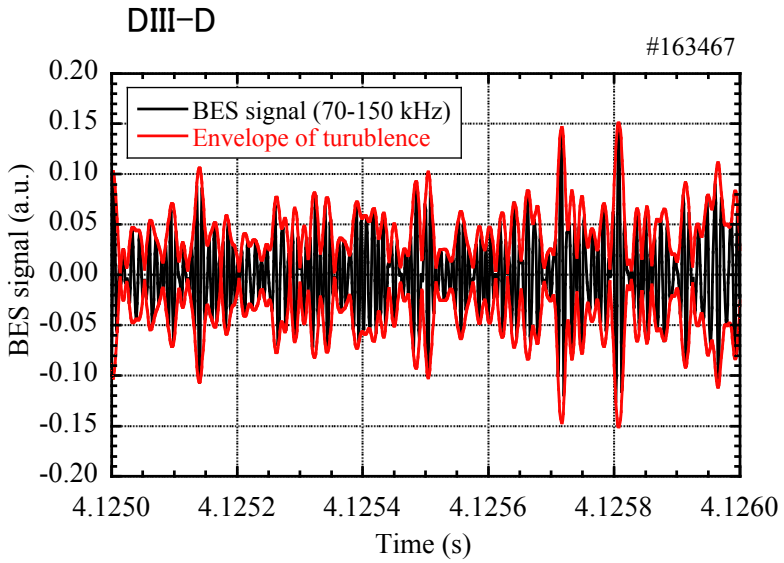

Figure 4.20: Temporal evolution of turbulence component in density fluctuation measured in QH-mode phase at $\rho = 0.91$ ($70 < f < 150$kHz) and its envelope.

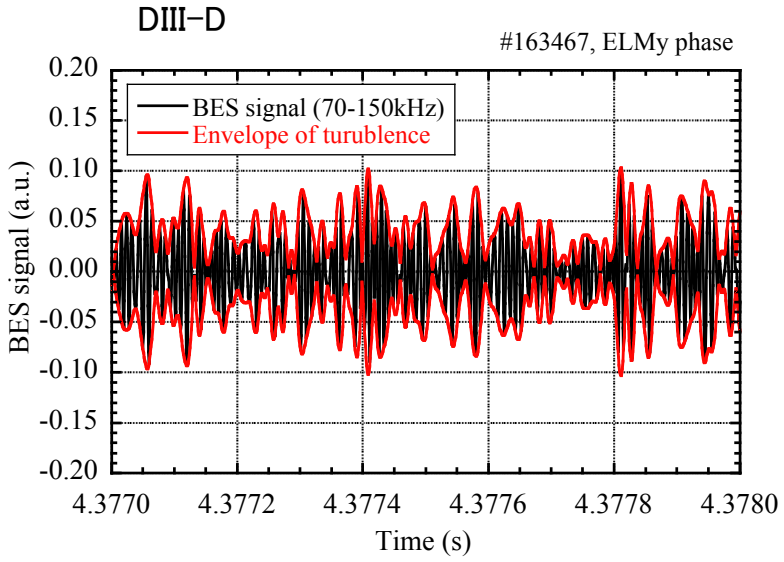

Figure 4.21: Temporal evolution of (black) turbulence component in density fluctuation measured in ELMy H-mode phase at $\rho = 0.91$ ($70 < f < 150$kHz) and (red) its envelope.

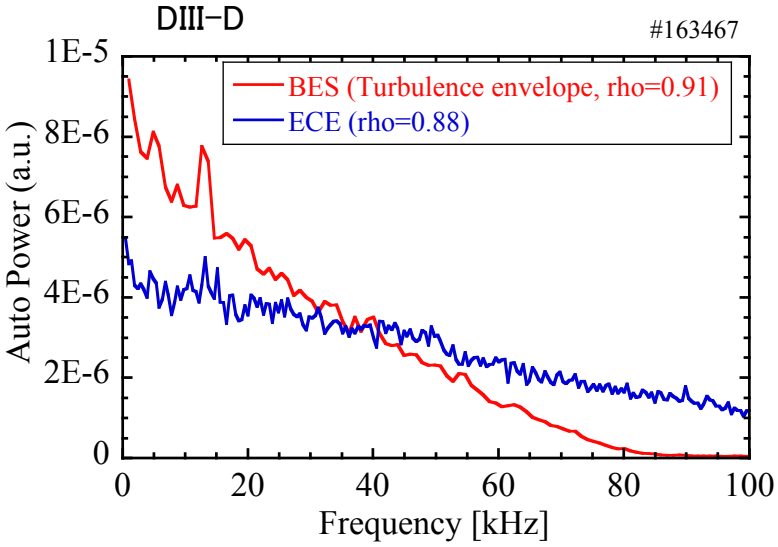

Figure 4.22: Mean frequency spectra of (red) the envelope of density fluctuation (higher frequency component in BES signal) and (blue) temperature fluctuaion (ECE).

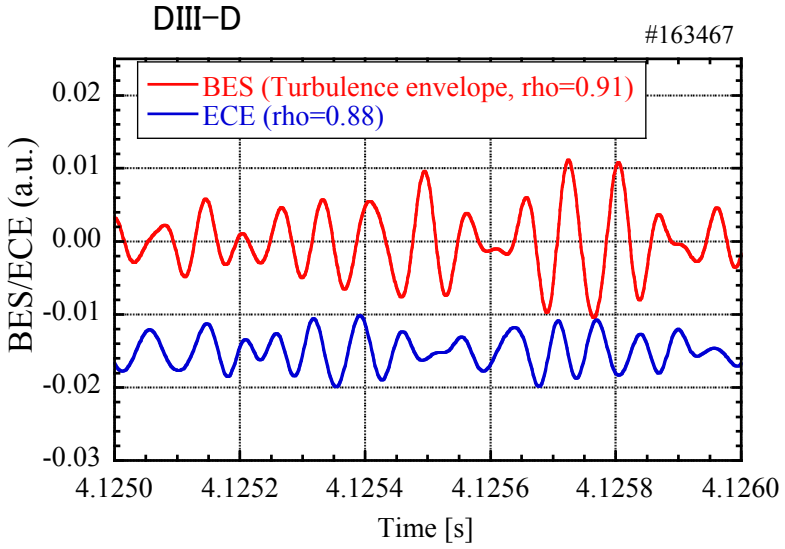

Figure 4.23: Time evolution of turbulence component in the density fluctuation. A red curve shows an envelope of the signal.

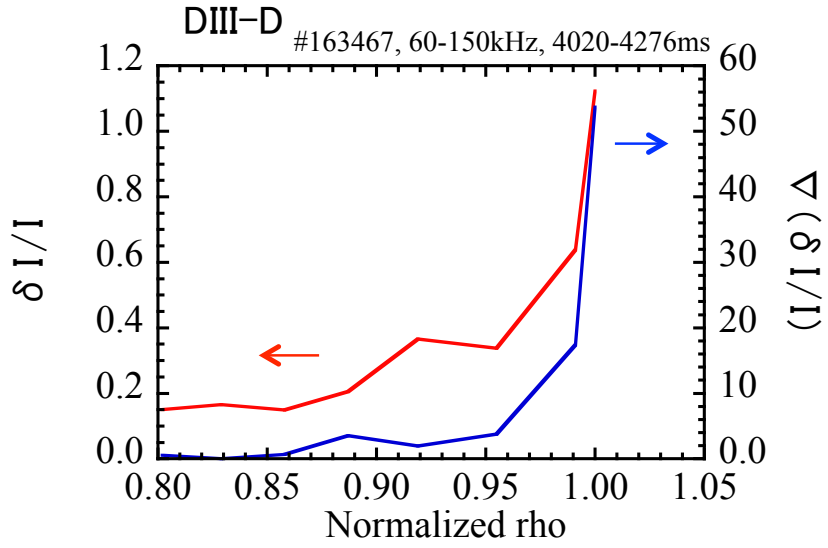

Figure 4.24: Radial profile of electron temperature T_e and gradient ∇T_e for t = 4171 ms (QH phase).

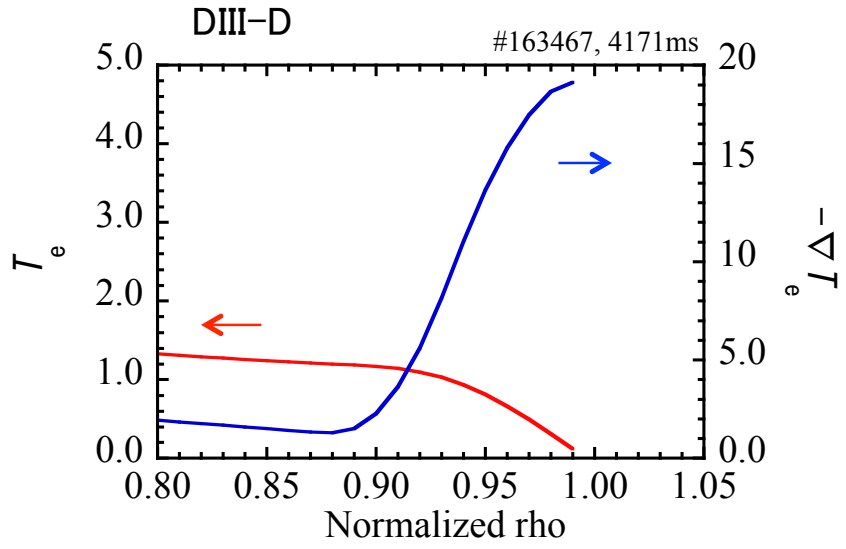

Figure 4.25: Radial profile of fluctuation level in beam emission ($\tilde{I}/I$) in the frequency range of 60-150 kHz and its gradient ($\nabla(\tilde{I}/I)$) for t =4020-4276ms (QH-phase).

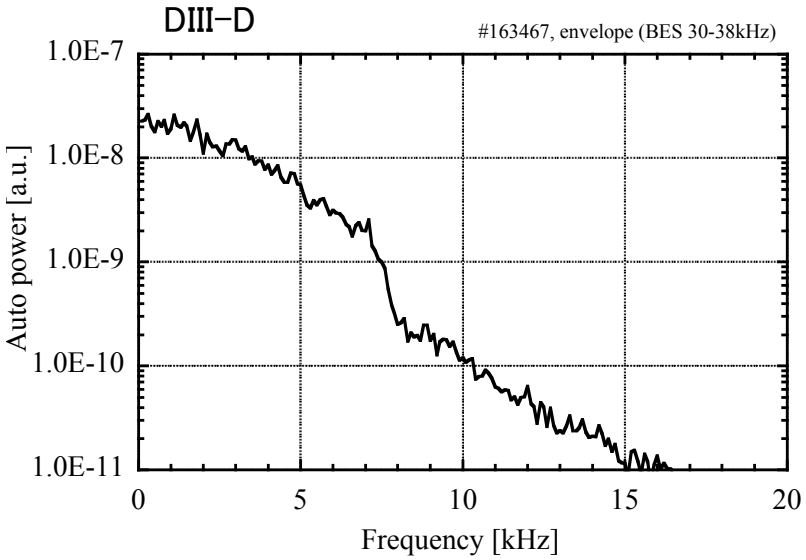

Figure 4.26: Auto power spectrum of envelope of beam emission for the low frequency band (30-38 kHz) measured at $\rho = 0.95$.

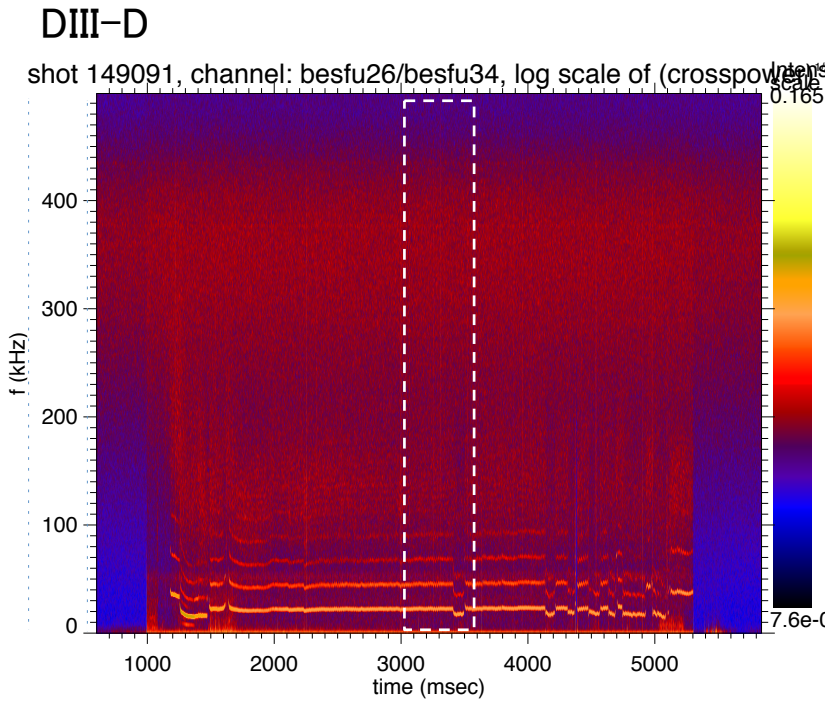

Figure 4.27: Temporal evolution of auto power spectrum of beam emission measured in a QH-mode plasma (#149091). EHO appears in most of the time of discharge with almost constant frequencies in time.

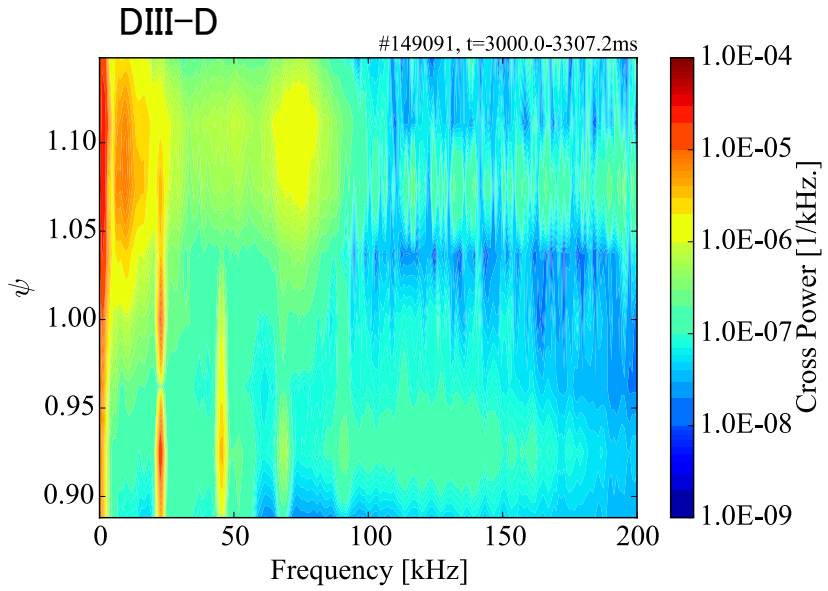

Figure 4.28: Radial profile of mean frequency spectrum for a shot 149091.

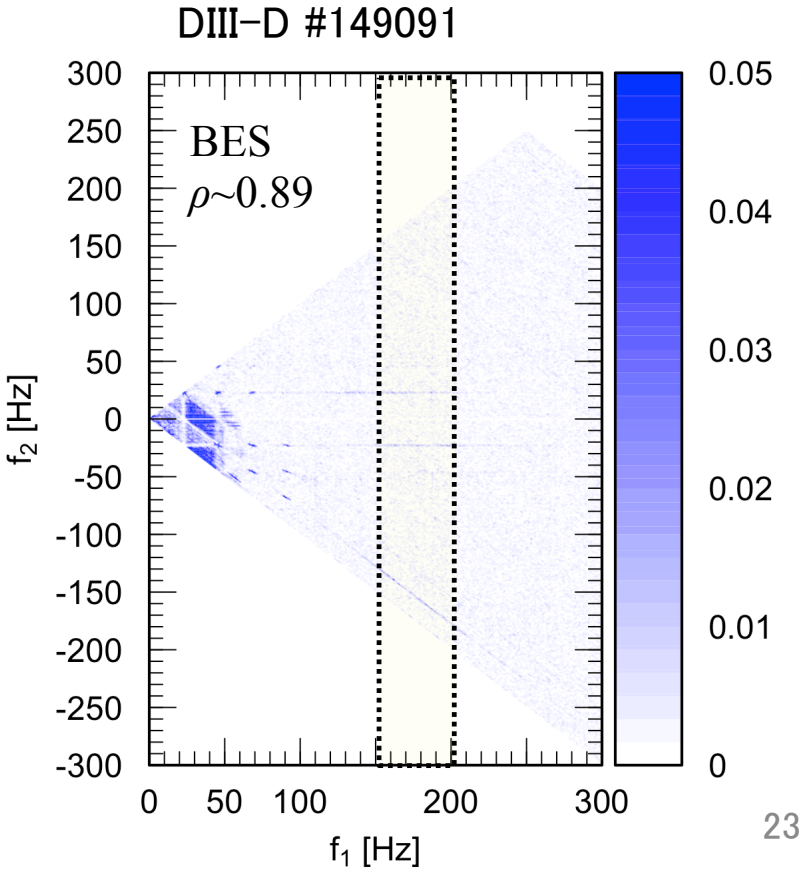

Figure 4.29: Time averaged squared cross bicoherence in beam emission signal in QH-mode discharge. The fundamental frequency of EHO is $f \sim 23$ kHz in this shot.

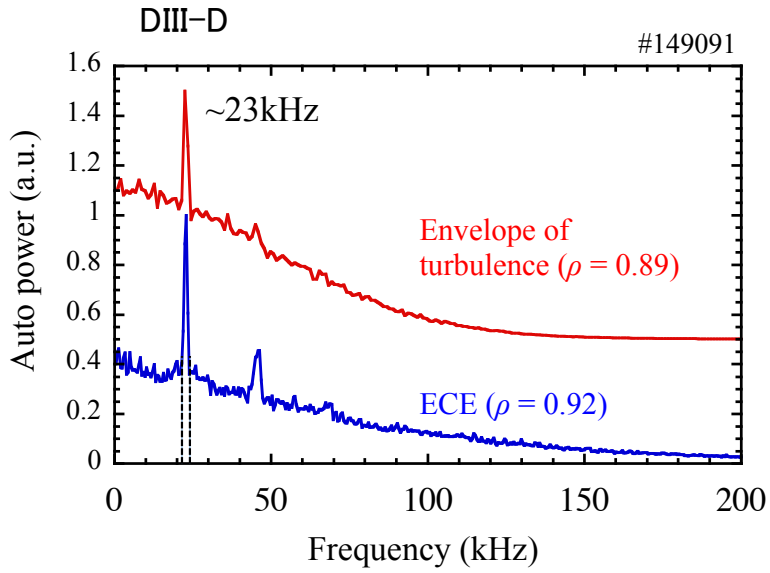

Figure 4.30: Mean frequency spectra of the envelope of the turbulence component in density flucuation (red) and temperature fluctuaion measured with ECE (blue) for the shot 149091.

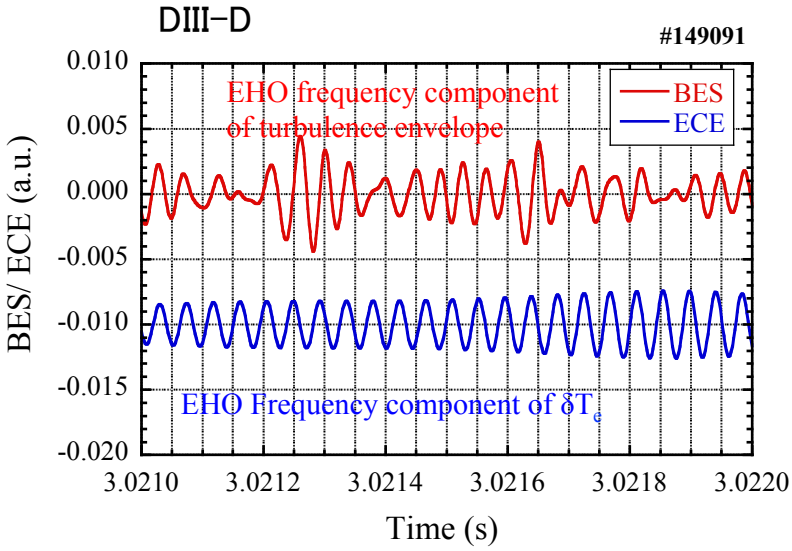

Figure 4.31: Comparison of time evolution of turbulence frequency component (f = 150 – 200 kHz) in the beam emission and ECE signal. Both signals are frequency filtered for the EHO fundamental frequency.

4.3 Conclusions

The subject of this thesis is to understand the coupling between MHD instability and turbulence in toroidal plasmas Here, summary for each chapter is given.

In order to study on plasma fluctuations, it is necessary to investigate the characteristics of fluctuations based on the precise measurements. In chapter 2, we highlighted an advantage of BES of local measurement. BES has been developped in LHD as well as other torus confinement devices. To achieve capability to measure the structure of fluctuations in two direction at the same time improved signal-to-noise ratio, we deployed the fiber bundle configuration. The images of the fiber bundles takes slit shape, then the system has increased wavenumber sensitivity in a paticular direction compared to sampling image of square or round shape.

In chapter 3, data analysis mothod were shown. In addition to usage of FFT as a basic tool for spectral analysis, we used MEM to get wavenumber spectrum. This bennefits in the case of spectral analysis with very short data series. Bicoherence is an index of degree of three wave interaction. Hilbert transforn is a method to take an envelope from fluctuating data. After seeking the frequency range where turbulence amplitude modulation by bicoherence, detailed analysis on phase and amplitude of turbulence envelope with regard to the flux surface was done in later chapter.

In chapter 4, characteristics of density fluctuation caused by EHO and turbulence were discussed. EHO, which is the low frequency fluctuations with several harmonics was observed by BES in LHD. The density fluctuation was found to have coherency with magnetic fluctuation, and had its peaks near the last closed flux surface. Spatiotemporal structure of density fluctuation caused by EHO showed poloidal propagation in the electron diamagnetic direction and finite radial phase delay, which was seen that outer sied leads the inner side. If we regard the radial phase delay as a propagation, the ratio of phase velocity was $v_{\mathrm{r}}v_{\theta} \sim 1/3$. Similar finite radial phase delay of density fluctuation by EHO was observed also in DIII-D. Amplitude modulation effect of EHO frequency on turbulence was observed in QH-mode plasma on DIII-D.

The phase between turbulence envelope and flux surface was compared with electron temperature fluctuation signal as a reference. The results showed the wave form of turbulence envelope was not exactly same phase as the flux surface of the EHO frequency component. This is an evidence that the turbulence amplitude modulation effect is not fully caused by the flux surface oscillation, and that other effect or nonlinear effect involvs.

Publications

Refereed papers

- “Beam emission spectroscopy with radially and poloidally elongated optical sightlines”, M. Ono *et al.*, *Rev. Sci. Instrum.* 87, 11E559 (2016)
- “Measurement of Spatiotemporal Structures of Density Fluctuations Using Two-Directional Beam Emission Spectroscopy in LHD”, M. Ono *et al.*, *Plasma Fusion Res.* 11, 1402115 (2016)

References

[1] K. Ida, *et al.*, *Sci. Rep.* **5**, 16165 (2015)

[2] S. Inagaki *et al.*, *Phys. Rev. Lett.* **107**, 115001 (2011)

[3] K. Itho *et al.*, *Journal Phys. Soc. Japan* **85**, 094504 (2016)

[4] J. D. Callen *Phys. Rev. Lett.* vol. 39, 24, 1540(1990)

[5] K.H. Burrell, *Phys. Plasmas* **8**, 2153(2001)

[6] C.M. Greenfield, *Phys. Rev. Lett.* **86**, 4544(2001)

[7] B.A. Grierson, *Phys. Plasmas* **22**, 05901(2016)

[8] W. Suttrop *Plasma Phys. Control. Fusion* **45**, 1399 (2003)

[9] W. Suttrop *Nucl. Fusion* **45**, 721 (2005)

[10] Y. Sakamoto *Plasma Phys. Control. Fusion* **46**, A299 (2004)

[11] N. Oyama *Nucl. Fusion* **45**, 871 (2005)

[12] P.B. Snyder, *Phys. Plasmas* **9**, 2037 (2002)

[13] P.B. Snyder, *Nucl. Fusion* **44**, 320 (2004)

[14] K.H. Burrell, *Phys. Plasmas* **12**, 056121 (2005)

[15] A. Iiyoshi, *et al.*, *Nucl. Fusion* **39**, 1245 (1999)

[16] A. Komori, *et al.*, *Fusion Sci. Technol.* **58**, 1 (2010)

[17] A. Sagara *et al.*, *Nucl. Fusion* **45** No4, 258 (2005)

[18] O. Ohyabu, T. Watanabe, H. Ji *et al.*, *Nucl. Fusion* **34**, 387 (1994)

[19] O. Motojima *et al.*, *Nucl. Fusion* **43**, 1674 (2003)

[20] O. Motojima *et al.*, *Fusion Sci. Technol.* **46**, 1 (2004)

[21] M.W. Maisel, T. Ohkawa, K.H. Burrell, R.L. Freeman, F.J. Helton, T.H. Jensen, R.J. Lahaye, D.O. Overskei, R. Prater, J.M. Rawls, and T. Tamano, *Nucl. Fusion* **25**, 1113 (1985)

[22] J.L. Luxon, *Nucl. Fusion.* **42**, 614 (2002)

[23] J. Wesson, *Tokamaks.* OXFORD SCIENCE PUBLICATIONS (2011)

[24] S. F. Paul *et al.*, *Phys. Fluids B* **4**, 2922 (1992)

[25] R. J. Fonck, P. A. Duperrex, and S. F. Paul, *Rev. Sci. Instrum.* **61**, 3487 (1990)

[26] S. F. Paul, and R. J. Fonck: *Rev. Sci. Instrum.* **61**, 3496(1990)

[27] H. Evensen *et al.*, *Rev. Sci. Instrum.* **63**, 4928 (1992)

[28] R. D. Durst *et al.*, *Rev. Sci. Instrum.* **66**, 842(1995)

[29] G. Mckee *et al.*, *Rev. Sci. Instrum.* **70**, 913 (1999)

[30] G. Mckee *et al.*, *Phys. Rev. Lett.* **84**, 1922(2000)

[31] M. Jakubowski *et al.*, *Rev. Sci. Instrum.* **70**, 874 (1999)

[32] G. R. Mackee, R. J. Fonck, M.Jakubowski, K. H. Burrell, K. Hallatschek, R. A. Moyer, D. L. Rudakov, W. Nevins, G. D. Porter, P. Schoch, and X. Xu, *Phys. Plasmas*, Vol.10 No.5, 1712(2003)

[33] T. Oishi, Master thesis, Department of Quantum Engineering and Systems Science, Graduate School of Engineering, The University of Tokyo (2003）

[34] T. Oishi *et al.*, *J. Plasma Fusion Res.* **6**, 449(2004)

[35] T. Oishi *et al.*, *Rev. Sci. Instrum.* **75**, 4118(2004)

[36] S. Kado, *J. Plasma Fusion Res.* **83**, 176(2007)

[37] T. Oishi, S. Kado, K. Ida, M. Yoshinuma, H. Nakano, and K. Yamazaki, *Rev. Sci. Instrum.* **81**, 10D719 (2010)

[38] S. Kobayashi, S. Kado *et al.*, *Rev. Sci. Instrum.* **81**, 10D726(2010)

[39] I. H. Hutchinson, *Plasma Phys. Control. Fusion* **44**, 71(2002)

[40] S. Kado *et al.*, *Rev. Sci. Instrum.* **81**, 10D720 (2010)

[41] D. R. Smith *et al.*, *Rev. Sci. Instrum.* **81**, 10D717 (2010).

[42] M. Yoshinuma, K. Ida, M. Yokoyama, M. Osakabe, and K. Nagaoka, *Fusion Sci. Technol. 58*, 375 (2010)

[43] C. D. Boley, R. K. Janev, and D. E. Post, *Phys. Rev. Lett.* **52**, No. 7, 534(1984)

[44] D. K. Gupta, R. J. Fonck, G. R. McKee, D. J. Schlossberg, and M. W. Shafer, *Rev. Sci. Instrum.* **75**, 3493 (2004)

[45] M. Ono *et al.*, *J. Plasma Fusion Res.* **11**, 1402115 (2016)

[46] M. Ono *et al.*, *Rev. Sci. Instrum.* **87**, 11E559 (2016)

[47] Burg J P, *et al.* 1975 ”Maximum entropy sepctral analysis” Ph.D. dissertation. Dep. Geophys., Stanford Univ., Stanford, CA, May, (1975)

[48] G. R. McKee, R. J. Fonck, D. K. Gupta, D. J. Schlossberg, M. W. Shafer, R. L. Boivin, and W. Solomon *Plasma Fusion Res.* **2**, S1025 (2007)

[49] R. D. Durst, R. J. Fonck, G. Cosby, H. Evensen, *Rev. Sci. Instrum.* **63**, 4907 (1992)

[50] T. A. Gianakon, R. J. Fonck, J. D. Callen, R. D. Durst, J. S. Kim, and S. F. Paul *Rev. Sci. Instrum.* **63**, 4931 (1992)

[51] G. R. McKee, C. Fenzi, R. J. Fonck, and M. Jakubowski, *Rev. Sci. Instrum.* **74**, 2014 (2003)

[52] G. McKee, R. Ashley, R. Durst, R. Fonck, M. Jakubowski, K. Tritz, K. Burrell, C. Greenfield, and J. Robinson, *Rev. Sci. Instrum.* **70**, 913 (1999)

[53] F. J. Fonck, R. Ashley, R. Durst, S. F. Paul, and G. Renda, *Rev. Sci. Instrum.* **63**, 4292 (1992)

[54] R. Hong and H.k. Chiu, ”Effects of Operating Prameters on the Beam Species of DIII-D Neutral Beam Ion Sources” Proc. of 19th IEEE/NPSS Symp. on Fusion Engineering, Atlantic City, Nes Jersey (2002)

[55] R. V. Bravenec, and A. J. Wootton, *Rev. Sci. Instrum.* **66**, 802 (1995)

[56] M. W. Shafer, R. J. Fonck, G. R. McKee, and D. J. Schlossberg, *Rev. Sci. Instrum.* **77**, 10F110 (2006)

[57] Y. Tsuji, H. Tanaka, T. Ohno, *J. Plasma Fusion Res.* 85, No.9, 620 (2009) (Japanese)

[58] M. Hino, ”*Spectral Analysis*” , Asakura Publishing (1977) (Japanese)

[59] T. Kobayashi, Doctoral thesis, Interdisciplinary Graduate School of Engineering Sciences, Kyushu University (2013）

[60] G. R. McKee, *et al.*, *Plasma Fusion Res.* **2**, s1025 (2007).

[61] T. Yamada, *et al.*, *Nature Phys.* **4**, 721 (2008).

[62] K. H. Burrell, *Phys. Plasmas* **4**, 1499 (1997).

[63] C. Watts, *Fusion Sci. Tech.* **52**, 176 (2007).

[64] M. E. Austin and J. Lohr,*Rev. Sci. Instrum.* **74**, 1457 (2003).

[65] M. Bornatici *et al.*,*Plasma Phys.* **23**, 1127 (1981).

Appendix A

Optical thickness

The radiation emitted from an electron accelerated by Lorentz force is called electron cyclotron emission (ECE). By mesuring spectrum of the radiation, information on electron temperature and runnaway electron can be obtained. The radiation intensity $I(\omega)$ depends on the strength of absorption, and is expressed in MKS units as

$$I(\omega) = I_{BB}(\omega)\frac{1-e^{-\tau}}{1-\rho e^{-\tau}} = \frac{I_{BB}(\omega)}{k_B T_e} k_B T_{rad} \tag{A.1}$$

where $I_{BB}(\omega)$ is the blackbody radiation intensity, ρ is the effective wall reflectivity with value between 0 and 1, k_B is Boltzmann's constant, T_{rad} is the electron temperature, T_{rad} is the radiation temperature as determined by a radio meter calibrated in terms of black body temperature, and τ is a value called optical thickness. The optical thick ness is defined as

$$\tau = \int_0^l \alpha(\omega)\mathrm{d}s, \tag{A.2}$$

where l is the path of the ray in the plasma, and $\alpha(\omega)$ is the absorption coefficient defined as the fractional rate of absorption of radiation per unit path length. If $\tau \gg 1$, the plasma is called optically thick, and the radiation intensity is proportional to electron temperature. On the other

hand, in the case that $\tau \ll 1$ it is said to be optically thin, and self-absorption is negligible.

The blackbody radiation intensity for a polarization mode is given as

$$I_{BB}(\omega) = \frac{\hbar\omega^3}{8\pi^3 c^2} \frac{1}{e^{\hbar\omega/k_B T_e} - 1}. \tag{A.3}$$

Here, $\hbar = h/2\pi$ with the Planck constant h. In high temperature plasmas such that $\hbar\omega/k_B T_e \ll 1$, one has

$$I_{BB}(\omega) = \frac{\omega^2 k_B T_e}{8\pi^3 c^2}, \tag{A.4}$$

that is, the equation for the Rayleigh-Jeans blackbody Law. In optically thick plasmas ($\tau \gg 1$), therefore, the radiation intensity of the detected frequency ω is equivalent to the blackbody radiation intensity and proportional to electron temperature. In a metal containment vessel with a high value of ρ, $\tau_{crit} \sim 2$ is considered a sufficient lower limit for optically thick plasmas. For temperature fluctuation mesurement the appropriate τ_{crit} should be ~ 3, instead of the value of 2 [63].

From Ref. [65], optical thickness of X-mode n-th harmonics ($n \geq 2$) in a tokamak plasma for propagation perpendicular ($\theta = \pi/2$) with respect to the external magnetic field on the equitorial plane is given as

$$\tau_n^{(X)} = \tau_n^{(X)}\left(\theta = \frac{\pi}{2}\right) = \frac{\pi^2 n^{2(n-1)}}{2^{n-1}(n-1)!} \left(\frac{\omega_{pe}}{\omega_{ce}}\right)^2 \left(\frac{v_t}{c}\right)^{2(n-1)} \mu_n^{(X)}\left(\theta = \frac{\pi}{2}\right) \frac{R_0}{\lambda_0} \tag{A.5}$$

with

$$\mu_n^{(X)}\left(\theta = \frac{\pi}{2}\right) = \left(N_\perp^{(X)}\right)^{2n-3} \left[1 + \frac{\left(\omega_p/\omega_c\right)^2}{n\left[n^2 - 1 - \left(\omega_p/\omega_c\right)^2\right]}\right]^2, \tag{A.6}$$

$$\left(N_\perp^{(X)}\right)^2 = 1 - \left(\frac{\omega_{pe}}{n\omega_{ce}}\right)^2 \frac{\left[n^2 - \left(\omega_p/\omega_c\right)^2\right]}{\left[n^2 - \left(\omega_p/\omega_c\right)^2\right] - 1},$$

where $\omega_{pe} = \sqrt{n_e e^2/\varepsilon_0 m_e}$ is the plasma frequency, $\omega_{ce} = eB/m_e$ is the electron cyclotron frequency, $v_t = (k_B T_e/m_e)^{1/2}$ is the thermal velocity of the electrons, c is the speed of light, $\lambda_0 = 2\pi c/\omega_c$ is the wavelength of the radiation, and R_0 is the major radius of the torus. For densities such that $\omega_{pe}^2 < n(n-1)\omega_{ce}^2$, Eq. A.6 becomes, to lowest significant order in $(\omega_{pe}/\omega_{ce})^2$,

$$\mu_n^{(X)}\left(\theta = \frac{\pi}{2}\right) \simeq 1 - c_n\left(\frac{\omega_p}{\omega_c}\right)^2$$

with $c_n \equiv (n - 3/2 - 2/n)/(n^2 - 1)$. For the second harmonic, $c_2 = -1/6$, Eq.A.5 reduces to

$$\tau_2^{(X)}\left(\theta = \frac{\pi}{2}\right) = \frac{\pi e}{\varepsilon_0 m_e c^3}\left(1 + \frac{1}{6}\frac{n_e m_e}{\varepsilon_0 B^2}\right)\frac{n_e k_B T_e R}{B}. \tag{A.7}$$

Using values of $|B_T| = 1.58$T, $n_e = 2.02 \times 10^{19}$n^{-3}, and $k_B T_e = 1.20$keV $= 1.92 \times 10^{-16}$[J at the measurement location of the ECE channel, $R = 2.23$m (normalized minor radius $\rho \sim 0.88$ at $t = 4125$ms), optical thickness is estimated as $\tau \sim 14.3\tau_{crit}$, and the plasma is optically thick enough for temperature fluctuation measurement.